# Surface Chemistry of

# Flat-Model Ziegler-Natta Catalysts

PROEFSCHRIFT

ter verkrijging van de graad van doctor aan de
Technische Universiteit Eindhoven,
op gezag van de rector magnificus prof.dr.ir. C.J. van Duijn,
voor een commissie aangewezen
door het College voor Promoties,
in het openbaar te verdedigen
op dinsdag 10 december 2013 om 16:00 uur

door

Ajin Verghese Cheruvathur

geboren te Vadakkekad, India

Dit proefschrift is goedgekeurd door de promotor en de samenstelling van de promotiecommissie is als volgt:

| | |
|---|---|
| Voorzitter : | prof.dr.ir. J.C. Schouten |
| Promotor : | prof.dr. J.W. Niemantsverdriet |
| Copromotor : | dr. P.C. Thüne |
| Leden : | prof.dr. V. Busico |
| | (Università di Napoli "Federico II") |
| | prof.dr. P. Budzelaar |
| | (University of Manitoba) |
| | prof.dr.ir. R.A. Janssen |
| Adviseur : | dr. G. Kishan |
| | (SABIC Europe B. V.) |

*"A theory is something nobody believes, except the person who made it;*
*an experiment is something everybody believes, except the person who made it."*

*-    Albert Einstein*

Ajin Verghese Cheruvathur

## *Surface Chemistry of Flat-Model Ziegler-Natta Catalysts*

## Table of contents

### Chapters

### Postface

# 1

# Introduction and scope of the thesis

## **Abstract**

*Ziegler-Natta catalysis is one of the most significant industrial processes in the mass production of polyolefins with a high degree of stereoselectivity. Over the years, these catalysts have developed from simple $TiCl_3$ crystals into $MgCl_2/TiCl_4$/donor systems, showing very high activity and selectivity. However, the molecular-level scientific elucidation of structures and reaction mechanisms of the new catalyst system did not follow this technological progress. This chapter provides an introduction to catalysis and a literature overview of the present knowledge about $MgCl_2$-supported Ziegler-Natta catalyst molecular level structure. Finally, we describe the scope of the thesis and the flat-model approach.*

## 1.1 Catalysis

### 1.1.1 Catalysis: past and present

For centuries, catalysts have been used to make beverages. For instance, a biocatalyst converts sugar to alcohol. In that time, chemistry was practised more like alchemy in which the chemist tried to convert scrap metal into expensive noble metals like gold. One sees that the Lead Chamber process for the production of sulphuric acid is among the earliest of catalytic processes and reaches back to 1750:[1] however, catalytic reactions were poorly or not at all understood. The term 'catalysis' was first defined by the Swedish chemist Berzelius in 1835.[2,3] In fact, the word catalysis originates from the Greek verb 'kata-luein' which means 'to dissolve' or 'loosen'. Basically, this meaning is one of the most trivial properties of a catalyst possesses: the ability to loosen or break chemical bonds. Today, catalysis is one of the principal drivers of the modern economy. According to the Freedonia Group, world catalyst demand is $14.7 billion in 2012, which is forecast to $19.5 billion in 2016.[4] Catalysts impact a sizable fraction of any nation's gross domestic product. In olefin polymerization, some catalysts produce million pounds of polymer per pound of metal (in the catalyst) per hour! It has been estimated that about 90% of the chemicals are derived in some fashion from catalytic processes.[5] Furthermore, catalysis is one of the 12 green chemistry principles.[6]

### 1.1.2 Principles of catalysis

Nowadays, a more popular description of a catalyst is: a substance that accelerates the rate of a chemical reaction by offering different pathways lower in energy than the respective uncatalyzed (gas-phase) reaction without being consumed itself. The so-called 'catalytic cycle' is depicted in Figure 1.1.[7] Every catalytic reaction is a sequence of elementary steps, in which reactant molecules bind to the catalyst, where they react, after which the product detaches from the catalyst, liberating the latter for the next cycle.

In general, catalysis can be subdivided into three major classes: homogeneous, heterogeneous and biocatalysis. In homogeneous catalysis, the catalyst is usually an organometallic complex that is dissolved in solvent along with reactants. Biocatalysis is an area of homogeneous catalysis where natural

3

products (enzymes) are used in chemical reactions. In heterogeneous catalysis, the catalyst is a solid, which catalyzes the reaction of reactants present in either gas or liquid phase. Because these catalytic reactions occur solely on the surface, the majority of catalysts are nanometer-sized particles, supported on an inert porous material with high surface area, such as alumina, silica and carbon. Although heterogeneous catalysts are mostly less active than homogenous catalysts, separation of the catalyst from the reaction system is relatively easy; thus, the catalyst can be recycled more often, which lowers their costs significantly. The easy separation of the catalyst from the reaction mixture also provides the possibility of continuous catalytic process. In this thesis; all work presented, is regarded as heterogeneous catalysis.
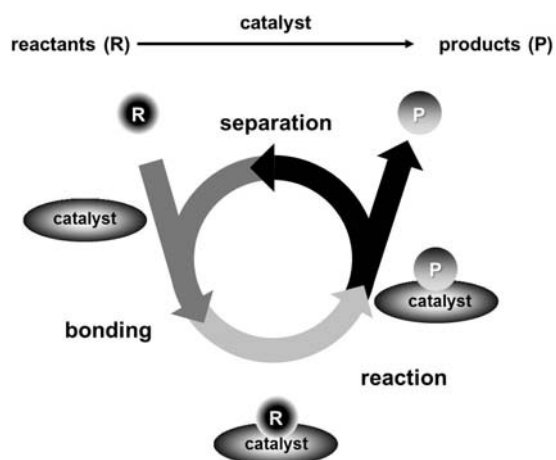


**Figure 1.1.** *A schematic representation of the catalytic cycle.*[7]

To get a better understanding of the catalyst's behaviour in terms of accelerating the reaction ($A_2+B_2 \rightarrow 2AB$), a potential energy diagram is presented in Figure 1.2. Within this respect, the steps in the catalytic cycle will be adsorption of reactant, reaction on the catalyst surface, desorption of product from the catalyst surface. The first step is the adsorption of the reactants $A_2$ and $B_2$. This is always an exothermic process, leading to a lower energy in the potential energy diagram. Next, the catalyst breaks the A-A and B-B bonds of the molecule, and when A and B atoms are in proximity of each other due to their respective diffusion on the surface, the catalyst creates a new bond between A and B to produce AB. The activation barrier required for this catalyzed to occur is noticeably lower than the

non-catalyzed reaction; therefore, leading to a much higher reaction rate at a given temperature and enabling much milder conditions (lower temperature and pressure). Finally AB is desorbed from the surface, and the reaction starts all again. Both reaction pathways end at the same energy level, thus, the overall potential energy is not changed when the reaction is catalyzed. Hence, a catalyst solely affects the kinetics of the reaction, but not its thermodynamics.
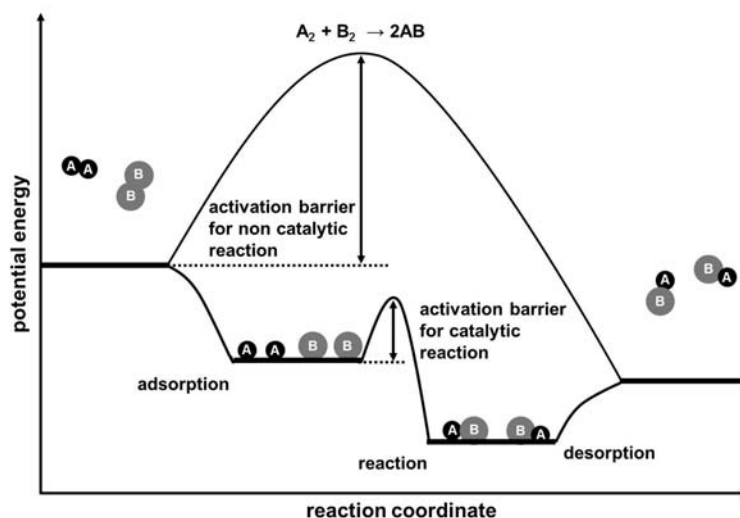


**Figure 1.2.** *Potential energy diagram of a reaction ($A_2+B_2{\rightarrow}2AB$) in catalytic and non-catalytic pathways. Note that the uncatalyzed reaction has to overcome a substantial energy barrier, whereas the barriers in the catalytic route are much lower.*[7]

## 1.2 Polyolefin catalysis

### 1.2.1 Polyolefins

Polyolefins, the generic name for the synthetic polymers based on ethylene, propylene, other non-functionalized α-olefins and reactive internal olefins are the most common commodity plastics. Scheme 1.1 represents the polymerization of α-olefin monomers to poly-α-olefin. In 2006, they constitute over 60% of the entire production of plastics.[8] The large volume production and broad utility of polyolefins, synthesized from a very simple set of inexpensive monomer units are related to their wide range of properties allowing them to be used in a wide variety

of applications, ranging from simple plastic bags to high strength fibres.[9] The growth of the span of polymer properties has been fueled by the continuous development of new catalyst systems as well as suitable process technologies, both from academic and industrial researchers.
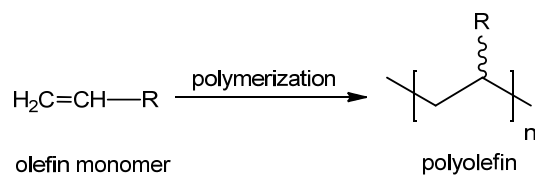


**Scheme1.1.** *General scheme of α-olefin polymerization. Right hand side of the equation shows the repeating unit of polyolefin; where n can vary from thousands to millions.*

## 1.2.2 Polyethylene and polypropylene

Among different polyolefins, polyethylene (PE) and polypropylene (PP) have established a prominent position, attributable to their cost and performance balance, and their economical and environmentally friendly production. In the total production of ~205 million tonnes of synthetic plastics in 2012, polyethylene is the largest volume polymer produced worldwide with a total production of over ~76 million tonnes per year.[10] The three major classes of polyethylene are described by high density polyethylene (HDPE), low density polyethylene (LDPE), and linear low density polyethylene (LLDPE).[11] Next to polyethylene, polypropylene constitutes the second largest volume polyolefin with a global market of ~53 million tonnes in 2012.[10] The polymerization of propylene is similar to that of ethylene, however, propylene being a prochiral monomer the resulting polymer chain may show different stereochemical orientations (tacticity). There are three predominant microstructures known for polypropylene depending on the orientation of each methyl group relative to the neighbouring methyl group in the polymer chain, namely atactic polypropylene, isotactic polypropylene and sydiotactic polypropylene (Figure 1.3).

When the methyl group in the polymer chain has no preference towards any particular orientation with respect to the carbon-carbon backbone (polypropylene formed via random monomer insertions), polypropylene thus formed is called

atactic polypropylene. Due to the lack of crystallinity, atactic polypropylene is an amorphous rubbery material with very little strength and is generally used in adhesive and roofing tar. The polypropylene in which all the side chain methyl groups have the same regular orientation along the polymer chain is referred as isotactic polypropylene. Due to its highly ordered structure isotactic polypropylene has a high crystallinity, resulting in good mechanical properties such as stiffness and tensile strength. In syndiotactic polypropylene, the methyl groups alternate regularly from side to side in the polymer chain. Syndiotactic polypropylene chains are less stiff than isotactic polypropylene chains, but materials based on it have a better impact strength and clarity.
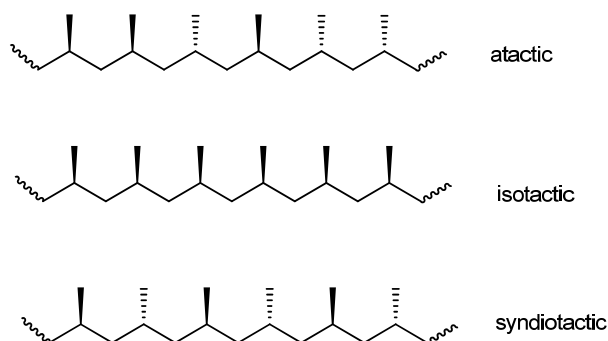


**Figure 1.3**. *Schematic representation of polypropylenes with different tacticity.[12]*

## 1.2.3 Ethylene and propylene polymerization catalysis

The first commercialization of polyethylene production was established in 1939 by Imperial Chemical Industry (ICI), using a high pressure-high temperature free radical process for the production of LDPE.[13] In 1951, Phillips Petroleum Company developed a low temperature, low pressure process for the production of polyethylene using a chromium trioxide-based catalyst supported on silica.[14] This type of catalyst still constitutes around 30% of today's production of HDPE and LLDPE. The biggest breakthrough came in 1953, when Karl Ziegler at the Max Planck Institute in Mülheim discovered combinations of transition metal salts and aluminium alkyls which were able to polymerize ethylene at low temperatures and pressures, giving HDPE.[15-16] Giulio Natta at Milan Polytechnic noticed the significance of the Ziegler catalyst system in the polymerization of propylene,

when he succeeded in isolating crystalline polypropylene (isotactic polypropylene).[17-18] The scientific breakthroughs, which allowed Ziegler and Natta to share the Nobel Prize in 1963, were quickly translated into industrial realities by Hoechst in 1955 and Montecatini in 1957, with the manufacture and commercialization of high-density polyethylene and isotactic polypropylene, respectively.[19]

## 1.2.4 Ziegler-Natta catalysts

A Ziegler-Natta catalyst may be defined as a combination of (i) a transition metal compound of an element from groups IV to VIII and (ii) an organometallic compound with the metal from group I to III of the periodic table. This combination provides a transition metal compound bearing a metal-carbon bond; which is able to promote a repeated insertion of olefin units and thus generate a macromolecular polyolefin chain. Therefore, the transition metal compound is denoted as the catalyst (the polymerization occurs at the transition metal center) and the organometallic compound is named as the cocatalyst or activator (creates the transition metal-carbon bond which is essential for monomer insertion). Transition metal compounds containing Ti, V and Cr are used as catalysts (largely Ti). Aluminum alkyls such as $AlEt_3$, $Al\text{-}i\text{-}Bu_3$ and $AlEt_2Cl$ are preferred as cocatalyst.

Ziegler-Natta catalysts are generally described in terms of generations, corresponding to the chronological order of their development.[20] The first two generations are based on $TiCl_3.0.33AlCl_3$ solid mixture (self-supported catalysts). The $TiCl_3$ catalysts (first generation) used in the early industrial process were typically prepared by the reduction of $TiCl_4$ with an aluminium alkyl or aluminium metal, generating a solid of composition $\beta\text{-}TiCl_3.0.33AlCl_3$. The catalyst activity was low (compared to today's standards), means the removal of catalyst residues (de-ashing) of catalyst residues from the polymer was necessary. In the case of propylene polymerization, due to the limited catalyst stereoselectivity (selectivity towards isotactic polypropylene) it was also necessary to remove 'atactic' polymer from the product. During the early 1970s, an improved $TiCl_3$ catalyst was developed by Solvay (second generation).[22] A spheroidal catalyst was obtained via reduction of $TiCl_4$ with $AlEt_2Cl$ and a subsequent treatment with di-n-butyl or di-

iso-amyl ethers, followed by treatment with $TiCl_4$. Because of the increased isospecificity of polymer (stereoselectivity of the catalyst), the removal of atactic fraction was not necessary. However, the productivity was not enough to avoid the de-ashing steps.

A drastic innovation was achieved with the development of $MgCl_2$ supported catalysts prepared by co-milling $TiCl_3$ and $TiCl_4$ with $MgCl_2$.[23] Compared to the predecessors, $MgCl_2/TiCl_4/AlR_3$ catalyst exhibited higher activity towards ethylene polymerization. In the case of propylene polymerization, the high activity was associated with a low selectivity.[24] In early 1970s, Montedison scientists noticed that the stereoselectivity of the $MgCl_2$ based catalyst can be increased by adding Lewis bases (generally known as electron donors in Ziegler-Natta chemistry); one with the $MgCl_2/TiCl_4$ solid component and another one together with $AlR_3$.[25] The former category of Lewis bases was called internal donor (inside the solid component) and the latter category of Lewis bases was called external donor (added externally with cocatalyst). The third, fourth and fifth generations of Ziegler-Natta catalysts differ mainly in the nature of internal-external donor couple. The influence of electron donors and the selection of internal-external donor pair will be explained in the following section. In 2001, 51% of global polyethylene production and 95 % of global polypropylene production were catalyzed by $MgCl_2$ supported Ziegler-Natta catalysts.[26]

## 1.2.5 Mechanism and Stereochemistry of polymerization

The first well-accepted mechanism for olefin polymerization was proposed by Cossee and Arlman in the mid-1960s.[27-29] This monometallic mechanism is applicable to different catalyst systems. In the particular case of Ziegler-Natta catalysis, the monometallic center is a surface Ti atom. The isospecific active site is an octahedrally coordinated titanium ion having a vacant position. The role of the cocatalyst is to form a Ti-C bond (via alkylation) and possible reduction of the transition metal atom. Thus, the active center is a titanium atom having a vacant coordination site and a Ti-C bond. Polymerization occurs via two steps. First step is the formation of an olefin π-adduct by the coordination of olefin to the vacant site of the active catalyst. The subsequent step is the migratory insertion of the olefin monomer into the metal-carbon bond via four center transition state. The

vacant coordination site, which regenerates at the end of the second step, enables further chain propagation. The polymer chain may or may not revert (back-skip) to the original position, depending on the ligand structure of Ti center catalyst and presence of steric hindrance on the surface of a heterogeneous Ziegler-Natta catalyst. Figure 1.4 represents the propagation step of olefin polymerization over Ziegler-Natta catalysts.
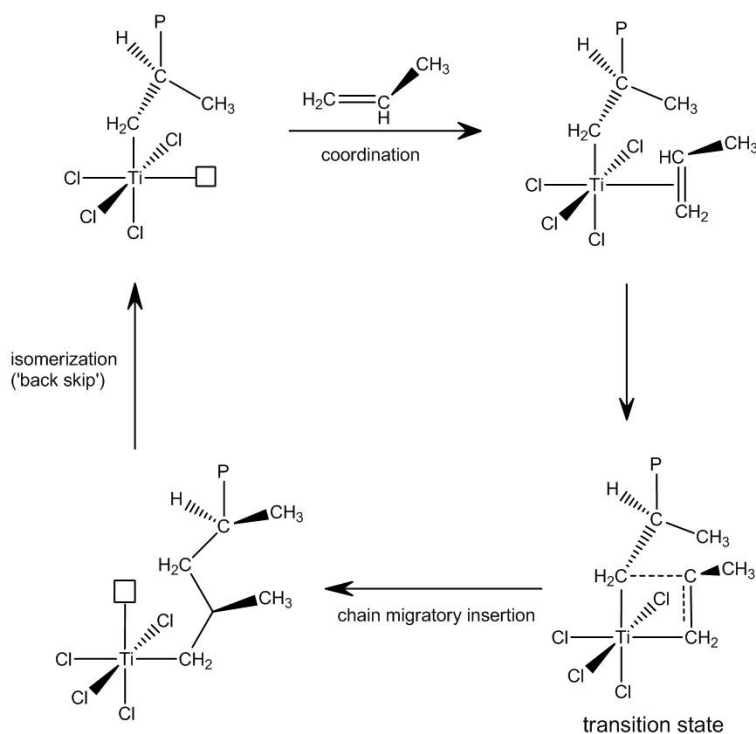


**Figure 1.4**. *Cossee's mechanism of Ziegler-Natta polymerization of propylene.*[19]

In the case of propylene and higher α-olefins (monomers with $C_s$ symmetry) polymerization using titanium chloride catalysts, chain propagation occurs via 1,2- insertion (primary insertion) of the monomer. The selectivity towards 1,2- insertion or 2,1- insertion (secondary insertion) is known as the regioselectivity of the catalyst. Compared to 2,1-insertion, the 1,2- insertion is generally favored; which results in the incorporation of less bulky -$CH_2$- near the metal (Figure 1.5a). Occasionally, 2,1- insertion can also occur, which results in the formation of a

dormant site and a reduction of the catalytic activity. For isospecific propagation, there must be only one coordination vacancy on a metal center and the active site must be chiral.[30] Corradini and coworkers have shown that the asymmetric environment of the active site compels the growing chain to adopt a particular orientation and reduce steric interactions with ligands (chlorine) present on the catalyst surface.[31] This leads to one particular prochiral face of the inserting monomer being preferred (as illustrated in Figure 1.5b) leads to isotactic polymer. Polymer chain termination occurs through hydrogen addition to growing polymer chain (Ti-$CH_2$-$CH_2$-Polymer + $H_2 \rightarrow$ Ti-H +$CH_3$-$CH_2$-Polymer). Hydrogen is used to control the molecular weight of the polymer. In the absence of hydrogen, β-hydride transfer with monomer occurs; releasing a polymer chain with vinylidene end groups (Ti-$CH_2$-$CH_2$-Polymer + $CH_2$=$CH_2 \rightarrow$ Ti-$CH_2$-$CH_3$ +$CH_2$=$CH$-Polymer). Another termination process in the absence of added hydrogen is the β-H elimination (Ti-$CH_2$-$CH_2$-Polymer $\rightarrow$ Ti-H +$CH_2$=$CH$-Polymer). To a lesser extent, alkyl exchange with cocatalyst and growing polymer chain also occurs (Ti-$CH_2$-$CH_2$-Polymer + $AlR_3 \rightarrow$ Ti-R +$AlR_2$-$CH_2$-$CH_2$-Polymer).
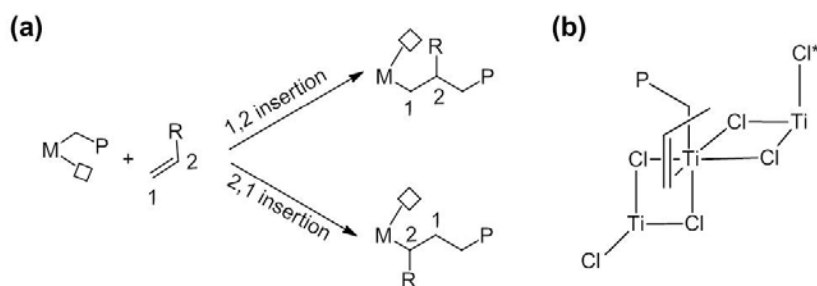


**Figure 1.5.** *(a) Scheme showing 1,2 and 2,1 insertion of α-olefin monomer M-P = polymer chain. (b)Model for stereospecific polymerization of propylene.*

## 1.2.6 Choice of MgCl₂ as a support

The use of $MgCl_2$ as a support was based on the assumption that the 'dilution' of Ti atoms on a high surface area carrier could be largely improve catalyst efficiency because a large number of surface Ti atoms are available for polymerization. The crystalline structure of $MgCl_2$ (α and β forms) is isomorphous with $TiCl_3$(γ and δ forms).[19] The ionic radii of $Mg^{2+}$(0.65 Å) and $Ti^{4+}$ (0.68 Å) ions

are very close. More specifically both $Mg^{2+}$ and $Ti^{4+}$ ions display the same octahedral coordination geometry and have comparable metal-chlorine bond lengths (Mg-Cl = 2.57 Å, Ti-Cl = 2.51 Å). This allows epitactic adsorption of $TiCl_4$ on the $MgCl_2$ surface, the formation of catalytic sites, which are analogous to those present on the surface of pure $TiCl_3$.

A structural layer of anhydrous $MgCl_2$ is depicted in Figure 1.6.[32] The atoms are organized in two-dimensional hexagonal arrays, with repetition periods a = b = 3.64 Å, γ = 120° for $MgCl_2$. This creates 'structural' triple layers in which the magnesium atoms are sandwiched between two layers of chlorine along the direction normal to the layers. Mg atoms are octahedrally coordinated and strongly bonded with Cl. The stacking of structural layers along the direction normal to the layers, at a distance of 5.90 Å. A regular cubic or a hexagonal packing mode of the bulkier Cl atoms gives rise to the α (c = 17.7 Å)[33] and β (c = 5.90 Å)[34] modifications respectively. The two forms differ only by the stacking of the hexagonal layers; ABC BCA CAB…and ABC ABC ABC…for the α-$MgCl_2$ and β-$MgCl_2$ respectively. The internal structures of hexagonal layers are almost equivalent, since van der Waals interaction between the layers is very weak.[34,35]
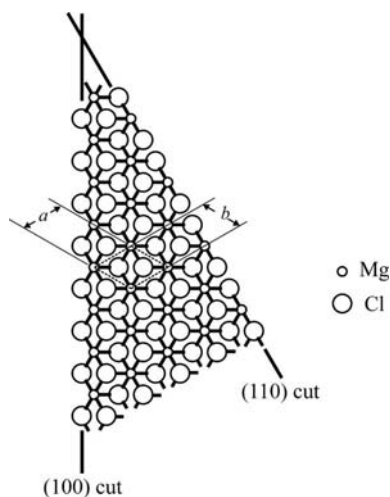


**Figure 1.6.** *Model of the Cl-Mg-Cl structural layer in $MgCl_2$ layer compounds showing the (100) and (110) cuts. The hexagonal unit-cell parameters for a = b = 3.64 Å are also indicated.*[32,38]

In order to exploit the maximum potential of $MgCl_2$ support by maximizing the amount and dispersion of Ti sites, a crystal modification with very high surface area is required. This usually demands an 'activation' process, which leads to the formation of structural disordered small crystallites ($\leq$ 3nm thick) of $MgCl_2$.[36] The activation can be performed by mechanical treatment (ball-milling) or a chemical reaction; in both cases $TiCl_4$ and/or Lewis base can be directly incorporated. In these disordered active forms ($\delta$ modifications) of $MgCl_2$, the successive Cl-Mg-Cl sandwich layers are stacked along the 'c' axis according to a hexagonal sequence or with a rotational disorder of 60°. The combination of small crystallite size and large rotational disorder leads to a higher activity.[32,37]

Giannini has indicated that, Mg atoms on the preferential lateral cleavage surfaces of $MgCl_2$ crystals are coordinated with four or five Cl atoms instead of six Cl atoms in the bulk.[38] The lateral cuts correspond to (110) and (100) faces of $MgCl_2$ as illustrated in Figure 1.6. Coordination numbers of Mg on (110) and (100) are four and five respectively. However, very recently, the crystal structure of $MgCl_2$ supports has been re-evaluated by Busico and coworkers who concluded that the surface with five-coordinate Mg cations should be indexed as (104) rather than (100).[39] In this thesis (to the rest of **Chapter 1** and following **Chapters**), we will adopt the indices (110) and (104) to represent the four and five-coordinate surfaces, respectively.

Corradini and coworkers proposed a plausible model for the active sites on the $MgCl_2$ crystal surfaces.[40,41] Structures of $TiCl_4$ surface species and active sites have been discussed based on the $MgCl_2$ (110) and (104) surfaces. $TiCl_4$ epitaxially adsorbs on these $MgCl_2$ surfaces due to similar ionic radii between $Ti^{4+}$ and $Mg^{2+}$, bearing the $TiCl_4$ monomeric species on the (110) surface and $Ti_2Cl_8$ dimeric species on the (104) surface.[40] The reaction of $MgCl_2$ support with $TiCl_4$ leads to the adsorption of $TiCl_4$ on $MgCl_2$ lateral cuts. Later $Ti^{4+}$ is reduced to $Ti^{3+}$ by the action of cocatalyst ($AlR_3$), and a Ti-C bond is introduced which is required for the insertion of a monomer molecule. Active sites for propylene polymerization are regarded as monoalkylated trivalent Ti species, resulting from the extraction and alkyl substitution of terminal Cl atoms with alkyl aluminium activator.[42,43] Analogous to the first and second generation $TiCl_3$ catalysts, the monomeric Ti species on the (110) surface and the dimeric Ti species on the (104)

13

surface were respectively assigned as aspecific and isospecific active sites.[40] Figure 1.7 indicates a model for the monolayer of $MgCl_2$ representing the most probable (104) and (110) cleavage surfaces and proposed coordination modes of $TiCl_4$ species on $MgCl_2$ lateral cuts; dimeric and monomeric species on a (104) and monomeric species on a (110) cut.
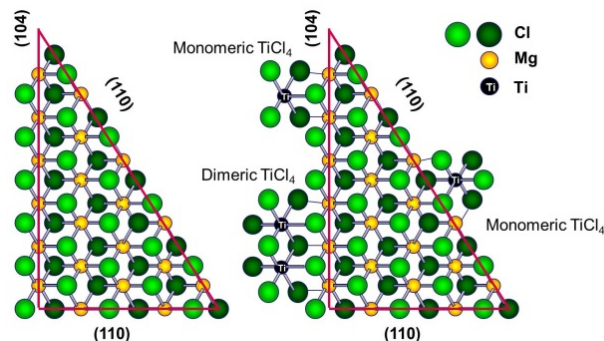


**Figure 1.7.** *Model for a monolayer of a $MgCl_2$ crystal showing the most probable (104) and (110) cleavage cuts and Ti species on these cuts.*[38,44]

Transmission electron microscopy/electron diffraction studies can provide direct assignments of surface edges in a crystal. However, gaining structural insight into Ziegler-Natta catalysts by means of TEM turned out to be extremely difficult. The major difficulty is the platelet-like morphology of $MgCl_2$ crystals tend to expose the coordinatively saturated basal planes (001) of no interest for catalysis.[39] In the past, transmission electron microscopy (TEM) was used for microscopic observation of polyolefins produced on Ziegler-Natta catalysts.[45,46] Direct TEM imaging of α-$TiCl_3$ was also reported in literature.[47,48] A microscopic analysis of the initial stage of the polyolefin formation on a $TiCl_4$/$MgCl_2$ catalyst was reported by Barbe and coworkers who used a gold sputtering technique for the TEM samples.[49] Using high resolution TEM, the (110) lateral cut of $MgCl_2$ in Ziegler-Natta catalyst (without electron donor) was identified.[50] Another high resolution TEM study on industrial catalysts (with ester or diester as an electron donor) revealed that changes in catalyst preparation methods can affect the atomic structure of $MgCl_2$ crystals.[51]*In-situ* real-time environmental TEM studies on donor-free $TiCl_4$/$MgCl_2$ catalyst identified different lateral terminations of $MgCl_2$.[52]

14

### 1.2.7 The role of electron donors

Even though the activity of the $MgCl_2/TiCl_4/AlR_3$ catalyst is higher than that of a $TiCl_3$ catalyst, the selectivity is almost half. Giannini and coworkers found that the incorporation of electron donors into the $MgCl_2$ supported catalyst system regained the selectivity.[25] Based on Corradini's model,[40,41] the role of the electron donor is twofold; (i) provide stability to small crystallites of $MgCl_2$ by binding to (104) and (110) lateral surfaces of $MgCl_2$, (ii) reintroduce the stereoselectivity of catalyst by selective poisoning of aspecific (110) surface sites. The latter is achieved by favourable (or stronger) coordination of electron donor on the more Lewis acidic $MgCl_2$ (110) site compared to less Lewis acidic $MgCl_2$ (104) site. This increases the proportion of isospecific dinuclear $Ti_2Cl_6$ species among the active species for polymerization and hence the stereoselectivity of the catalyst. In other words, an electron donor controls the amount and distribution of $TiCl_4$ on the support surface. Schematic drawings of the hypothetical distribution of Lewis base (LB) on the (104) and (110) cuts before and after titanation is shown in Figure 1.8.
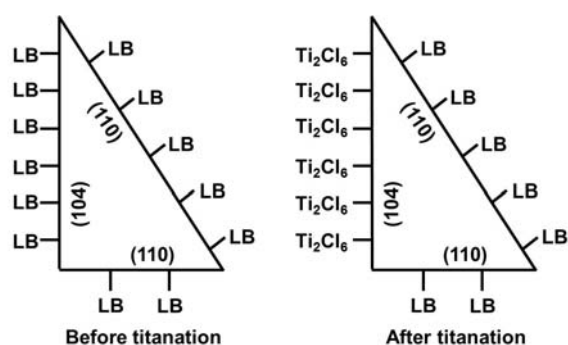


**Figure 1.8.** *Schematic drawings of hypothetical distribution of Lewis base (LB) on the (104) and (110) cuts; before and after $TiCl_4$ treatment.*[42]

The proposal indirectly assumes that isospecific active sites are the same dimeric Ti species irrespective of the donor structures and the degree of the stereospecific improvement depends on the selectivity of the donor adsorption on the (110) surface. As the research progressed, it became clear that polymer microstructures reflecting active site structures are sensitive to donor structures.[53,54] A powerful technique to study the effects of electron donors on site selectivity in

Ziegler-Natta catalysts is the determination of the stereoregularity of the first insertion step in propylene polymerization. The first step stereoregularity is particularly sensitive to the steric environment of the active center, due to the fact that the stereospecificity of the first monomer insertion has been always lower than that of the following propagation steps.[44] Investigation of the effect of alkoxysilane donors on the first step stereoregularity resulting from propylene insertion into a Ti-Et bond formed via chain transfer with $^{13}$C enriched AlEt$_3$ using a MgCl$_2$/TiCl$_4$/diisobutyl phthalate catalyst, showed that the mole fraction of erythro (isotactic) placement in the isotactic polymer fraction was 0.67 with no external donor and 0.82 in the presence of alkoxysilane external donor.[55] It could indicate the direct participation of donor molecules in isospecific centers. Subsequently, the coordination of donor molecules to TiCl$_4$ is spectroscopically excluded.[56]

Based on detailed $^{13}$C Nuclear Magnetic Resonance (NMR) analysis of the PP chain microstructure, Busico and coworkers demonstrated the presence of the donor molecule in the vicinity of isospecific active species.[57] This model is based on the fact that defects arising from stereoirregular insertions are not randomly distributed along the chain, but are clustered. So the same polymer chain can contain, not only highly isotactic blocks, but weakly isotactic and syndiotactic blocks. This means that the active site can isomerize between the three different propagating species. The three sequences can be present in both isotactic and atactic fractions, but the relative proportions should vary. The relative contributions of these sequences can be related to site transformations involving the presence or absence of steric hindrance in the vicinity of active species. $^{13}$C NMR studies have indicated that the presence of $C_1$-symmetric active species in MgCl$_2$-supported catalysts. With a mechanism of isotactic propagation, which is analogous to that for certain $C_1$-symmetric metallocenes, in the sense that propylene insertion at a highly enatioselective site tends to be followed by chain 'back-skip' rather than a less 'regio and stereoselective' insertion when the chain is in the coordination position previously occupied by the monomer.[58] It is proposed thata (temporary) loss of steric hindrance from one side of an active species with local $C_2$- symmetry giving a $C_1$- symmetric species, may result in a transition from highly isospecific to moderately isospecific propagation. The loss of steric hindrance on both sides can lead to sydiospecific propagation. If the presence of a donor molecule creates steric

hindrance near to the active species, and that the coordination of such donor molecule is reversible, the above model provides a clarification for the fact that strongly-coordinating, stereorigid donors usually give a polymer chain in which highly isotactic sequences predominate.[59] The three-site model proposed by Busico and coworkers (Figure 1.9), describes the stereospecificty of supported Ti species is influenced by the presence or absence of bulky ligands at the neighbouring under-coordinated metal sites; and independent of the location [on (110) or (104)] and nuclearity (monomeric or dimeric).[57] Now, it is generally believed that donor molecules adsorb on $MgCl_2$ and interact with nearby Ti species in a non-bonded manner to improve the stereospecificity of the Ti species. A number of types of active species, where the presence of a donor in the vicinity of the active Ti atom is required for high isospecificity, have been proposed, though the precise structure of the active species is still not resolved.[60]
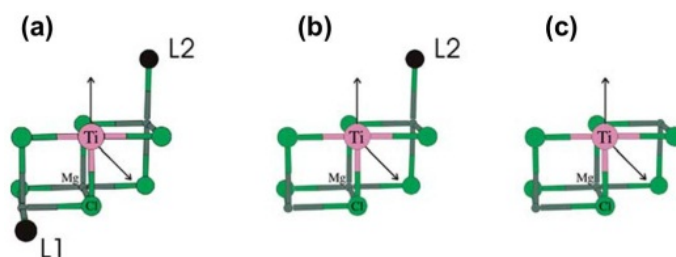


**Figure 1.9.** *3 site model of possible active species for (a) highly isotactic, (b) isotactoid and (c) syndyotactoid propagation.*[57]

The microstructure and physical properties of polypropylene depends greatly on the polymerization catalyst used for its production.[30] This is the reason why one of the of the traditional methods employed to get information on the Ziegler-Natta catalyst structure is the investigation, not of the catalyst itself, but of the polymer it produces and of its response to catalyst variables. Unfortunately, this method is not sensitive enough to get a comprehensive description of the catalyst. Therefore, any attempt to tune the catalyst properties is necessarily a trial-and-error approach. An aromatic monoester (mostly ethyl benzoate) was used as an internal donor in the third generation of $MgCl_2$-supported Ziegler-Natta catalyst.[25] Addition of *p*-toluate as an external donor improved stereospecificity of the catalyst.[61] When the catalyst comes into contact with $AlR_3$, a large quantity of internal donor is lost due to

17

alkylation and/or complexation reactions. When the external donor is absent, poor stereospecificity is obtained due to the loss of steric bulk in the vicinity of the active species. Upon the interaction of an external donor with catalyst components, substitution of the internal donor by the external donor has been indicated.[55,62,63] In the search for donors giving catalysts with improved performance, it was thought that bidentate donors such as phthalate diesters should be able to form strong chelating complexes with tetracoordinate Mg atoms on the (110) edge of $MgCl_2$ and/or binuclear complexes with two pentacoordinate Mg atoms on the (104) edge.[42] Sacchi and coworkers observed that selectivity of $MgCl_2/TiCl_4/EB$ based catalyst increased upon adding any type of external donor, whereas the selectivity of $MgCl_2/TiCl_4$/dialkyl phthalate was markedly increased only when phenyltriethoxysilane was used as external donor.[55,63] This clearly shows that the effectiveness of a catalyst system depends more on the combination or choice of donor rather than on the individual internal or external donor.[63] Later on alkoxysilanes were used as external donor in combination with all different classes of internal donors. However, alkoxysilanes cannot be used as internal donors due to the reaction with the $TiCl_4$ present during catalyst preparation. The search for an internal donor, which binds strongly to $MgCl_2$ surface even in the presence of $AlR_3$ result in the discovery of 2,2-disubstituted-1,3-dimethoxypropanes.[42,64] The best performance in terms of productivity and isotacticity was obtained when the bulkiness of substituents at 2-position resulted in a diether having a most probable conformation with an oxygen-oxygen distance in the range of 2.8 – 3.2 Å.[65] Table 1.1 shows the evolution of Ziegler-Natta catalyst. Figure 1.10 represents chemical structures of different donors used in industry.
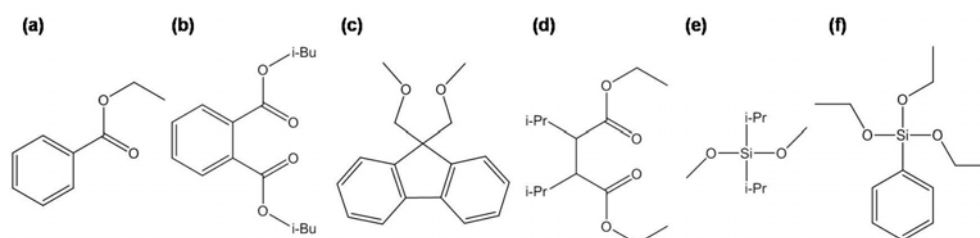


**Figure 1.10.** *Chemical structures of donors. (a) ethyl benzoate – EB. (b) diisobutyl phthalate – DIBP. (c) 9,9-bis(methoxymethyl)fluorene-*

18

*BMMF. (d) 2,3-diisopropyl diethyl succinate – DIPS. (e) diisopropyl dimethoxy silane – DPDS. (f) phenyl triethoxy silane – PTES.*

**Table 1.1.** *Generations of Ziegler-Natta catalysts for the propylene polymerization.*

| Generation / year | Catalyst composition | Productivity ($kg_{PP}/g_{cat}$) | Selectivity/I.I. (%) |
|---|---|---|---|
| First (1954) | $\delta$-TiCl$_3$.0.33AlCl$_3$+AlEt$_2$Cl | 2 – 4 | 90 – 94 |
| Second (1970) | $\delta$-TiCl$_3$+AlEt$_2$Cl | 10 – 15 | 94 – 97 |
| (1968) | MgCl$_2$/TiCl$_4$+AlR$_3$ | 15 | 40 |
| Third (1971) | MgCl$_2$/TiCl$_4$/benzoate + AlR$_3$/benzoate | 15 – 30 | 95 – 97 |
| Fourth (1980) | MgCl$_2$/TiCl$_4$/phthalate + AlR$_3$/Silane | 40 – 70 | 95 – 99 |
| Fifth (1988) | MgCl$_2$/TiCl$_4$/diether + AlR$_3$ | 100 – 130 | 95 – 98 |
| | MgCl$_2$/TiCl$_4$/diether + AlR$_3$/silane | 70 – 100 | 98 – 99 |
| 'Next' (1999) | MgCl$_2$/TiCl$_4$/succinate + AlR$_3$/silane | 40 – 70 | 95 – 99 |

(Polymerization conditions: liquid propylene, 70 °C, H$_2$)

## 1.3 Research in catalysis

### 1.3.1 Ultimate goal of catalysis research

The past decades, catalysis research have evolved from the description of catalysis to understanding reaction mechanisms and kinetics at a molecular level and be able to relate it to the exact composition and structure of the catalyst. The evolution of catalysis research will –hopefully– ultimately lead to the prediction of

an industrial catalyst that is able to produce the desired products under the ideal reaction conditions (rather eco-friendly).

In the industry, most of the research is focused on exploiting a catalyst rather than understanding it. Generally, development and optimization of catalysts are based on empirical knowledge about the effect of preparation methods, additives, and different carriers on the reaction. The heterogeneous catalysts developed by these ways are very complex mixtures with a broad diversity of compounds. Regardless of continuous research, knowledge of the active site and/or reaction mechanism remains unclear. Therefore, better fundamental understanding is demanded, which requires the application of spectroscopic and microscopic techniques to characterize the active catalyst, coupled with catalyst testing.

In the case of Ziegler-Natta catalysts, the barriers to achieve this goal were the complexity of the high-surface-area micro-porous catalyst, the extreme sensitivity of the catalyst to oxygen and moisture and the lack of spectroscopic data detecting the active sites during polymerization.[66] When using microscopic techniques, the crystalline primary particles of $MgCl_2$ support tend to expose the coordinatively saturated basal (001) planes, which is of no interest for catalysis.[39] The catalyst has a multi-site nature because of the heterogeneity of the support.[32] Beside the multi-site nature conferred by the support, they are constituted by many components, each one responsible for a specific function, and often interacting together.[67] Furthermore the number of active species may represent only a small proportion of the total transition metal present in the system, which makes it indistinguishable from the inactive phases, in turn hard to assign the macroscopic properties of the catalyst to the microscopic structure.[66]

## 1.3.2 The flat-model approach

A partial solution to the challenges in the catalyst research can be the development of model catalysts. A model catalyst will be a much simplified version of the existing catalyst system as the industrial support is removed or altered; the promoting agents may be missing. Overall, the design of a model catalyst is a compromise between achieving a simple well definable and controllable catalyst and resembling the original industrial catalyst to maintain relevance.[68]

20

A well-known class of model catalyst is single crystals, which possess known geometry of surface atoms, dependent on the direction of the cleavage and the crystal structure; for instance, Rh(111), Rh(100), MgO (100) or $TiO_2$(110). Single crystals have been used to understand the intrinsic kinetics of catalytic reactions by studying adsorption, desorption and surface coverage and lateral interaction of co-adsorbates.[69,70] Interactions between the near to perfect single crystal and adsorbates are compared with the interaction of adsorbates on the 'perfect'/defect–free surfaces modeled by Density Functional Theory (DFT), and vice versa.[71]

An alternative way to design the model catalyst is the utilization of a flat and inexpensive silicon disc covered with a thin film of $SiO_2$.[72] These $SiO_2$/Si(100) systems are convenient and realistic models for a silica support.[73-78] Moreover, it is relatively straightforward to apply $TiO_2$ or $Al_2O_3$ by wet chemical reactions using titanium alkoxide, or evaporating or sputtering aluminium onto the surface, respectively.[79]

Schematic drawings in Figure 1.11 show the differences in an industrial catalyst, model catalyst on a flat support and an unsupported single crystal model catalyst.

In the case of Ziegler-Natta catalyst, the support ($MgCl_2$) can be easily be deposited over $SiO_2$/Si(100), by means of spin coating from ethanol solution.[80-83]
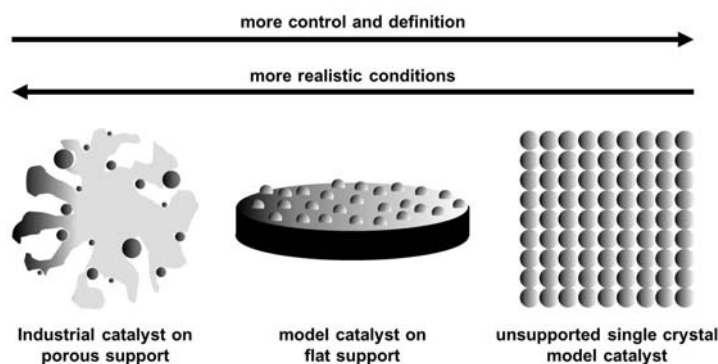


**Figure 1.11.** *Schematic drawings of (left) conventional porous catalyst; (middle) a model supported catalyst with catalytically active*

*phase on a thin layer of flat material; (right) a well-defined single crystal model catalyst.*

The planar geometry of supported model catalysts offers a number of advantages;[79]

- All catalytically active particles in the system are exposed, and not hidden in the pores. The surface that is probed by spectroscopy techniques is identical to the active surface. It is easier to achieve a correlation between catalyst activity and surface characterization; which can be done on the same material.

- For mechanistic studies, the absence of pores results in the absence of diffusion limitations, with the attractive advantage that a wider temperature range can be accessed for studying the kinetics.

- The conductivity of the model support helps to minimize the effects of charging on applying techniques like X-ray photoelectron spectroscopy (XPS) and scanning electron microscopy (SEM).

- The extremely flat surface facilitates the application of scanning probe techniques like Atomic Force Microscopy (AFM), which makes it possible to visualize the catalytic surface at a nanometer resolution.

- When a flat active surface used to model and test polymerization catalysts, the polymer growth occurs in a direction normal to the catalyst plane to form a film. This well-defined polymer growth can be used as a tool to obtain information of the active catalyst on a micrometer scale.

However, the flat-model catalyst also have some characteristic disadvantages; especially in terms of activity measurement and its interpretation.

- Since the active phase is distributed on a very small area (dimensions in orders of centimeters), the amount of active material is extremely small. As a result, the catalyst is very sensitive to impurities, and extreme care should be taken in interpreting the activity data. Reproducible activities similar to the conventional systems are indispensable in proving similarity with industrial catalysts.

- The small amount of active materials results in small yields in absolute terms. This can trouble the catalytic testing and analysis of reaction products.

In our group, this flat-model approach has been successfully applied to iron oxide nanoparticles in Fischer-Tropsch catalysts,[84-86] Philips catalyst for ethylene polymerization,[73-78,87-91] immobilized homogenous catalysts for ethylene polymerization[92-95] and recently, Ziegler-Natta catalyst for ethylene and propylene polymerization.[80-83,96]

## 1.3.3 The flat Ziegler-Natta model catalysts

The pioneering works in the field of model Ziegler-Natta catalysts belong to the group of Somorjai and coworkers,[66,97-103] who established an experimental route to prepare model Ziegler-Natta catalysts on a single crystal surface. Epitaxial $MgCl_2$ films were grown on a large variety of clean metal surfaces, such as polycrystalline Au(gold foil), Pd(111) and Pd(100), through thermal evaporation of molecular $MgCl_2$ under UHV conditions. $TiCl_4$ was successively anchored to the defective $MgCl_2$ surfaces by following different methods, among which the vapor deposition under electron bombardment was the most employed. Somorjai and coworkers used XPS to analyze the active species on the catalyst surface after exposing to the cocatalyst. Later, Freund and coworkers successfully applied the Electron Paramagnetic Resonance (EPR) technique to characterize similar model systems.[104-106] The EPR technique was able to prove (for the first time) the formation of alkyl radicals during the alkylation process.[105,106] Finally, ethylene polymerization was successfully performed on these model catalysts.

Sioku and Ntais introduced a surface science model of Ti-based Ziegler-Natta catalyst supported on $SiO_2/Si(100)$ prepared by spin coating THF solutions of $TiCl_4.(THF)_2$ and $MgCl_2/TiCl_4.(THF)_2$.[107,108] The surface composition was characterized by XPS. However, these authors did not report any activity data for ethylene and propylene polymerization.

Earlier, in our group, Andoni and coworkers developed an active flat model system for Ziegler-Natta catalyst.[96] The synthesis method involves the spin coating of a $MgCl_2$ solution (with or without electron donor) in ethanol on a flat silicon wafer. Subsequent treatment with $TiCl_4$ and $AlEt_3$ resulted in an active ethylene and propylene polymerization catalyst.[80,81] Incorporation of different internal donors (such as diether and esters) in the $MgCl_2$crystal growth process (Ostwald ripening) generated large crystallites and provided strong evidence that the

distribution of the active species in Ziegler-Natta depends on the nature of the internal donor; as a consequence of the ability of internal donor to steer the formation of a particular $MgCl_2$ crystallite face during catalyst preparation.[82,83] Employing scanning force and electron microscopy, it was found that, in the absence of electron donors, the crystals grow as thin hexagonal prisms, which indicates that one kind of lateral termination is predominant. The same morphology was obtained in the presence of 1,3 diethers, whereas crystals with chemisorbed ethyl benzoate or diisobutyl phthalate exhibited basal planes with extra 90° angles calling for the presence of two different lateral terminations.[82,83] However, molecular level information about coordination modes and coordination sites of internal donor was unclear.

## 1.4 Role of infrared spectroscopy in Ziegler-Natta catalysis

The infrared spectrometer was probably the first instrument used for the characterization of catalyst (CO adsorption on copper).[109] Infrared spectrum is sensitive to the molecular properties of the investigated samples, such as type of atoms, chemical bonding, geometry, and intra/intermolecular interactions. Moreover, the spectra successfully provide surface structural information, because of their ability to discriminate between different species that may simultaneously be present in the investigated system.[110-112]

Infrared spectroscopy was extensively used to characterize Ziegler-Natta catalysts.[113-128] The majority of the studies is devoted to the characterization of complexes between the catalyst precursors and the electron donor molecules added to improve the stereo-specificity in α-olefin polymerization. Intense IR absorption bands characteristic of the chemical group directly interacting with Mg or Ti centers (e.g., C-O stretching vibrations in ethyl benzoate, dialkyl phthalate or diether donors) were used as markers of complexation. Due to the formation of different complexes of donor with $MgCl_2$ and $TiCl_4$, the envelope of $\nu(C=O)$ is always broad. Some attempts were made to estimate the distribution of donor in different complexes by means of resolving the $\nu(C=O)$ band into components.[117,120,121,123] The peak positions of the components selected for resolving the spectra were taken from the spectra of $MgCl_2$-donor molecular

24

complexes.[115-117] In all these cases, the components used to explain the spectra were really broad. The adjacently positioned components cause large errors in the quantification due to covariance.

Very often, in the absence of other experimental results obtained by complimentary techniques, the vibrational spectra were interpreted by means of quantum chemical calculations performed on selected models. For instance, the geometries of 9,9-bis(methoxymethyl)fluorene as an internal electron donor were investigated by Brambilla and coworkers.[126] By combining the data from experiment (infrared absorption) and theory (quantum chemical calculations), the authors gained convincing evidence to propose the conformations of the pure donor, the donor complexed with $MgCl_2$ and the donor in the $MgCl_2/TiCl_4$ system.

Earlier, in our group, the flat model Ziegler-Natta catalyst has been optimized for investigation by means of *in-situ* attenuated total internal reflection - Fourier transform infrared spectroscopy (*in-situ* ATR-FTIR). Preliminary results on the interaction of electron donor with $MgCl_2$ and $MgCl_2/TiCl_4$ were reported.[124] ATR-FTIR has been used to monitor *in-situ* ethylene polymerization over flat model Ziegler-Natta catalyst and immobilized homogenous catalyst.[80,124]

## 1.5 Scope of the thesis

This project intends to extend the research on flat-model Ziegler-Natta catalyst system developed by Andoni and coworkers, especially in achieving;

- Identification of the active surfaces on $MgCl_2$
- A quantitative description of surface Mg ion interaction with internal donors having industrial relevance.

These objectives can be achieved by a combined experimental and computational approach. $MgCl_2$ surface sites for internal donor coordination and the geometry of adsorbed internal donor can be modeled by density functional theory including dispersion (DFT-D). The vibrational spectra of adsorbed internal donor also can be simulated by DFT. Computational modelling was performed by our collaborators at the University of Naples (Maddalena D'Amore and Vincezo Busico).

25

We can perform a systematic *in-situ* ATR-FTIR study on the flat-model MgCl$_2$ supports (prepared by spin coating impregnation) with respect to their interaction with electron donors (in the hydrocarbon solution or already present in the MgCl$_2$ film) as a function of temperature and concentration, and subsequently to their α-olefin polymerization performance. Changes in the coordination modes and coordination sites of internal donor can be detected by the shifts in experimental IR bands. Active MgCl$_2$ surface sites for internal donor coordination and the corresponding surface complexes of internal donors were identified in the DFT study of our collaborators. Reconciling the information from experimental and simulated IR bands provide a more accurate picture of active species on Ziegler-Natta catalysts.

Our choice of internal donor is diisobutyl phthalate (DIBP). The presence of DIBP in the film can be easily identified by the strong carbonyl signal in the IR spectra. As a bidentate donor, different binding modes are possible for the coordination on MgCl$_2$ surface. Moreover, DIBP is believed to bound on both lateral surface terminations of MgCl$_2$. Since, DIBP is an internal donor used in Ziegler-Natta catalyst industry, lot of IR studies have already been performed on MgCl$_2$/DIBP complexes. The *in-situ* capabilities of our ATR-FTIR setup allowed us to gain a more detailed insight into the DIBP adsorption.

## 1.6 Outline of the thesis

- **Chapter 1** (present chapter) gives a literature review on the current understanding of the surface chemistry of MgCl$_2$ supported Ziegler Natta catalyst support. We provide the project aim and the methodology to achieve the aim.
- **Chapter 2** explains in detail the preparation of the model catalyst, including a description of the spin coating impregnation method. Finally, the most important spectroscopy and microscopy techniques applied in this thesis are introduced and elaborated.
- **Chapter 3** introduces a method to quantify internal donor in MgCl$_2$/DIBP films. Using F – labeled DIBP donor estimation of donor in MgCl$_2$ films. Based on the current understanding on surface chemistry of MgCl$_2$/DIBP

complexes, a model is developed to explain the $MgCl_2$ – DIBP interactions at different temperatures and donor loading.

- **Chapter 4** describes the method to isolate various DIBP species coordinated exclusively (or almost exclusively) on one type of $MgCl_2$ surface sites. With the help of DFT-D (performed by our collaborators in University of Naples), the plausible surface species of DIBP on $MgCl_2$ are identified. The morphology of $MgCl_2$/DIBP film and its changes upon temperature changes is studied by TEM.

- In **Chapter 5** we attempt to combine the results of the DFT study (from the collaborators) with our experimental ATR-FTIR observations in order to create a molecular level picture of the dynamic interplay of $MgCl_2$ surface structure and DIBP adsorption. Based on experimental and simulated DIBP spectra of various $MgCl_2$/DIBP surface species, we derived a set of components to resolve the $\nu(C=O)$ band of DIBP. With this model, we can explain the influence of internal donor on the relative stability of $MgCl_2$ surface sites.

- **Chapter 6** deals with *in-situ* polymerization of propylene over flat-model Ziegler-Natta catalyst discussed in previous chapters. We also discuss the potential of ATR-FTIR setup to estimate the catalyst performance (in terms of activity and selectivity).

- **Chapter 7** comprises an overview/evaluation of the most important results of the thesis along with perspectives for future research.

## 1.7 References

(1) Armor, J. N. *Catal. Today* **2011,** *163,* 3.
(2) Berzelius, J. J. *Royal Swedish Academy of Sciences* **1835.**
(3) Berzelius, J. J. *Annls. Chim. Phys.* **1836,** *61,* 146.
(4) *World Catalysts to 2016;* Freedonia, **2013,** *2989.*
(5) *Recognizing the Best in Innovation: Breakthrough Catalyst*; R&D Magazine, **2005,** 20.
(6) Anastas, P. T.; Warner, J. C. *Green Chemistry: Theory and Practice;* Oxford University Press: Oxford, **1998.**
(7) Chorkendorff, I.; Niemantsverdriet, J. W. (Hans).*Concepts of Modern Catalysis and Kinetics;* WILEY-VCH: Weinheim, **2003.**
(8) Braunschweig, H.; Breitling, F. M.. *Coord. Chem. Rev.* **2006**, *250,* 2691.
(9) Kaminsky, W.; Arndt, M. *Adv. Poly. Sci.* **1997**, *127*, 143.

(10) Moolji,S. IOCL conclave, **2013;**
http://www.petrochemconclave.com/presentation/2013/Mr.SMoolji.pdf

(11) Peacock, A. J. *Handbook of polyethylene: Structure, Properties and Applications;* Marcel Deckcer: New York, **2000.**

(12) Resconi, L.; Cavallo, L.; Fait, A.; Fabrizio, P. Chem. Rev. **2000**, *100*, 1253.

(13) Fawcett, E. W.; Gibson, R. O.; Perrin, M. W.; Patton, J. G.; Williams, E. G., GB 471590, Imperial Chemical Industries Ltd., **1937.**

(14) Hogan, J. P.; Banks, R. L., US 2825721, Phillips Petroleum Company., **1958.**

(15) Ziegler, K. *Angew. Chem.***1952**, *64*, 323.

(16) Ziegler, K.; Holzkamp, E.; Breil, H.; Martin, H. *Angew. Chem.***1955**, *67,* 541.

(17) Natta, G.; Pino, P.; Corradini, P.; Danusso, F.; Mantica, E.; Mazzanti, G.; Moraglio, G. *J. Am. Chem. Soc.***1955**, *77*, 1708.

(18) Natta, G. *Angew. Chem.***1956**, *68*, 393.

(19) Cecchin, G.; Morini, G.; Piemontesi, F. *Kirk-Othmer Encyclopedia of Chemical Technology;* WILEY: **2003,***26,* 502.

(20) Albizzati, E.; Cecchin, G.; Chadwick, J. C.; Collina, G.; Giannini, U.; Morini G.; Noristi, L. *Polypropylene Handbook;* Pasquini, N., Ed.; Hanser Publishers: Munich, **2005.**

(21) Boor, J. *Ziegler-Natta Catalysis and Polymerizations;* Academic Press: New-York, **1979.**

(22) Hermans, J. P.; Henrioulle, P., US 4210738, Solvay **1972.**

(23) Galli, P.; Mayr, A.; Susa, E.; Drusco, D, G.; Giachetti, E., US 4298718, Montedison, **1981.**

(24) Albizzati, E.; Galimberti, M. *Catal. Today.* **1998,** *41*, 159.

(25) Giannini, U.; Cassata, A.; Longi, P.; Mazzochi, R., US 4336360, Monedison, **1982.**

(26) Kashiwa, N. *J. Polym. Sci. A: Polym. Chem.* **2004,** *42,*1.

(27) Cossee, P.*Tetrahedron Lett.* **1960,** *17*, 17.

(28) Cossee, P.*J. Catal.* **1964,** *3*, 80.

(29) Arlman, E. J.; Cossee, P.*J. Catal.* **1964,** *3*, 99.

(30) Chadwick, J. C. *Ziegler-Natta Catalysts: Encyclopedia of Polymer Science and Technology;* WILEY: **2003.**

(31) Corradini, P.; Busico, V.; Gurrea, G. *Comprehensive Polymer Science;* Pergamon Press,**1998.**

(32) Auriemma, F.; De Rosa, C. *J. Apll. Cryst.* **2008,** *41,* 68.

(33) Partin, D. E.; O'Keeffe, M.*J. Solid State. Chem.* **1991,** *95,* 176.

(34) Bassi, I. W.; Polato, F.; Calcattera, M.; Bart, J. C. J. *Z. Kristallogr.* **1982,** *159,* 297.

(35) Trubitsyn, D. A.; Zakharov, V, A.; Zakharov, I. I. *J. Mol. Catal. A: Chem.* **2007,** *270*, 164.

(36) Goodball, B. L. *Polypropylene and other Polyolefins: Polymerizations and Characterizations;* van der Ven, S., Ed.; Elsevier: Amsterdam **1990.**

(37) Marigo, A.; Marega, R.; Zanneti, G.; Morini, G.; Ferrara, G. *Eur. Polym. J.* **2000,** *36,* 1921.

(38) Giannini, U. *Macromol. Chem. Suppl.* **1981,** *5*, 216.

(39) Busico, V.; Causa, M.; Cipullo. R.; Credendino, R.; Cutillo, F.; Friederichs, N.; Lamanna, R.; Segre, A.; Castelli, V. V. A. *J. Phys. Chem C* **2008,** *112*, 1081.

(40) Busico, V.; Corradini, P.; de Martino, L.; Proto, A.; Savino, V.; Albizzati, E. *Makromol. Chem.* **1985,** *186,* 1279.

(41) Busico, V.; Corradini, P.; de Martino, L.; Proto, A.; Albizzati, E. *Makromol. Chem.* **1986,** *187,* 1115.

(42)    Albizzati, E.; Giannini, U.; Morini, G.; Smith, C. A.; Ziegler, R. C. In *Ziegler Catalysts: Recent Scientific Innovations and Technological Improvements;* Flink, G.; Mülhaupt, R.; Brintzinger, H. H., Eds.; Springer-Verlag: Berlin, **1995.**

(43)    Soga, K.; Chen, S. I.; Ohnishi, R. *Polym. Bull.* **1982,** *8,* 473.

(44)    Chadwick, J. C.; Garoff, T.; Severn, J. R. *Tailor-Made Polymers via Immobilization of Alpha-Olefin Polymerization Catalysts;* Severn, J. R.; Chadwick, J. C., Eds.; WILEY-VCH: Weinheim, **2008,** Ch.2.

(45)    Kakugo, M.; Sadathoshi, H.; Yokoyama, K.; Kojima, K. *Macromolecules* **1989,** *22,* 547.

(46)    Kakugo, M.; Sadathoshi, H.; Sakai, J.; Yokoyama, M. *Macromolecules* **1989,** *22,* 3172.

(47)    Murry, R. T.; Pearce, R.; Platt, D. *J. Polym. Sci., Polym. Lett. Ed.* **1978,** *16,* 303.

(48)    Higuchi, T.; Liu, B.; Nakatani, H.; Otsuka, N.; Terano, M. *Appl. Surf. Sci.* **2003,** *214,* 272.

(49)    Barbe, P. C.; Noristi, L.; Baruzzi, G.; Marchetti, E. *Makromol. Chem. Rapid. Commun.* **1983,** *4,* 249.

(50)    Mori, H.; Sawada, M.; Higuchi, T.; Hasebe, K.; Otsuka, N.; Terano, M. *Macromol. Rapid. Commun.* **1999,** *20,* 245.

(51)    Mori, H.; Higuchi, T.; Otsuka, N.; Terano, M. *Macromol. Chem. Phys.* **2000,** *201,* 2789.

(52)    Oleshko, V. P.; Crozier, P. A.; Cantrell, R. D.; Westwood, A. D. *J. Electron. Microsc.* **2002,** *51(Supplement)*, S27.

(53)    Zambelli, A.; Ammendola, P. *Prog. Polym. Sci.* **1991,** *16,* 203.

(54)    Sacchi, M. C.; Tritto, I.; Locatelli, P. *Prog. Polym. Sci.* **1991,** *16,* 331.

(55)    Sacchi, M. C.; Forlini, F.; Tritto, I.; Mendichi, R.; Zannoni, G.; Noristi, L *Macromolecules* **1992,** *25,* 5914.

(56)    Terano, M.; Kataoka, T.; Keii, T. *Macromol. Chem.* **1987,** *188,* 1477.

(57)    Busico, V.; Cipullo, R.; Monaco, G.; Talarico, G.; Vacatello, M.; Chadwick, J. C.; Segre, A. L.; Sudmeijer, O. *Macromolecules* **1999,** *32,* 4173.

(58)    Busico, V.; Cipullo, R.; Talarico, G.; Serge, A. L.; Chadwick, J. C. *Macromolecules* **1997,** *30,* 4786.

(59)    Chadwick, J. C.; Morini, G.; Balbontin, G.; Camaruti, I.; Heere, J. J. R.; Mingozzi, I.; Testoni, F. *Macromol. Chem. Phys.* **2001,** *202,* 1995.

(60)    Barino, L.; Scordamaglia, R. *Makromol. Theory. Simul.* **1998,** *7,* 407.

(61)    Kakugo, M.; Miyatake, T.; Naito, Y.; Mizunumz, K. *Macromolecules* **1988,** *21,* 314.

(62)    Noristi, L.; Barbé, P. C.; Baruzzi, G. *Macromol. Chem.* **1991,** *192,* 1115.

(63)    Sacchi, M. C.; Tritto, I.; Shan, C.; mendichi, R.; Norisuti, L. *Macromolecules* **1992,** *24,* 6823.

(64)    Albizzati, E.; Giannini, U.; Morini, G.; Galimberi, M.; Barino, L.; Scordamaglia, R *Macromol. Symp.* **1995,** *89,* 73.

(65)    Barino, L.; Scordamaglia, R. *Macromol. Symp.* **1995,** *89,* 101.

(66)    Kim, S, H.; Somorjai, G. A. *Surf. Inetrface. Anal.* **2001,** *31,* 701.

(67)    Soga, K.; Shiono, T. *Prog. Polym. Sci.* **1997,** *22,* 1503.

(68)    Gunter, P. L. J.; Niemantsverdriet, J. W. (Hans).; Ribeiro, F. H.; Somorjai, G. A. *Catal. Rev.* **1997,** *39,* 77.

(69)    Nieskens, D. L. S.; van Bavel, A. P.; Niemantsverdriet, J. W. (Hans). *Surf. Sci.* **2003,** *564,* 159.

(70)  van Bavel, A. P.; Hopstaken, M. J. P.; Currulla, D.; Niemantsverdriet, J. W. (Hans).; Lukkien, J. J.; Hilbers, P. A. J. *J. Chem. Phys.* **2003,** *119*, 524.

(71)  Nieskens, D. L. S.; van Bavel, A. P.; Curulla Ferre, D.; Niemnatsverdriet, J. W. (Hans). *J. Phys. Chem. B.* **2004,** *108,* 14541.

(72)  Niemantsverdriet, J. W. (Hans).; Engelen, A. F. P.; de Jong, A. M.; Wieldraaijer, W.; Kramer, G. J. *Appl. Surf. Sci.* **1999,** *144-145,* 366.

(73)  Thüne, P. C.; Loos, J.; Wouters, D.; Lemstra, P. J.; Niemantsverdriet, J. W. (Hans). *Macromol. Symp.* **2001,** *173*, 37.

(74)  Thüne,P. C.; Loos, J.; Weingarten, U.; Müller, F.; Kretschmer, W.; Kaminsky, W.; Lemstra, P. J.; Niemantsverdriet, J. W. (Hans). *Macromolecules* **2003,** *36*, 1440.

(75)  Thüne,P. C.; Verhagen, C. P. J.; van den Boer, M. J. G.; Niemantsverdriet, J. W. (Hans). *J. Phys. Chem. B.* **1997,** *101*, 8559.

(76)  Thüne,P. C.; Loos, J.; Lemstra, P. J.; Niemantsverdriet, J. W. (Hans). *J. Catal.* **1999,** *183*, 1.

(77)  Thüne,P. C.; Loos, J.; de Jong, A. M.; Lemstra, P. J.; Niemantsverdriet, J. W. (Hans). *Top. Catal.* **2000,** *13*, 67.

(78)  Thüne,P. C.; Linke, R.; van Gennip, W. J. H.; de Jong, A. M.; Niemantsverdriet, J. W. (Hans). *J. Phys. Chem. B.* **2001,** *105*, 3073.

(79)  Thüne,P. C.; Niemantsverdriet, J. W. (Hans). *Surf. Sci.* **2009,** *603*, 1756.

(80)  Andoni, A.; Chadwick, J. C.; Milani, S.; Niemantsverdriet, J. W. (Hans).; Thüne, P. C. *J. Catal.* **2007,** *247* (2), 129.

(81)  Andoni, A.; Chadwick, J. C.; Niemantsverdriet, J. W. (Hans).; Thüne, P. C. *Macromol. Symp.* **2007,** *260,* 140.

(82)  Andoni, A.; Chadwick, J. C.; Niemantsverdriet, J. W. (Hans).; Thüne, P. C. *Macromol. Rapid Commun.* **2007,** *28* (14), 1466.

(83)  Andoni, A.; Chadwick, J. C.; Niemantsverdriet, J. W. (Hans).; Thüne, P. C. *J. Catal.* **2008,** *257,* 81.

(84)  Moodley, P., *Iron Nanoparticulate Planar Model Systems – Synthesis and Applilcations;* Ph. D Thesis., Eindhoven University of Technology: The Netherlands, **2010.**

(85)  Moodley, P.; Loos, J.; Niemantsverdriet, J. W. (Hans).; Thüne, P. C. *Carbon* **2009,***47* (8), 2002.

(86)  Moodley, P.; Scheijen, F. J. E.; Niemantsverdriet, J. W. (Hans).; Thüne, P. C. *Catal. Today* **2010,** *154,* 142.

(87)  Thüne, P. C., *A Surface Science Model for the Phillips Ethylene Polymerization Catalyst;* Ph. D Thesis., Eindhoven University of Technology: The Netherlands, **2000.**

(88)  van Kimmenade, E. M. E., *Ethylene Polymerization over Flat Phillips Model Catalysts;* Ph. D Thesis., Eindhoven University of Technology: The Netherlands, **2006.**

(89)  van Kimmenade, E. M. E.; Kuiper, A. E. T.; Tamminga, Y.; Thüne, P. C.;Niemantsverdriet, J. W. (Hans). *J. Catal.* **2004,** *223* (1), 134.

(90)  van Kimmenade, E. M. E.; Loos, J.; Niemantsverdriet, J. W. (Hans).; Thüne, P. C. *J. Catal.* **2006,** *240* (1), 39.

(91)  Thüne, P. C.; Loos, J.; Cheng, Y.; van Kimmenade, E. M. E.; Kong, B. L.;  Niemantsverdriet, J. W. (Hans). *Top. Catal.* **2007,** *46*, 239.

(92)   Han, W., *Supported Homogenous Catalysts on Flat Model Surfaces for Ethylene Polymerization;* Ph. D Thesis., Eindhoven University of Technology: The Netherlands, **2007.**

(93)   Han, W.; Müller, C.; Vogt, D.; Niemantsverdriet, J. W. (Hans).; Thüne, P. C. *Macromol. Rapid. Commun.* **2006,** *27,* 279.

(94)   Han, W.; Wu, D.; Ming, W.; Niemantsverdriet, J. W. (Hans).; Thüne, P. C. *Langmuir* **2006,** *22* (19), 7956.

(95)   Han, W.; Niemantsverdriet, J. W. (Hans).; Thüne, P. C. *Macromol. Symp.* **2007,** *260,* 147.

(96)   Andoni, A., *A Flat Model Approach to Ziegler-Natta Olefin Polymerization Catalysts;* Ph. D Thesis., Eindhoven University of Technology: The Netherlands, **2009.**

(97)   Magni, E.; Somorjai, G. A. *J. Phys. Chem.* **1996,** *100*, 14786.

(98)   Magni, E.; Somorjai, G. A. *Surf. Sci.* **1996,** *354*, 1.

(99)   Magni, E.; Somorjai, G. A. *Surf. Sci.* **1997,** *377*, 824.

(100)  Magni, E.; Somorjai, G. A. *J. Phys. Chem. B.* **1998,** *102*, 8788.

(101)  Koranyi, T. I.; Magni, E.; Somorjai, G. A. *Top. Catal.* **1999,** *7*, 179.

(102)  Kim, S. H.; Somorjai, G. A. *J. Phys. Chem. B.* **2000,** *104*, 5519.

(103)  Kim, S. H.; Somorjai, G. A. *J. Phys. Chem. B.* **2002,** *106*, 1386.

(104)  Schmidt, J.; Risse, T.; Hamann, H.; Freund, H. J. *J. Chem. Phys.* **2002,** *116*, 10861.

(105)  Risse, T.; Schmidt, J.; Hamann, H.; Freund, H. J. *Angew. Chem., Int. Ed.* **2002,** *41*, 1518.

(106)  Freund, H. J.; Baumer, M.; Libuda, J.; Risse, T.; Rupprechter, G.; Shaikhutdinov, S. *J. Catal.* **2003,** *216*, 223.

(107)  Siokou, A.; Ntais, S. *Surf. Sci.* **2003,** *540*, 379.

(108)  Siokou, A.; Ntais, S. *Surf. Sci.* **2003,** *600*, 4216.

(109)  Eischens, R. P.; Pliskin, W. A.; Francis, S. A. *J. Chem. Phys.* **1954,** *22,* 1786.

(110)  Socrates, G. C. *Infrared and raman Charecteristic Group Frequencies. Tables and Charts,* 3rd Ed.; John Wiley & Sons: Canada, **2001.**

(111)  Duncan, A. B. F.; Gordy, W.; Jones, R. N.; Matsen, F. A.; Sandorfy, C.; West, W. *Chemical Application of Spectroscopy;* Interscience Publisher, Inc.: New York, **1956.**

(112)  Wilson, E. B.; Decius, J. C.; Cross, C. P.*Molecular Vibrations: The Theory of Infrared and Raman Vibrational Spectra;* Dover Publications, **1980.**

(113)  Gordon, D.; Wallbridge, M. G. M. *Inorg. Chim. Acta.* **1984,** *88*, 15.

(114)  Terano, M.; Katakoa, T.; Keii, T. *J. Polym. Sci. A: Polym. Chem.* **1990,** *28*, 2035.

(115)  Arzoumanidis, G. G.; Karayannis, N. M. *Appl. Catal.* **1991,** *76*, 221.

(116)  Song, W. D.; Chu, K. J.; Chang, H. S.; Ihm, S. K. *J. Mol. Catal.* **1993,** *84,* 109.

(117)  Yang, C. B.; Hsu, C. C.; Park, Y. S.; Shurvell, H. F. *Eur. Polym. J.* **1994,** *30* (2), 205.

(118)  Noto, V. D.; Fregonese, D.; Marigo, A.; Bresadola, S. *Macromol. Chem. Phys.* **1998,** *199*, 633.

(119)  Zohuri, G.; Ahmadjo, S.; Jamjah, R.; Nekoomanesh, M. *Iran. Polym. J.* **2001,** *10* (3), 149.

(120)  Potapov, A. G.; Bukatov, G. D.; Zakharov, V. A. *J. Mol. Catal. A: Chem.* **2006,** *246* (1-2), 248.

(121)  Kissin, Y. V.; Liu, X. S.; Pollick, D. J.; Brungard, N. L.; Chang, M. *J. Mol. Catal. A: Chem.* **2008,** *287* (1-2), 45.

(122)   Makwana, U.; Naik, D. G.; Singh, G.; Patel, V.; Patil, H. R.; Gupta, V. K. *Catal. Lett.* **2009,** *131* (3-4), 624.

(123)   Singh, G.; Kaur, S.; Makwana, U.; Patankar, R. B.; Gupta, V. K. *Macromol. Chem. Phys.* **2009,** *210* (1), 69.

(124)   Andoni, A.; Chadwick, J. C.; Niemantsverdriet, J. W. (Hans).; Thüne, P. C. *Catal. Lett.* **2009,** *130,* 278.

(125)   Stukalov, D. V.; Zakharov, V. A.; Potapov, A. G.; Bukatov, G. D. *J. Catal.* **2009,** *266* (1)*,* 39.

(126)   Potapov, A. G.; Bukatov. G. D.; Zakharov. V. A. *J. Mol. Catal. A: Chem.* **2010,** *316* (3-4), 95.

(127)   Brambilla, L.; Zerbi, G.; Piementosi, F.; Nascetti, S.; Morini, G. *J. Phys. Chem.* **2010,** *114,* 11475.

(128)   Potapov, A. G.; Politanskaya, L. V. *J. Mol. Catal. A: Chem.* **2013,** *368*, 159.

# 2

# Experimental and analytical details

# Abstract

*The objective of the present chapter is to explain the experimental work carried out in this thesis. First, we briefly describe the flat-model preparation; including the pre-treatment to flat-model support, preparation of thin films by spin coating technique, and the operating conditions for the Ziegler-Natta catalyst. In addition, we discuss all spectroscopic and microscopic techniques used to investigate the surface chemistry and morphology of the prepared film samples.*

## 2.1 Pretreatments on the planar surface

The carriers for the flat model Ziegler-Natta catalyst system were a silicon wafer or internal reflection crystal of silicon or zinc selenide.

For X-ray photoelectron spectroscopy (XPS) studies, a Si wafer having a typical size of 20 x 20 mm$^2$ was used. The preparation of the SiO$_2$/Si(100) surface has been previously investigated and explained in the research conducted in our group.[1-4] The silicon disc is initially cut into 20 x 20 mm$^2$ size wafers and calcined in the air at 750 °C for 24 hours to grow a thin SiO$_2$ layer of several nanometers (~ 20 nm). After cooling down, the samples were placed in a 1:1 volumetric mixture of NH$_4$OH (25%) and H$_2$O$_2$ (35%) to remove carbon contamination and to etch away the first mono-layers of SiO$_2$. The mixture solution was stirred for 10 minutes, after which the wafers were submerged in hot water (80 °C) for 30 minutes in order to fully hydrolyze the SiO$_2$ surface. Subsequently, the wafer is then dried at 110 °C in the hot air to remove the physically adsorbed water. While hot, the wafers were transferred to a glovebox.

For transmission electron microscopy (TEM) studies, custom-made TEM wafers of typical size of 20 x 20 mm$^2$were used. These wafers consist of 36 individual TEM grids that are arranged into a square pattern and stabilized by a silicon frame. The central part of each TEM grid is etched away to create a 15 – 20 nm thick silicon nitride (SiN$_x$) 'membrane' window (typical dimensions of 100 x 100 μm$^2$) through which the electron beam can pass, enabling imaging of the supported particles on a sub-nanometer length scale. After calcination at 750 °C for 24 hours in dry air silicon nitride forms a 3 nm thick surface layer of silicon oxide. Subsequently, the wafer is then transferred to the glovebox. The schematic representation of the TEM grid is shown in Figure 2.1.

For attenuated total internal reflection – Fourier transform infrared spectroscopy (ATR-FTIR) studies, internal reflection crystals (trapezoid shaped, 45° angle) made of silicon (Si) and zinc selenide (ZnSe) crystals were used. These ATR crystals were dried at 110 °C in the hot air and transferred to the glovebox.
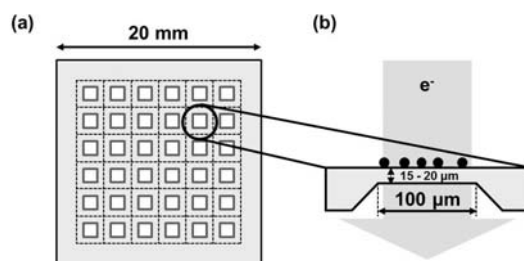
**Figure 2.1.** *(a) Schematic representation of custom made TEM wafer, consisting of 36 fused TEM grids with windows. (b) Cross sectional view of the individual TEM grid with the electron transparent membrane suspended in silicon frame.*

## 2.2 Spin coating technique

Every preparation of a Ziegler-Natta catalyst on the flat model surface starts from the deposition of $MgCl_2$ (with or without donor incorporated) in ethanol solution onto Si wafers/TEM grids/ZnSe or Si ATR crystals by means of the spin coating technique. 'Spin to coat' can be the most simplified elaboration to the process of spincoating. Spin coating is a technique which is used to coat or create films with organic, inorganic or polymeric materials from solutions by evaporating the solvent with high speed spinning. In other words, it is a technique for the desorption of soluble material on planar supports by wet 'impregnation', which is analogous to that of industrial impregnation procedures (Figure 2.2).[5-10]

Generally a spin coating device can be schematically depicted as indicated in Figure 2.2b (left).[2,5] A substrate, for example a silica/silicon wafer, is attached to a chuck. The wafer is covered with the solution and spun at a desired speed. Spinning velocity, acceleration and spinning time are changeable parameters directly linked to the equipment. Figure 2.2b (middle) shows how the film is formed upon spinning. As the solution is ejected from the substrate by radial flow, a uniform film of, for example, $MgCl_2$ in ethanol is formed due to centrifugal forces. Upon spinning, the deposited layer becomes thinner, and the shear viscosity forces slow down the outer movement of the liquid. At a definitive moment ejection and the evaporation of liquid contribute equally in the layer thinning process.[1,2] Moreover, a uniform film thickness can also be achieved.
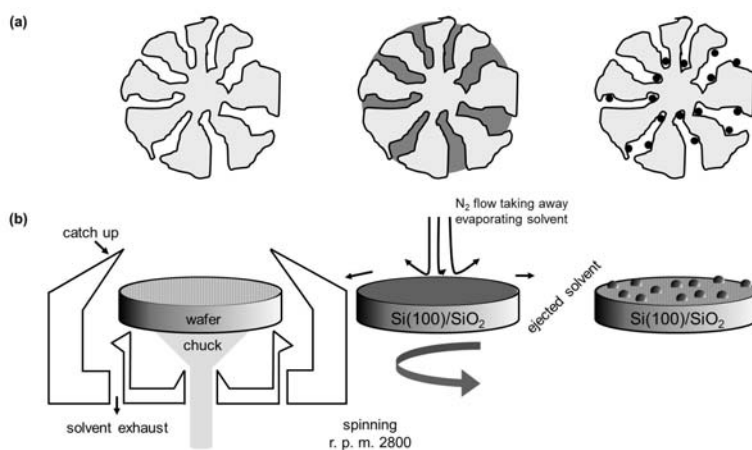
**Figure 2.2.** *The analogy between (a) pore volume impregnation of porous support, and (b) spincoating impregnation of a flat model support.[5] (b left) Schematic representation of a spin coat device; the sample is mounted on a chuck by means of vacuum and spun at a desired spinning speed between 1000 and 6000 r. p. m. The excess solvent is collected on the side.[2] (b middle) Evaporation of the solvent and radial liquid flow due to the centrifugal forces of the solvent determine the amount of the solute which precipitates on the wafer.[1]*

From that moment, the evaporation time becomes the prevailing parameter until, after a certain time $t_e$, the solvent is entirely evaporated. The evaporation time $t_e$, the spinning speed $\omega$ and the concentration of the precursor in the impregnating solution ($C_0$) determine the amount of deposited material $M$.[11-13] The evaporation time can be determined by monitoring the disappearance of the interference pattern (Newton's rings), which become noticeable when the solution layer is satisfactorily thin. The loading of the solute can be controlled by varying the concentration in the impregnating solution and is determined using the following Equation (2.1).[11-13]

$$M = 1.35C_0\sqrt{\eta/t_e\rho\omega^2} \qquad (2.1)$$

where $\eta$ and $\rho$ are the viscosity and density of the impregnating solution, respectively. This equation has been verified formerly for the flat $Co/Pt/SiO_2/Si(100)$ bimetallic model catalysts prepared from $Co(NO_3)_2.6H_2O$ and $Pt(NH_3)_4(NO_3)_2$ precursors[14] and a flat $Cr/SiO_2/Si(100)$ model catalyst[1,2] prepared

from $CrO_3$. In general, this equation holds as long as there is no strong chemical interaction between the solute and substrate.[15]

In this particular case, under a dry nitrogen atmosphere (under glovebox conditions), the Si wafers/TEM grids/ZnSe or Si ATR crystals is spins at 2800 rotations per minute (r. p. m) with a solution of $MgCl_2$ in ethanol or $MgCl_2$/electron donor in ethanol for various studies. The solution is ejected from the wafer, leaving behind a thin film of $MgCl_2.n$EtOH or $MgCl_2$(donor).$n$EtOH. Figure 2.3 shows the spin coating device and different samples for XPS, TEM and ATR-FTIR studies.
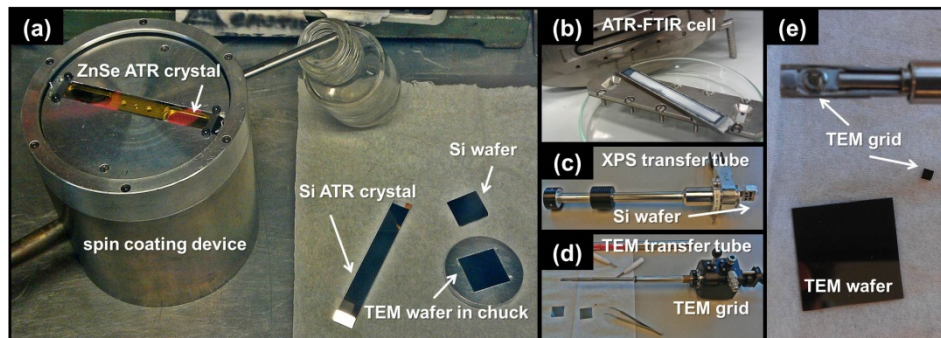


**Figure 2.3.** *(a) A spin coat device located inside the glovebox; ATR crystals, Si wafer and TEM wafer are also shown in the figure. (b) Picture of ATR-FTIR cell. (c) Picture of XPS transfer tube; Si wafers on the sample holder. (d) Picture of TEM transfer tube. (e) Close view of the TEM grid holder in the TEM transfer tube.*

## 2.3 Working operations

Briefly, Ziegler-Natta catalysts are air sensitive systems. Anhydrous $MgCl_2$ can very easily absorb water due to its hygroscopic properties. $TiCl_4$ and cocatalyst ($AlEt_3$) react rapidly and violently with water. Therefore, the delicacy of this catalytic system demands working operations to be carried out under anhydrous and anaerobic conditions in a glove box ($O_2$ < 1 ppm and $H_2O$ < 0.2 ppm). Each preparation step starting from spin coating in the glovebox.

The spin coated ATR crystal is inserted into the ATR cell and sealed. The ATR cell was then transferred from glovebox to ATR-FTIR spectrometer.

The spin coated XPS wafers were attached to the sample holder of the XPS transfer unit. The sealed XPS transfer unit was then transferred from glovebox to an X-ray photoelectron spectrometer.

The spin coated TEM wafer was carefully broken into individual TEM grids. A single TEM grid was mounted on the sample holder of the TEM transfer tube. The TEM transfer tube was then sealed and transferred from glovebox to transmission electron microscope.

## 2.4 Attenuated total reflection – Fourier transform infrared (ATR-FTIR) spectroscopy

Infrared spectroscopy is one of the oldest characterization techniques used in catalysis.[16] Infrared spectroscopy (IR) is a technique based on the vibrations of the atoms of a molecule. An infrared spectrum is commonly obtained by passing infrared radiation through a sample and determining what fraction of the incident radiation is adsorbed at a particular energy. Fourier-transform infrared (FTIR) spectroscopy is based on the idea of the interference of radiation between two beams to yield an interferogram. The latter is a signal produced as a function of the change of pathlength between the two beams. The two domains of distance and frequency are interconvertible by the mathematical method of Fourier-transformation.[17]

Attenuated total reflectance (ATR) spectroscopy utilizes the phenomenon of total internal reflection (Figure 2.4).[18] The concept of internal reflection spectroscopy or ATR originates from the fact that radiation propagating in an optically dense medium of refractive index $n_1$ undergoes total internal reflection at an interface of an adjacent medium of lower optical density (refractive index $n_2 < n_1$).[19,20] This wave is termed evanescent and is decays exponentially in accordance with Equation (2.2),[20] which permit this technique to probe only the first micrometres in the rarer medium. The evanescent beam loses energy at the wavelength where the material absorbs. The resultant attenuated radiation is measured and plotted as a function of wavelength by the spectrometer and gives rise to the absorption spectral characteristics of the sample.
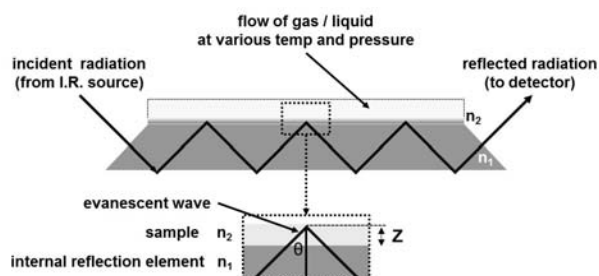
**Figure 2.4.** *The principle of ATR-FTIR. An IR-beam is directed on the internal reflection element (refractive index $n_1$) above the critical angle ($\theta$) to obtain total internal reflection and the evanescent wave penetrated in the rarer medium (refractive index $n_2$). The absorption in the rarer medium (sample) is detected after the beam departs the internal reflection element.*

$$E = E_0 e^{[-2\pi/\lambda_1(sin^2\theta - n_{21}^2)^{1/2}Z]} = E_0\, e^{(-\gamma Z)} \qquad (2.2)$$

where

$$n_{21} = n_2/n_1$$

$n_1$        is the refractive index of the less dense medium.

$n_2$        is the refractive index of the denser medium.

$$\lambda_1 = \lambda/n_1$$

$\lambda_1$        is the wavelength in the denser medium

$\lambda$        is the wavelength in free space

$\theta$        is the angle of incidence with respect to the normal

$Z$        is the distance from the surface as indicated in Figure 2.4

To obtain total reflection, the angle of incident radiation must be exceed the critical angle ($\theta \geq \theta_C$); according to Equation (2.3).

$$\theta_C = sin^{-1}\frac{n_2}{n_1} \qquad (2.3)$$

Even though total reflection takes place at the interface when $\theta \geq \theta_C$, the electromagnetic field penetrates beyond the reflecting surface into the less dense

medium, but only by a fraction of its wavelength. The depth of penetration is expressed as in Equation (2.4).[20]

$$d_p = \frac{\lambda_1}{2\pi}(sin^2\theta - n_{21}^2)^{-1/2} \qquad (2.4)$$

An ATR-FTIR set up comprises an internal reflection element to which the indirect IR-beam is directed in the critical or higher angle. Different designs of ATR cells allow both liquid and solid samples to be examined. The sample is pressed onto the internal reflection element and the evanescent wave comes into the sample. It is also possible to set up a flow-through ATR cell by including an inlet and an outlet in the apparatus. This allows for the continuous flow of solutions through the cell and permits spectral changes to be monitored with time i.e., *in-situ*. Compared to single reflection of IR radiation through ATR prism, multiple internal reflections of IR radiation through the specially shaped crystal produce more intense spectra. The penetration depth ($d_p$) decreases as a function of decreasing wavelength, and hence it is normal to correct the ATR-FTIR spectra if they are compared with normal IR-spectra.[20] The penetration depth is typically about 1μm.[21]In the case of polyethylene film grown on ZnSe crystal the calculated depth of penetration is 2 μm.[3] Hence, in PE films thicker than about 2 μm. Only the first 2 μm contribute to the ATR signal. The lowest measurable IR signal wavenumber (cut-off) is 1500 cm$^{-1}$ for Si crystal and 520 cm$^{-1}$ for ZnSe crystal.

For the study of the flat model for ethylene or propylene polymerization catalyst, an ATR-FTIR flow cell set up has been constructed (Figure 2.5). This set up includes solution containers, a pre reactor and an ATR flow cell, all of which can be connected to gas supplies with a pressure up to 10 bars and a vacuum system. A solution [e.g. Al(C$_2$H$_5$)$_3$ in anhydrous benzene] can be introduced to the pre-reactor, where the solution will be saturated with ethylene or propylene at a desired pressure. The ethylene or propylene saturated solution is introduced into the ATR cell under the ethylene or propylene in a flow mode with the speed controlled by a flow meter. Both the pre-reactor and the ATR cell can be set to a desired temperature up to 250 °C. In the meantime as polymer grows on the ZnSe crystal, infrared spectra are recorded to monitor the polymerization.
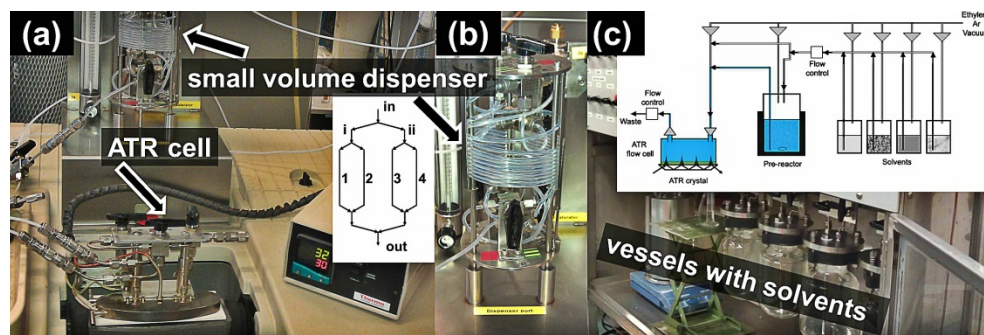
41

**Figure 2.5.** *(a) Picture of ATR-FTIR spectrometer set-up. (a inset) Schematic diagram of small volume dispenser. (b) Picture of small volume dispenser set-up. (c) Ethylene and propylene polymerization set-up. (c inset) Schematic set-up representation of ATR-FTIR.*

A small volume dispenser was developed to introduce hydrocarbon solutions of electron donor into ATR cell. In the glovebox, small volumes of electron donor/heptane solutions were loaded in the dispenser. The dispenser is small enough to fit in the small antechamber of the glovebox, which enables fast transfer from glovebox to ATR setup. The dispenser was then inserted into the ATR set up.

In conclusion, the advantages of the *in-situ* ATR-FTIR are (i) the ability to provide information at the molecular level, (ii) the high sensitivity towards extremely diluted surface species, (iii) the high versatility, which implies the possibility to perform measurements *in-situ* in the presence of reagents or probe molecules, at different temperatures and different pressures.

All FTIR spectra were collected using a Nicolet Protégé 460 Fourier transform infrared spectrometer equipped with a liquid $N_2$ cooled MCT detector. Spin coated Si or ZnSe crystals were sealed in a heated attenuated total reflectance (HATR) flow cell from Spectra-tech ARK. We have used *in-situ* ATR-FTIR to follow interactions of electron donors with $MgCl_2$, $TiCl_4$ and $AlEt_3$; which is described in **Chapter 3**, **4**, **5** and **6**.

## 2.5 X-Ray photoelectron spectroscopy (XPS)

X-ray photoelectron spectroscopy (XPS) is a surface science technique based upon the photoelectric effect which was discovered by Thomson[22] and later

explained by Einstein.[23] When an X-ray beam is directed onto a sample surface, energy of the X-ray photon is adsorbed by the core electron of an atom. If the photon energy, *hv*, is large enough, the core electron will then escape from the atom and emit out of the surface. The emitted electron with the kinetic energy of $E_k$ is referred to as the photoelectron. The kinetic energy of the emitted electron depends on the wavelength of radiation in accordance with the following Equation (2.5).[24,25]

$$E_k = hv - E_b - \varphi \qquad (2.5)$$

where

$E_k$         is the kinetic energy of the electron.

$h$         is Plank's constant.

$v$         is the frequency of the absorbed radiation.

$E_b$         is the binding energy of the photoelectron w. r. t. the Fermi level of the sample.

$\varphi$         is the work function of the spectrometer.

Equation (2.5) can be used to calculate the binding energy $E_b$, if the frequency $v$ of the X-ray photons and the kinetic energy $E_k$ of the photoelectrons are known. As XPS set-ups are equipped with X-ray sources of known wavelengths – Al Kα (1486.6 eV) and/or Mg Kα (1253.6 eV) – binding energies can be plotted against the amount of counts per energy step and labelled according to the quantum numbers of the level from which electron originates.

The principle is schematized in Figure 2.6. As the sample is irradiated, an atom absorbs a photon of energy (*hv*) and an electron, a photoelectron to be specific, is emitted. At around the same time, but at a slower rate, an additional phenomenon occurs. The core hole created by the electron is filled with an electron from a higher shell whereas the atom relaxes from the excited state. The energy released from this step is taken up by another electron, the Auger electron, which is emitted, again with an element specific kinetic energy. Auger electrons have fixed kinetic energies.[24-27]

The photoelectron can travel a very limited distance in the substance, which makes the XPS very surface sensitive. The inelastic mean free path of the photoelectrons in solids is less than 1 – 2 nm for the kinetic energies within 15 – 1000 eV,[27] and generally the information depth of the XPS is limited to approximately three times the inelastic mean free path.[24] Hence, XPS evidently entails ultra-high vacuum (UHV) operating conditions with a pressure if possible less than $10^{-9}$ mbar.
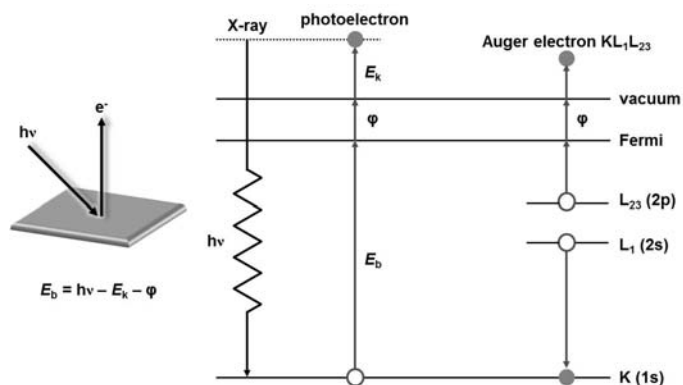


**Figure 2.6.** *The photoelectric effect forms the principle behind XPS. Atoms are excited with X-rays (hv), a photoelectron is emitted with the kinetic energy ($E_k$) equal to hv minus the binding energy ($E_b$) and the work function ($\varphi$). The empty core created by the photoelectron is filled by an electron from a higher energy level ($L_1 \rightarrow K$), and the relaxation energy emits an Auger electron ($L_{23} \rightarrow Auger$).*[24]

Overall, the important consequence of the small inelastic mean free path is that the XPS intensity for atoms located at the surface is significantly higher than for atoms underneath the surface. Atoms which are located more than a few nanometers below the surface barely contribute to the XPS signal. Binding energies are influenced by oxidation states of atoms; therefore XPS can also be used to identify these states and quantify them. Another important feature in XPS is that by changing the take-off angle (an easy procedure in the XPS set up), the surface sensitivity changes: the greater the take-off angle of photoelectrons between its direction and the surface normal of the sample, the greater the surface sensitivity of

photoelectrons.[24] Angle dependency of the XPS can be used to make a coarse assessment of the vertical distribution of materials in the sample.

In conclusion, XPS can offer semi-quantitative information about (i) the elements present on the surface, (ii) relative amounts of elements on the surface (iii) chemical states of those elements on the surface.

For our studies, we used VG Escalab 200 and Kratos AXIS Ultra spectrometers, equipped with a monochromatic Al Kα source and a delay-line detector (DLD). Spectra were obtained using this aluminium anode (Al Kα = 1486.6 eV) operating at 150 W and spectra were recorded with a background pressure in the analysis chamber of $1 \times 10^{-9}$ mbar. Measurements were carried out at a 0° and 60° take-off angle relative to the surface normal. Binding energies were calibrated with the standard Si 2p = 103.3 eV or Cl 2s = 199.5 eV.

XPS is used to characterize samples of $MgCl_2$ (with or without donor), $MgCl_2/TiCl_4$ and complete Ziegler-Natta catalyst system; which is described in **Chapter 3** and **6**.

## 2.6 Transmission electron microscopy

Electron microscopy is a common technique to investigate nano-scale structures. The principle of electron microscopy is comparable with that of a light microscope with the differences of a light source being replaced by an electron beam source and the optic lenses by electro-magnetic ones. Electrons in the electron beam have a typical wavelength of λ = 5 – 10 pm, small enough to image nanometer-sized structures but too small for wavelengths of visible light (λ = 400 – 800 nm).[24,25,28] Figure 2.7 shows the range of signals which are generated when the primary electron beam is pointed towards a sample. These response signals can be used for all kinds of characterization techniques.

Transmission electron microscopy (TEM) uses a focused primary electron beam to radiate the sample but in TEM electrons with a much higher kinetic energy are used (100-300 keV). These electrons have such a high kinetic energy that samples thinner than 50 nm become partly electron transparent and the so-called transmission electrons will travel through the sample generating a shadow-image. This shadow-image gives detailed information about the internal structure of the

materials (crystal lattices, stacking faults, etc.) and can reach nanometer resolution under the right conditions.[24,28] The most common method to get electron transparent samples in thin film research is cutting out a cross-section of the material using a focused ion beam.[28] However, since this method is labour-intensive, we used in-house grids (more details about the TEM grids can be seen in **Section 2.1**).
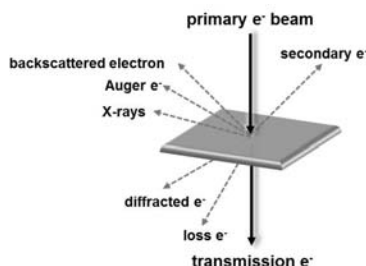


**Figure 2.7.** *The signals generated by an electron beam in electron microscopy. In the case of transmission electron microscopy, transmission electron signals are used.*

The analysis of samples was carried out on a FEI Tecnai G$^2$ Sphera microscope operating with a 200 kV LaB$_6$ filament and a bottom mounted 1024 x 1024 Gatan CCD camera. All images were measured using the TEM in the bright field mode. Electron diffraction patterns of species also can be obtained which can be used to determine the crystalline phases present in the samples. The application of TEM to MgCl$_2$ and MgCl$_2$/donor films will be extensively discussed in **Chapter 4**.

## 2.7 References

(1)  Thüne, P. C., *A Surface Science Model for the Phillips Ethylene Polymerization Catalyst;* Ph. D Thesis., Eindhoven University of Technology: The Netherlands, **2000.**

(2)  van Kimmenade, E. M. E., *Ethylene Polymerization over Flat Phillips Model Catalysts;* Ph. D Thesis., Eindhoven University of Technology: The Netherlands, **2006.**

(3)  Han, W., *Supported Homogenous Catalysts on Flat Model Surfaces for Ethylene Polymerization;* Ph. D Thesis., Eindhoven University of Technology: The Netherlands, **2007.**

(4)  Andoni, A., *A Flat Model Approach to Ziegler-Natta Olefin Polymerization Catalysts;* Ph. D Thesis., Eindhoven University of Technology: The Netherlands, **2009.**

(5)     Gunter, P. L. J.; Niemantsverdriet, J. W. (Hans).; Ribeiro, F. H.; Somorjai, G. A. *Catal. Rev. Sci. Eng.* **1997,** *39,* 77.

(6)     Thüne, P. C.; Verhagen, C. P. J.; van den Boer, M. J.; Niemantsverdriet, J. W. (Hans). *J. Phys. Chem B* **1997,** *101*, 8559.

(7)     Kishan, G.; Coulier, L.; de Beer, V. H. J.; van Veen, J. A. R.; Niemantsverdriet, J. W. (Hans). *J. Catal.* **2000,** *196,* 180.

(8)     Coulier, L.; de Beer, V. H. J.; van Veen, J. A. R.; Niemantsverdriet, J. W. (Hans). *Top. Catal.* **2000,** *13,* 99.

(9)     Coulier, L.; de Beer, V. H. J.; van Veen, J. A. R.; Niemantsverdriet, J. W. (Hans). *J. Catal.* **2001,** *197,* 26.

(10)    Kishan, G.; Coulier, L.; de Beer, V. H. J.; van Veen, J. A. R.; Niemantsverdriet, J. W. (Hans). *J. Catal.* **2001,** *200,* 194.

(11)    Kuipers, E. W.; Laszlo, W.; Wieldraaijer, W. *Catal. Lett.* **1993,** *17,* 71.

(12)    Kuipers, E. W.; Doornkamp, C.; Wieldraaijer, W.; van den Berg, R. E. *Chem. Mat.* **1993,** *5,* 1367.

(13)    van Hardeveld, M.; Gunter, P. L. J.; van IJzendoorn, L. J.; Wieldraaijer, W.; Kuipers, E. W.; Niemantsverdriet, J. W. (Hans). *Appl. Surf. Sci.* **1995,** *84,* 339.

(14)    Borgna, A.; Anderson, B. G.; Saib. A. M.; Bluhm, H.; Havecker, M.; Knop-Gericke, A.; Kuiper, A. E. T.; Tamminga, Y.; Niemantsverdriet, J. W. (Hans). *J. Phys. Chem.* **2004,** *108,* 17905.

(15)    Saib, A. M., *Towards a cobalt Fischer-Tropsch Synthesis Catalyst with Enhanced stability: A Combined Approach;* Ph. D Thesis., Eindhoven University of Technology: The Netherlands, **2006.**

(16)    Eischens, R. P.; Pliskin,, W. A.; Francis, S. A. *J. Chem. Phys.* **1954,** *22,* 1786.

(17)    Griffiths, P. R.; de Haseth, J. A., *Fourier Transform Infrared Spectroscopy;* Wiley: New York, **1986.**

(18)    Harrick, N. J.; du Pre, F. K. *Appl. Optics* **1966,** *5,* 1739.

(19)    Urban, M. W., *Attenuated Total Reflectance Spectroscopy of Polymers;* American Chemical Society: Washington DC, **1996.**

(20)    Mirabella, F. M., *Internal Reflexion Spectroscopy;* Dekker: New York, **1993.**

(21)    Knotturi, E., *Surface Chemistry of cellulose from Natural Fibers to Model Surfaces;* Ph. D Thesis., Eindhoven University of Technology: The Netherlands, **2005.**

(22)    Thomson, J. J. *Philos. Mag. Ser. 5:* **1899,** *48,* 547.

(23)    Einstein, A. *Ann. Phys.* **1905,** *17,* 132.

(24)    Niemantsverdriet, J. W. (Hans)., *Spectroscopy in Catalysis;* Wiley-VCH: Weinheim, **2007.**

(25)    Watts, J. F.; Wolstenholme, J., *An Introduction to Surface Analysis by XPS and AES;* Wiley-VCH: **2003.**

(26)    Briggs, D.; Seah, M. P., *Practical Surface Analysis;* John Wiley & Sons: Chichester, **1983.**

(27)    Hüfner, S., *Photoelectron Spectroscopy – Principles and Applications;* Springer: Berlin, **1996.**

(28)    Egerton, R. F., *Physical Principles of Electron Microscopy; an Introduction to TEM, SEM and AEM;* Springer-Verslag: **2005.**

# 3

# Quantification and calibration of

# ATR-FTIR signals

# **Abstract**

*To study the surface structure of $MgCl_2$ support and its interaction with other active components in Ziegler-Natta catalyst, such as electron donors, we prepared a thin film analogue for Ziegler–Natta ethylene polymerization catalyst support by spin coating a solution of $MgCl_2$ in ethanol, optionally containing a diester internal donor (diisobutyl-ortho-phthalate – DIBP) on a flat Si crystal surface. The donor content of these films was quantified by applying attenuated total internal reflection – Fourier transform infrared spectroscopy (ATR-FTIR) and X-ray photoelectron spectroscopy (XPS). Changes in the interaction of DIBP with $MgCl_2$ at various temperatures were monitored by in-situ ATR-FTIR. Upon increasing the temperature, a shift in the $v(C=O)$ band towards lower wavenumbers was observed together with the depletion of $v(O-H)$ stretching band due to the desorption of residual ethanol. We assign this shift to gradual redistribution of adsorbed DIBP from the less acidic adsorption sites on the $MgCl_2$ (104) surface towards the more acidic $MgCl_2$ (110) surface.*

# 3.1 Introduction

Infrared spectroscopy has long been a useful tool for studying the chemical structure of heterogeneous catalysts. It is particularly attractive in the field of Ziegler-Natta catalysts for olefin polymerization, where organic complexes are formed within the catalyst matrix.[1] With regard to the propylene polymerization catalysts, most of the work has focused on the spectral changes in the IR features of internal donors (used as promoters) in various stages of catalyst preparation.[2-20] It is generally believed that an internal donor binds to lateral terminations of the $MgCl_2$ support – such as (104) and (110) – and thereby provide stability to those surfaces.[17] Internal donors also provide stereoregulartity to the nearby bound titanium species along the same surface.[13,18] Diisobutyl phthalate (DIBP) ester is widely used as an internal donor in industrial Ziegler-Natta catalysts due to its ability to control the amount and distribution of $TiCl_4$ over the $MgCl_2$ support.[21] The $\nu$(C=O) band of ester and diester donors is intense and very sensitive to the coordination with a Lewis acid (in this particular case, the surface sites on $MgCl_2$ crystals). The IR spectrum of the solid $DIBP/MgCl_2/TiCl_4$ catalyst is in the 1900 – 1550 $cm^{-1}$ spectral range, contains a complex envelope of $\nu$(C=O) bands at 1687 $cm^{-1}$ (shifted from the 1729 $cm^{-1}$ of free DIBP), as well as two narrow bands of the *ortho*-disubstituted benzene ring of DIBP at 1595 and 1582$cm^{-1}$ (aromatic ring modes). The envelope of the carbonyl group vibrations in the DIBP coordinated catalyst IR spectra can be explained as the combination of the IR bands from different DIBP complexes.[11-13] The $\nu$(C=O) bands are assigned to complexes of DIBP with $MgCl_2$ and $TiCl_4$, as well as complexes of $MgCl_2$ with two derivatives of DIBP (these derivatives are formed due to the reaction between $TiCl_4$ and DIBP).[13-20] Fourier Transform Infrared (FTIR)has been an important qualitative tool for studying infrared observable adsorbates,[22-26] and under certain circumstances, can be used to determine surface concentration.[27-28] The integrated Beer-Lambert relation, *a = Alc*, is often used to relate surface concentration to IR peak areas, where *a* is IR absorbance peak area, *l* is the sample thickness, and *c* is the surface concentration. *A* is the integrated absorption intensity which can also be thought of as an extinction coefficient.[29-31] Knowledge of such extinction coefficients allows the quantitative determination of the concentrations of surface

adsorbed species using FTIR. When using the attenuated total internal reflection (ATR) technique, infrared radiation penetrates only a few micrometers into the bulk of a material, making it an excellent tool for surface studies of thin films.[32-36] For thin films (thickness less than 200 nm), the measured integrated absorbance can be approximated to the scale linear with the concentration of the deposited material.[37]

So far, XPS has been used to study the effect of the internal donor in flat-model Ziegler-Natta catalysts, by following the influence of the internal donor on the electron density around titanium.[38-43] This is an indirect method. In a direct XPS analysis of organic adsorbents (here, electron donors), shifts in the C 1s signal could be interpreted qualitatively, but poor deconvolution of spectra makes quantitative analysis unreliable.[44,45] This prompts the use of fluorine as an excellent analytical marker or doping agent for XPS, as fluorine exhibits a clear quantifiable peak around 692 eV.[29,46-49] It should be noted that XPS data are influenced by surface topology, lateral heterogeneity and depth from the sample surface. So, angle resolved XPS analysis is essential for accurate quantification.[50]

However, the complex nature of real catalysts prevents the acquisition of the atomic level knowledge about the active centers for polymerization and their local geometry. The active centers are hidden in the pore structure of the support, thereby limiting the exposed surface area for characterization. One solution to this problem is the development of model catalysts. The flat-model approach facilitates the characterization of the catalyst by surface spectroscopy and microscopy techniques.[39,51] *In-situ* ATR-FTIR is a good analytical tool to study the surface chemistry of flat-model catalyst system.[52] In the case of Ziegler-Natta catalysts, it is possible to observe the changes in the infrared features of internal donors during thermal and chemical treatments on $MgCl_2$.

In this chapter, we focus on the *in-situ* ATR-FTIR analysis of $MgCl_2$/Ethanol/DIBP films on a flat surface. The $\nu(C=O)$ band of the $MgCl_2$/DIBP films producing an asymmetric envelope between 1710 and 1692 $cm^{-1}$ is the prime interest for this study. Since the $TiCl_4$ is not present in this film, the existence of donor-$TiCl_4$, donor derivative-$MgCl_2$ complexes can be excluded. The DIBP content of the films was quantified by combining ATR-FTIR and XPS data. An

approximate estimation of residual ethanol in these films was done by XPS measurements. Changes in the $\nu$(C=O) band of the DIBP/MgCl$_2$ films upon heating in a flowing argon gas stream were monitored *in-situ*. Using the IR signatures of DIBP-MgCl$_2$ complexes reported in literature, we made an attempt to reveal the changes in the adsorption mode of DIBP on MgCl$_2$ surface with respect to temperature.

## 3.2 Experimental

### 3.2.1 Materials

Anhydrous magnesium chloride (ball milled, 99.9%), 4-fluorophthalic anhydride (97%), isobutanol (99%), anhydrous calcium chloride, concentrated sulphuric acid (96.7%), dichloromethane, sodium bicarbonate, sodium chloride and sodium sulphate were purchased from Aldrich Chemicals and used as received. Absolute ethanol (99.9%) and diisobutylphthalate (97%)were purchased from Merck Chemicals and used as received. Argon (grade 6.0) was purchased from Linde and used after passing through a Dririte®/molecular sieve column (4 Å).

### 3.2.2 Synthesis of 4-Fluoro-diisobutyl phthalate

4-Fluoro-diisobutyl phthalate (FDIBP) was synthesized adapted from a procedure found in literature.[53] FDIBP was obtained by the full esterification of 4-fluorophthalic anhydride with isobutanol (Scheme 3.1).
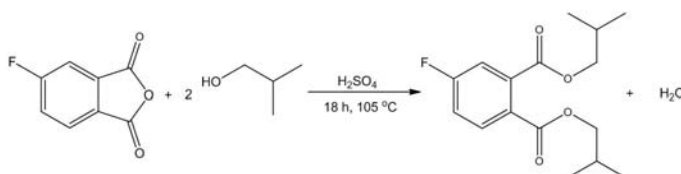


**Scheme 3.1.** *Full esterification of 4-fluorophthalic anhydride with isobutanol.*

4-Fluorophthalic anhydride (2 g, 12 mmol) was added to dry isobutanol (25 cm$^3$) in a round-bottomed flask equipped with an Ar-inlet and a reflux condenser fitted with a CaCl$_2$-drying tube. Concentrated sulphuric acid (96.7 %, 30 mg, 15 µL, 0.015 mol dm$^{-3}$) was carefully added with stirring. Upon bubbling Ar through the mixture, it was stirred for 18 h at 105 °C after which it was concentrated to *ca.*

10 cm$^3$ and transferred to a separating funnel using 40 cm$^3$ dichloromethane. The organic layer was washed with 50 cm$^3$ cold water, cold 0.6 M NaHCO$_3$ solution and a cold saturated NaCl solution. After drying the organic layer with Na$_2$SO$_4$, the solvent was evaporated to afford 4-fluoro-diisobutyl phthalate as a colourless oil (3.185g, 10.8 mmol, 89.6%). Obtained 4-fluoro diisobutylphthalate (FDIBP) was characterized by $^1$HNMR (Figure 3.1).
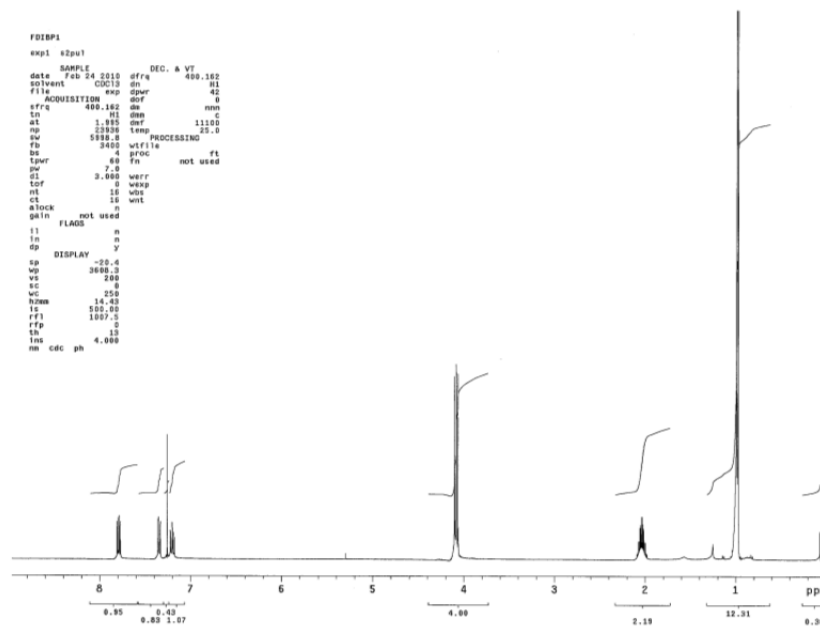


**Figure 3.1.** *$^1$HNMR spectra of 4-fluoro-diisobutyl phthalate [$\delta_H$ (CDCl$_3$)7.80 (1-H, m, Ar-H), 7.38 (1-H, m, Ar-H), 7.21 (1-H, m, Ar-H), 4.08 (4-H, t, -O-C$\underline{H}_2$-), 2.02 (2-H, m, -C$\underline{H}$(CH$_3$)$_2$), 1.01 (12-H, d, -CH(C$\underline{H}_3$)$_2$)].*

### 3.2.3 Preparation of MgCl$_2$/donor thin films

From a bulk solution of MgCl$_2$ (105 mmol dm$^{-3}$) in ethanol, a series of solutions with donor/MgCl$_2$ molar ratios of 0.05, 0.10, 0.15, 0.20, 0.25 and 0.50 was prepared. Donor free MgCl$_2$ films also were prepared. All these preparations were carried out in N$_2$ atmosphere. In a typical procedure, a solution was spincoated (2800 r.p.m.) under glovebox conditions onto Si crystal (for ATR-FTIR studies), Si wafer (for XPS studies).

### 3.2.4 Analytical techniques

All FTIR spectra were collected using a Nicolet Protégé 460 Fourier transform infrared spectrometer equipped with a heated HATR flow cell for Spectra-Tech ARK with a Si 45° crystal (cut-off at 1500 cm$^{-1}$). The FTIR spectra of uncoordinated DIBP and FDIBP were recorded using Nicolet Smart Golden Gate equipment with a diamond crystal (cut-off at 800 cm$^{-1}$). The coated Si crystal was mounted and sealed under a nitrogen atmosphere in an ATR-cell. In order to mimic the high vacuum conditions during XPS measurement and simultaneously prevent moisture and oxygen from atmosphere entering into the system, Ar gas was flowed through the cell for 30 min at 2 bar and 30°C. FTIR spectra were measured in absorbance mode using a Silicon background (taken at 30 °C) with a resolution of 4 cm$^{-1}$ and 32 scans per measurement. For temperature programmed *in-situ* studies, the ATR set up was gradually heated under argon flow with isothermal steps (10 °C difference) from 30 °C up to 150 °C. FTIR spectra were recorded at the end of each isothermal step (5 min), against a Si background (taken at that particular temperature).

XPS measurements were performed with a VG Escalab 200 using a standard aluminium anode (Al Kα 1486.3 eV) operating at 300 W. The coated Si wafer was transferred (using the XPS transfer vessel) under nitrogen atmosphere into the XPS-antechamber and then under high vacuum conditions into the measurement chamber. Spectra were recorded at a background pressure of $1 \times 10^{-9}$ mbar. Binding energies were calibrated to a Cl 2s peak at 199.5 eV. Measurements were carried out at a 0° and 60° take-off angle relative to the surface normal.

## 3.3 Results and discussion

### 3.3.1 Quantification of residual ethanol in the spin coated MgCl$_2$ films

A solution of MgCl$_2$ in ethanol was spin coated on Silicon wafers under an inert atmosphere (in the glove-box). Then these wafers were heated at 30, 80, 150, 200 and 250 °C for one hour in the same atmosphere and cooled down to room temperature. We recorded the XPS spectrum of MgCl$_2$/ethanol film (on a silicon wafer) at room temperature. The elemental analysis (C, O, Mg, Cl and Si) was

55

carried out. The Mg/Cl ratio (1.00:2.10) in the non-annealed $MgCl_2$/EtOH films closely resembles that of anhydrous $MgCl_2$, indicating that $MgCl_2$ has deposited without any significant hydrolysis. This ratio remains almost same in the films annealed at 30, 80 and 150 °. However, the films which is annealed at 200 and 250 °C; the Cl to Mg ratio reduced from 2 to 0.7. This could be due to the formation of MgO; the final product of hydrolyzed $MgCl_2$ (occurs at high temperature in the presence of adsorbed moisture contaminant). Figure 3.2 shows the difference in the Cl and Mg signals from the $MgCl_2$/EtOH films annealed at 30 and 250 °C.
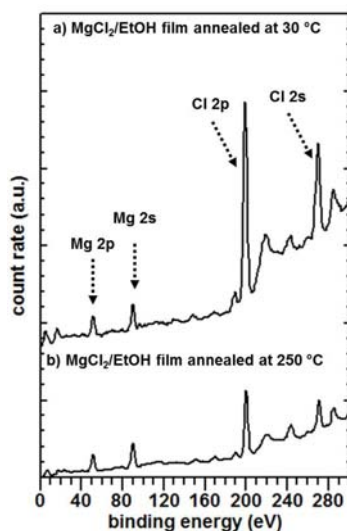


**Figure 3.2.** *Comparative XPS spectra of MgCl$_2$/EtOH film annealed at 30 °C (top) and MgCl$_2$/EtOH film annealed at 250 °C (bottom).*

Ethanol contributes to C1s signal of XPS spectra. However, C1s signal is largely overlapped with energy loss features of Cl 2s signal (Cl from $MgCl_2$). As a reference, we measured XPS spectrum of anhydrous $MgCl_2$. The anhydrous $MgCl_2$ film was used for the calibration of Cl 2s energy loss features. Based on this information, it is possible to resolve the C 1s region of the $MgCl_2$/ethanol film as Cl 2s energy loss and C 1s signal from ethanol. C 1s signal of ethanol contains two peaks (based on XPS database), the C 1s signal from $CH_3$- carbon (284.3 eV) and the C 1s signal from $-CH_2-OH$ carbon (285.8 eV).C 1s regions of anhydrous $MgCl_2$, $MgCl_2$/ethanol film at 30 °C, and 150 °C are shown in Figure 3.3.

The contribution of ethanol to C 1s signal in the films annealed at different temperature was estimated. The residual ethanol present in the $MgCl_2$/ethanol film annealed at 30 °C was around 13 mol% w.r.t. Mg. We use this amount to calibrate $\nu$(O-H) band in the ATR-FTIR spectra of $MgCl_2$/ethanol film measured at 30 °C (after exposing to Ar gas flow for 30 minutes). The ATR-FTIR spectra of the same is shown in Figure 3.5 (top).
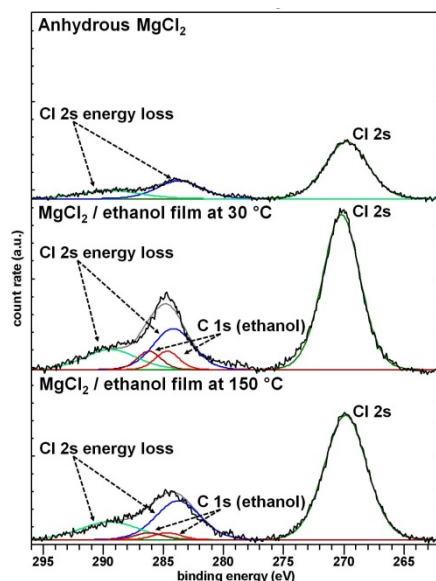


**Figure 3.3.** *Comparative XPS spectra (C1s region) of anhydrous $MgCl_2$ (top), $MgCl_2$/ethanol films after annealing at 30 °C (middle) and 150 °C (bottom).*

The $\nu$(O-H) band between 3500 to 3000 cm$^{-1}$ is from ethanol. However, water molecule also can give $\nu$(O-H) band between 3500 to 3000 cm$^{-1}$. It is important to make sure the spectra choose for calibration should be free from moisture. From the Figure 3.5 (top) it clear that at this stage the film is free of any adsorbed moisture. If moisture is present in the film, a band at 1630 cm$^{-1}$ (due to the scissoring of the two O-H bands) should appear. Thus we confirmed that the $\nu$(O-H) band appears in this particular spectrum is exclusively from ethanol. From XPS measurements we saw that residual ethanol bound to the film was decreased from 13 mol% to 3 mol% at 250 °C. However, the ATR-FTIR spectra recorded at very high temperature had signals from moisture too. So the actual concentration of

57

residual ethanol at high temperature might be even lower. The estimation of ethanol in the donor incorporated films were carried out by comparing the intensities of $v$(O-H) bands in those films with $v$(O-H) band of $MgCl_2$/ethanol film measured at 30 °C (after exposing to Ar gas flow for 30 minutes).

## 3.3.2 Quantification of coordinated donor

A series of $MgCl_2$-DIBP mixtures in ethanol with different DIBP to Mg molar ratio was prepared and spin coated onto the Si ATR crystal. FTIR spectra of these $MgCl_2$/DIBP films were recorded after 30 minutes of Ar flow at 30 °C. All spectra measured at 30 °C contained a $v$(C=O) band around 1700 cm$^{-1}$, which can be assigned to the $v$(C=O) band of coordinated DIBP. We observed a linear increase in peak intensity when increasing the DIBP to Mg ratio up to 0.25.

A fluorine tagged DIBP homologue (4-fluoro-diisobutyl phthalate or FDIBP) was synthesized for XPS studies. Comparison of uncoordinated DIBP and FDIBP IR spectra is given in Figure 3.4.
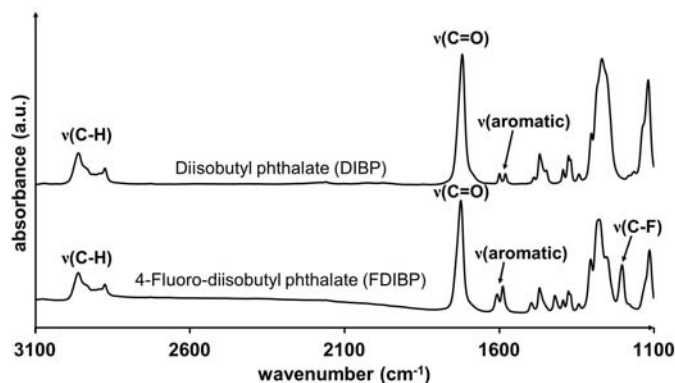


**Figure 3.4.** *Comparative IR spectra of diisobutyl phthalate (top) and 4-fluoro-diisobutyl phthalate (bottom).*

The peak positions of all relevant IR bands in Figure 3.4 are given in Table 3.1. The peaks marked **'$v$(C-H)'** represents alkyl group stretching bands of the donors. The peaks denoted as **'$v$(C=O)'** representing the respective carbonyl stretching bands of uncoordinated DIBP and FDIBP, are separated by only 3 cm$^{-1}$ (see Table 3.1), an indication that the fluorine atom of FDIBP has negligible influence on the stretching frequency of the C=O bonds when compared to DIBP.

As expected, the two aromatic ring mode peaks, marked **'ν(aromatic)'** (at *c.a.* 1600 and 1580 cm$^{-1}$ for both compounds), are symmetric for DIBP but asymmetric for FDIBP. The **'ν(C-F)'** band of FDIBP is clearly visible at 1203 cm$^{-1}$.

**Table 3.1.** *Comparative ATR-FTIR peak vibration frequencies for uncoordinated and coordinated 4-fluoro-diisobutyl phthalate (FDIBP) and diisobutyl phthalate (DIBP).*

| Donor | $\nu_{max}$ (C=O) (cm$^{-1}$) | $\nu_{max}$ (Aromatic ring modes) (cm$^{-1}$) |
|---|---|---|
| Uncoordinated DIBP | 1725 | 1599 & 1580 |
| Uncoordinated FDIBP | 1728 | 1608 & 1589 |
| Coordinated DIBP | 1705 | 1596 & 1581 |
| Coordinated FDIBP | 1708 | 1606 & 1590 |

The apparent similarity of the ν(C=O) bands is highly favoured when considering FDIBP as a tagged analogue for DIBP, since the C=O bond plays a vital role in coordinating with metal centers. In Figure 3.5, the ATR FTIR spectra of the spin coated MgCl$_2$/ethanol, MgCl$_2$/ethanol/DIBP and MgCl$_2$/ethanol/FDIBP films having donor to MgCl$_2$ ratios 0, 0.1 and 0.1 respectively, are compared.



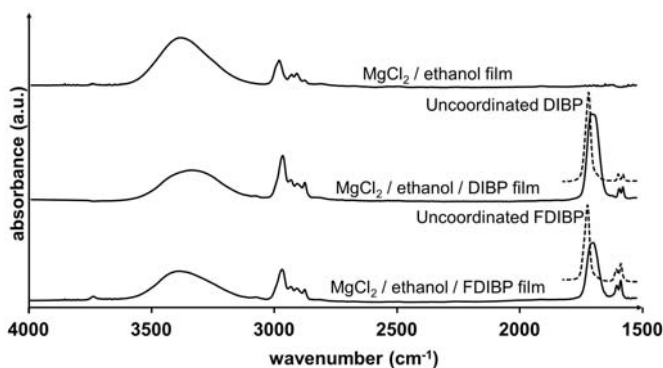**Figure 3.5.** *Comparative IR spectra of spin coated MgCl$_2$/Ethanol (top), MgCl$_2$/Ethanol/DIBP (middle) and MgCl$_2$/Ethanol/FDIBP (bottom) films, along with carbonyl stretching and aromatic ring modes of uncoordinated DIBP and FDIBP (dotted lines).*

> *Donor/MgCl$_2$ molar ratios are 0 (top), 0.1 (middle) and 0.1 (bottom) respectively.*

The carbonyl stretching modes and aromatic ring modes of uncoordinated DIBP and FDIBP are also shown (in dotted lines) for a comparison. The shift in peak maxima of carbonyl bands indicates the coordination of DIBP and FDIBP. The peak around 3400 cm$^{-1}$ corresponds to O-H stretching frequency of residual ethanol in the MgCl$_2$ film. The peak around 2950 cm$^{-1}$ corresponds to the C-C stretching frequency of alkyl groups in ethanol and donors.

Upon coordination, the $\nu_{max}$(C=O) (the carbonyl band peak maxima) shifts from 1725 to 1705 cm$^{-1}$ (DIBP) and 1728 to 1708 cm$^{-1}$ (FDIBP). The $\Delta\nu_{max}$ [difference between the $\nu_{max}$(C=O) of uncoordinated and coordinated donor] is 20 cm$^{-1}$ in both cases indicating that, the influence of F atom in the aromatic ring on the coordination behaviour of phthalate ester is negligible (see Table 3.1). This makes FDIBP an ideal substitute for DIBP in XPS studies. MgCl$_2$/FDIBP films were prepared by following the same preparation method used for MgCl$_2$/DIBP films. The same ATR-FTIR experimental procedure used for DIBP/MgCl$_2$ films was followed for FDIBP/MgCl$_2$ complexes too. ATR-FTIR spectra of MgCl$_2$/DIBP films and MgCl$_2$/FDIBP films with different donor loadings are shown in Figure 3.6a and 3.6b respectively.

The peak position of uncoordinated donors (in the liquid phase) is also given for comparison (dotted line). Using TQ Analyst Software, peak maxima (center of gravity peak location at 10% threshold) and integrated peak intensities for the carbonyl stretching band of DIBP and FDIBP was determined. Both DIBP and FDIBP show Beer-Lambert type behaviour when plotting the integrated intensity (absorbance mode) of the C=O stretching band and aromatic ring bands versus Donor to Mg ratio (shown in Figure 3.6a inset and 3.6b inset). This indicates that donor/MgCl$_2$ ratio in films reproduces the donor to MgCl$_2$ ratio in the spin coating solution.
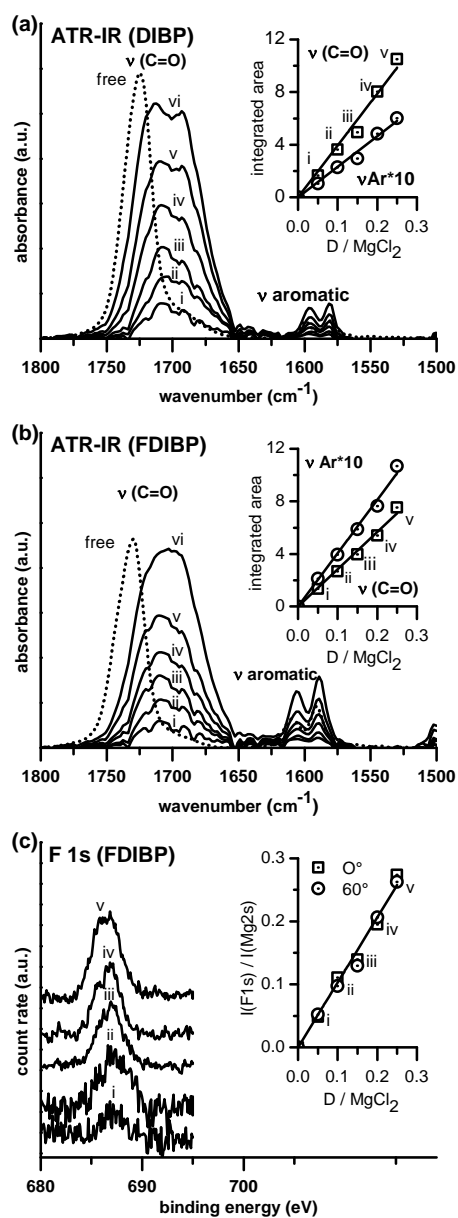
**Figure 3.6.** *(a) Carbonyl and aromatic IR bands of DIBP in MgCl₂/DIBP films. (a inset) Plot of the integrated peak intensities of the carbonyl band and the aromatic ring band (intensity multiplied by 10) versus the DIBP/Mg ratios in ethanol solution prior to spin coating. (b) Carbonyl and aromatic IR bands of FDIBP in*

*MgCl$_2$/FDIBP films. (b inset) Plot of the integrated peak intensities of the carbonyl band and the aromatic ring band (intensity multiplied by 10) versus the FDIBP/Mg ratios in ethanol solution prior to spin coating. (c) F 1s XPS spectra of the MgCl$_2$/ethanol/FDIBP films. (c inset) Plot of the F/Mg ratios measured by XPS (at a photo electron takeoff angle of 0° and 60°, relative to the surface normal) versus the F/Mg ratios in ethanol solution prior to spin coating.*

XPS is used to confirm the ATR-FTIR quantification of the donor concentration in the film. A fluorinated derivative of DIBP (FDIBP) was used as the internal donor in the films for XPS studies. Using XPS, the constituent atoms in the FDIBP/MgCl$_2$ films were quantified, and the lateral heterogeneity of the films was established. The combined XPS spectrum (F 1s region) of MgCl$_2$/Ethanol/FDIBP films, with donor/Mg molar ratios ranging from 0.05 to 0.25 is shown in Figure 3.6c. Angle resolved XPS experiments showed that the Mg to F ratio remained unchanged, irrespective of the photoelectron take-off angle 0° or 60° (relative to the surface normal). This is an indication of homogenous DIBP distribution throughout the MgCl$_2$ film. Figure 3.6c inset represents the plot of actual FDIBP to Mg ratio calculated using XPS versus initial FDIBP to Mg ratio in the spin coated solution. XPS proves the one-to-one correlation between concentration of donor in solution and film. Therefore, ATR-FTIR can be used for quantitative estimation of the donor in MgCl$_2$/donor films.

### 3.3.3 *In-situ* ATR-FTIR studies during annealing of the DIBP/MgCl$_2$ films under argon flow

The spectrum recorded before starting the Ar flow, represents the state of MgCl$_2$/film as spin coated. The $\nu$(C=O) band of DIBP at that state was super imposable to uncoordinated DIBP (around 1725 cm$^{-1}$), which leads to the conclusion that the donor was not chemisorbed on Mg. The IR signal of ethanol (remnants from the impregnation solution) was also observed. Within the 30 minutes of Ar flow at 30 °C, the $\nu_{max}$(C=O) band broadened and shifted to lower wavenumber (around 1700 cm$^{-1}$) indicating the coordination of DIBP to Mg surface. Simultaneously, we observed the partial removal of residual ethanol from the film. The $\nu_{max}$(C=O) at room temperature was changed from 1704 cm$^{-1}$ to 1715

cm⁻¹, when the DIBP loading was increased from 5% to 50 % of MgCl₂. This is probably due to the incomplete conversion of uncoordinated donor to coordinated donor. On increasing the temperature from 30 °C to 150 °C, all the DIBP/MgCl₂ films showed a clear and progressive shift in $v_{max}(C=O)$ of DIBP to a lower wavenumber (around 1690 cm⁻¹). Further removal of residual ethanol from the film was observed. In the films with DIBP concentration above 20 mol% with respect to MgCl₂, partial desorption of DIBP was also observed. As an example, the ATR-FTIR spectra recorded in between the *in-situ* experiment on MgCl₂/DIBP film with donor to Mg ratio of 0.15 is shown in Figure 3.7.
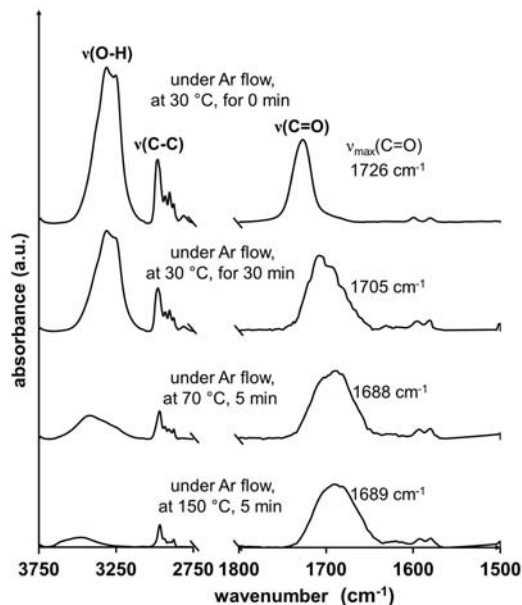


**Figure 3.7.** *Comparative ATR FTIR spectra of DIBP/MgCl₂ film (with a donor to Mg ratio of 0.15) at different stages of the in-situ experiment. v(O-H) is the O-H stretching band of ethanol, v(C-H) is the C-H stretching band of ethanol and donor, v(C-O) is the carbonyl stretching of DIBP.*

The band **'v(O-H)'** represents the O-H stretching mode of ethanol. This band disappeared at 150 °C due to ethanol removal. At 30 °C, the band **'v(C-H)'** represents the C-C stretching modes of ethanol and donor. The ethanol leaves the surface at high temperature and shape of the band changes. At 150 °C, the band

63

**'ν(C-H)'** solely represents C-C stretching modes of DIBP. XPS studies on MgCl$_2$/ethanol films showed that the amount of residual ethanol in the film at 30 °C is around 13% with respect to MgCl$_2$ (see 3.3.1 for details). Based on this, the amount of residual ethanol with respect to MgCl$_2$ in the MgCl$_2$/ethanol/DIBP film was estimated, which is around 18.5 mol% before Ar flow, 9 mol% after 30 minutes of Ar flow and 1 mol% after annealing at 150 °C. The peak maxima of **'ν(C=O)'** shifted from 1705 cm$^{-1}$ to 1688 cm$^{-1}$. After cooling down the ATR system to room temperature, the carbonyl band at 1688 cm$^{-1}$ remains stationary, indicates an irreversible shift.

*In-situ* ATR-FTIR spectra of DIBP/MgCl$_2$ films at different temperatures and different loadings were compared. The surface concentration of DIBP at each temperature was calculated using the quantification method (based on the Beer-Lambert relation) discussed in the previous section. Donor coverage as the function of temperature is shown in Figure 3.8. The maximum amount of DIBP in the MgCl$_2$/DIBP film declines from 38% at 30 °C to 19% at 150 °C. The average peak maxima of the spectra at this stage were around 1692 cm$^{-1}$.
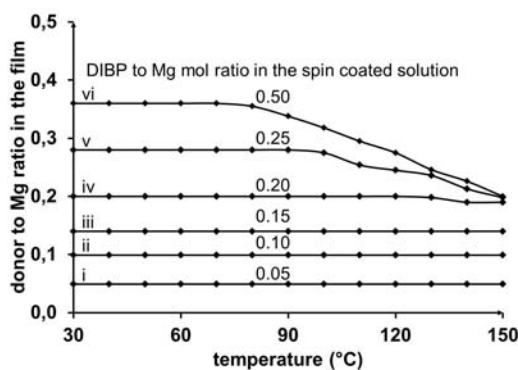


**Figure 3.8.** *Thermal desorption pattern of DIBP (Calculated from integrated peak intensities of DIBP carbonyl band).*

The assignments for the phthalate ester peak found in literature are summarized in Table 3.2.

**Table 3.2.** *Peak assignments for phthalate esters - reported in literature.*

| $\nu$(C=O) band | Assigned $\nu_{max}$(C=O) in $cm^{-1}$ |
|---|---|
| Uncoordinated phthalate ester (liq. state) / physisorbed to six fold Mg at (001) plane | 1732 [15], 1730 [14], 1728 [11, 12, 16, 17] 1733 [13], 1722 [18] |
| Phthalate ester bound to five-fold Mg at (104) edge | 1705 [19], 1704 [17], 1700 [11], 1699 [12,18] |
| Phthalate ester bound to four-fold Mg at (110) edge | 1692 [11], 1684 [17], 1672 [12,18], 1662 [19] |
| Phthalate ester bound to three-fold Mg at corner | 1656 [17], 1650 [12,18] |

In literature, the broad peak around 1687 $cm^{-1}$ was attributed as a superposition of bands due to DIBP coordinated on different surface sites of $MgCl_2$.[11] The shift in $\nu_{max}$(C=O) occurs at elevated temperature can be explained as the changes in the coordination sites on $MgCl_2$ or changes in the coordination mode of DIBP. It is believed that four coordinated $MgCl_2$ (110) site is more acidic than five coordinated $MgCl_2$ (104) site. The interaction of electron donor with $MgCl_2$ (110) site will be stronger than that of (104) site, which result in a lower wavenumber infrared band for electron donor coordinates on $MgCl_2$ (110) site.

## 3.3.4 Peak fitting simulations of experimental ATR-FTIR spectra

The experimental ATR-FTIR spectra (recorded at different donor concentrations and temperatures) of the $MgCl_2$/DIBP films were simulated as a summation of Gaussian-Lorentzian function. Peak fitting simulations were carried out using casa XPS software (http://www.casaxps.com/). Infrared spectra were transferred to casa format. The preliminary constraints used for peak fitting was based on values reported in the literature. ATR-FTIR experiments showed that uncoordinated (pure condensed phase) DIBP band appears around 1725$cm^{-1}$. The

best fit for the entire spectra was achieved when three components with peak maxima around 1725 (component a), 1705 (component b) and 1685 (component c) were used. Based on the information from Table 3.2, the observed $\nu$(C=O) band can be explained as a combination of three overlapping components correspond to the DIBP at three different chemical environments/phases; [a] uncoordinated DIBP, [b] DIBP coordinated on $MgCl_2$ (104) site and [c] DIBP coordinated on $MgCl_2$ (110) site. The relative amounts of the DIBP at above mentioned environments were calculated using the quantification method (discussed above). The constraints used for peak fitting is shown in Table 3.3.

**Table 3.3.** *Constraints used for peak fitting simulations.*

| Symbol | Wavenumber ($cm^{-1}$) | FWHM |
|---|---|---|
| a | 1726 - 1724 | 20 - 30 |
| b | 1706 - 1704 | 30 - 35 |
| c | b - 20 | 35 - 50 |

As an example, the carbonyl stretching and aromatic ring mode bands of DIBP in the DIBP/$MgCl_2$ film (with 15 mol% DIBP loading) at various stages of the *in-situ* experiment is shown in Figure 3.9.
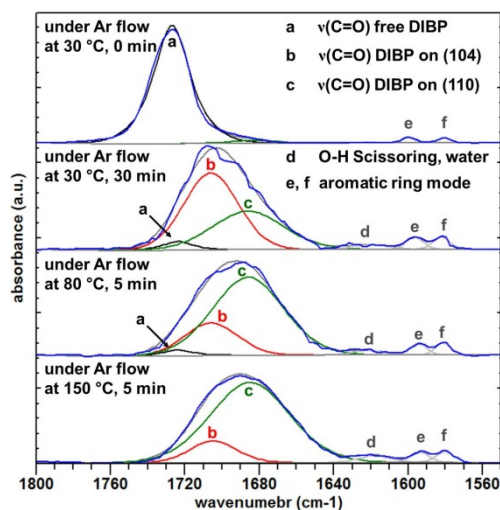


**Figure 3.9.** *Comparative in-situ ATR-FTIR spectra after peak fitting (DIBP to Mg mol ratio of 0.15).*

The changes in the intensity of components are clearly visible. The component 'd' represents the (O-H) scissoring band of moisture. Component 'e' and 'f' represents two aromatic ring stretch bands of DIBP.

The relative amounts of the three DIBP components in the $MgCl_2$ films as a function of temperature are plotted in Figure 3.10.
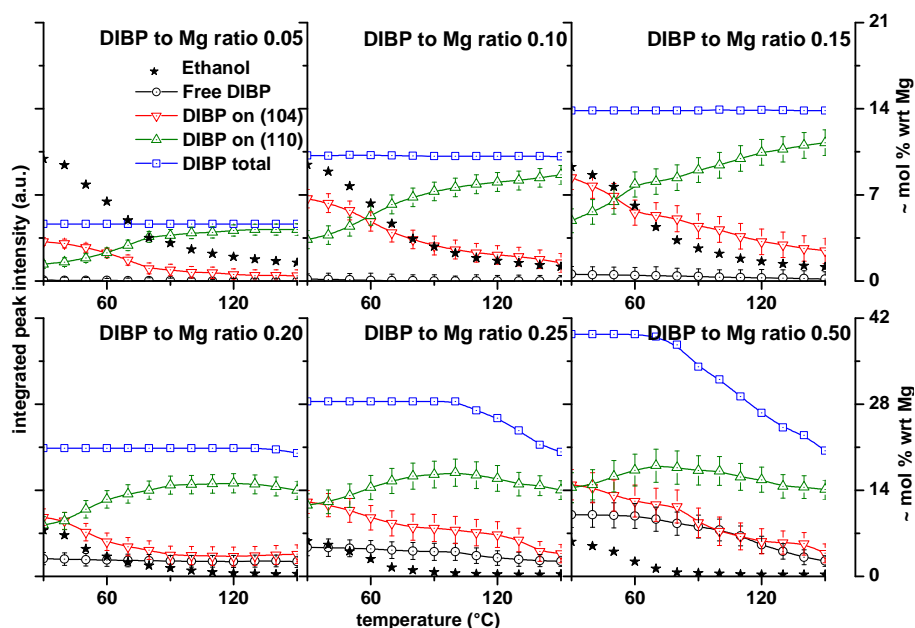


**Figure 3.10.** *Changes in distribution of DIBP among different components with respect to DIBP loading and temperature (the range of error due to the covariance of different components is shown along with each data point). The approximate amount of ethanol derived from the intensity of the (O-H) stretching band is included. The ethanol amounts are only a rough estimate due to the uncertainty of the XPS quantification of ethanol in $MgCl_2$ films.*

DIBP remains uncoordinated in the film after spin coating but prior to argon flow. Large excess of ethanol in the film indicates that the layered $MgCl_2$ crystallites may not yet have formed. Non-layered $MgCl_2$-ethanol adduct formation from a saturated solution of $MgCl_2$ in ethanol is reported in literature.[54] As the ethanol desorbs in the Ar flow, crystalline $MgCl_2$ forms and DIBP starts to

coordinate on $MgCl_2$ (104) and (110) sites. The existence of crystalline $MgCl_2$ in non-annealed films has been confirmed by TEM (see below). Within the 30 minutes of Ar flow, majority of the DIBP coordinates on $MgCl_2$ (104) and (110) sites. At the low donor loading (DIBP to Mg mol ratio < 0.15), DIBP prefers to coordinate on $MgCl_2$ (104) site. At high donor loading (DIBP to Mg mol ratio > 0.15), DIBP does not have any preference between the $MgCl_2$ (104) or (110) site. The amount of residual ethanol remaining in the film (after 30 minutes of Ar flow) decreases with increasing amounts of DIBP in the film. The above two observations lead to the point that, ethanol is preferably coordinates on $MgCl_2$ (110) site, and DIBP coordinates on the remaining surface sites. On thermal annealing, ethanol desorbs from the $MgCl_2$ (110) surface. Simultaneously, DIBP migrates from $MgCl_2$ (104) sites to $MgCl_2$ (110) sites. In the case of high DIBP loadings, the relative abundance of DIBP on $MgCl_2$ (110) sites also increase with increasing temperature, up to a point at which the total intensity of the carbonyl band starts to decrease. This decrease in intensity is only observed in films with donor to Mg ratio above than 0.20. It is assigned to the sintering of $MgCl_2$ crystals at high temperature. The maximum amount of donor coordinated to the $MgCl_2$ surface sites was around 18 mol%.

The outcome of this peak-fitting suggests the conversion of uncoordinated DIBP in to DIBP coordinated on $MgCl_2$ (104) and (110) sites at 30 °C, followed by the migration of DIBP from $MgCl_2$ (104) sites to $MgCl_2$ (110) sites at elevated temperatures. On spin coating, a thin film of $MgCl_2$, ethanol and DIBP is formed. The chemical state of $MgCl_2$ at this stage is either as a non-layered $MgCl_2$-ethanol adducts or $MgCl_2$ crystals (with lateral surface sites coordinated by ethanol) formed from this adduct. At this stage, DIBP remains uncoordinated in the film. During Ar gas flow, large amount of ethanol is removed from the film, and DIBP coordinates to the vacancies created by ethanol on $MgCl_2$ (104) and (110) sites. Upon annealing, DIBP transfers from $MgCl_2$ (104) sites to $MgCl_2$ (110). The transfer of DIBP occurs in the temperature range of 50 - 90 °C, which is the same temperature range at which most of the ethanol removes from the surface. It can be assumed that $MgCl_2$ (110) sites become vacant on ethanol removal, and DIBP migrates from less acidic $MgCl_2$ (104) site to more acidic $MgCl_2$ (110) site. It is already known that $MgCl_2$ (110) sites are unstable in the absence of adsorbent molecule, because

of the high surface energy of the empty surface.[55] SEM-EDX studies on Ostwald ripened crystals of $MgCl_2$ prepared from DIBP/$MgCl_2$/ethanol solution (DIBP to Mg ratio of 0.1), pointed out the formation of crystallites with 120° and 90° edge angles, which indicates the presence of (104) and (110) edge surfaces of $MgCl_2$ with five and four fold Mg ions respectively.[56] The coexistence of $MgCl_2$ (104) and (110) sites in the $MgCl_2$ crystal (in the presence of DIBP) is in line with the results of peak fitting.

## 3.4 Summary

A sensitive method was developed for the investigation of coordinated donor on flat-model Ziegler-Natta catalysts by means of *in-situ* ATR-FTIR. The method is based on the linear relationship between the carbonyl stretching band integrated peak intensity of DIBP and concentration of DIBP (concentration of DIBP in the $MgCl_2$/DIBP adduct prepared) in $MgCl_2$ films. The results were calibrated by XPS studies on an F-labelled homologue of DIBP, which is the 4-fluoro-diisobutylphthalate (FDIBP). The newly synthesized FDIBP displayed a well-quantifiable fluorine 1s peak during XPS-studies of spincoated $MgCl_2$/Ethanol/Donor surfaces, as opposed to the hitherto used, poorly resolved carbon signals of DIBP. ATR-FTIR spectra of the flat surfaces showed a sufficient similarity in coordination behaviour between FDIBP and DIBP to regard 4-fluoro-diisobutylphthalate as a possible substitute for DIBP in future XPS studies on flat-model catalyst surfaces. Changes in the coordination behaviour of DIBP on $MgCl_2$ were followed by *in-situ* ATR-FTIR spectroscopy. Directly after impregnation, DIBP shows no interaction with $MgCl_2$. However, as some ethanol desorbs at 30 °C in flowing argon, DIBP binds to the $MgCl_2$. Based on values reported in literature, we tentatively explain the observed changes of the $\nu$(C=O) adsorption bands as a combination of three overlapping components assigned to uncoordinated DIBP, DIBP adsorbed to $MgCl_2$ (104) and to DIBP adsorbed to $MgCl_2$ (110). Based on our tentative assignment, we derive the following conclusions:

- Before annealing, we have observed a slight preference of the DIBP donor for the $MgCl_2$ (104) site. This preference is probably induced by the presence of co-adsorbed ethanol.

- Upon annealing, DIBP transfers from $MgCl_2$ (104) sites to $MgCl_2$ (110) sites as these adsorption sites become vacant due to desorption of ethanol from $MgCl_2$ (110) sites.

- The saturation loading of DIBP after annealing at 150 °C is 18 mol% with respect to Mg. Excess donor is removed from the film under Ar flow. The DIBP loss is attributed to sintering of the $MgCl_2$ platelets.

The results show the feasibility of preparing Ziegler-Natta catalysts with different donor concentration on different $MgCl_2$ surface sites. Since the activity and selectivity of the catalyst is heavily depends on the coordination behaviour of internal donor, it is interesting to compare the activity and selectivity of these catalysts. The quantification method discussed in this chapter can be applied to different types of donors used in Ziegler-Natta catalysis. Moreover, this quantitative information will be useful for the *in-situ* studies on the further steps of catalyst preparation, such as treatment with $TiCl_4$ and aluminium alkyls.

However, the molecular level structure of the coordination sites (surface site structure, DIBP coordination mode and DIBP coverage on surface sites) is still unknown. Molecular structures and the corresponding wavenumbers for the carbonyl bands of adsorbed DIBP can only be found by DFT calculations.

## 3.5 References

(1)  Terano, M.; Kataoka, T. *J. Polym. Sci. A: Polym. Chem.* **1990,** *28*, 2035.

(2)  Terano, M.; Kataoka, T. *Macromol. Chem.* **1987,** *188*, 1477.

(3)  Ferreira, M. L.; Damiani, D. E. *J. Polym. Sci. A: Polym. Chem.* **1994,** *32*, 1137.

(4)  Jeong, Y. T.; Lee, D. H. *Macromol. Chem.* **1990,** *191*, 1487.

(5)  Chien, J. C. W.; Dickinson, L . C.; Vizzini, J. C. *J. Polym. Sci. A: Polym. Chem.* **1990,** *28*, 2321.

(6)  Chien, J. C. W.; Wu, J. C.; Kuo, C. I. *J. Polym. Sci.: Polym. Chem.* **1983,** *21,* 725.

(7)  Spitz, R.; Lacombe, J. L.; Primet, M. *J. Polym. Sci.: Polym. Chem* **1984,** *22,* 2611.

(8)  Bache, Ø.; Ystenes, M. *Appl. Spec.* **1994,** *48,* 985.

(9)  Potapov, A. G.; Bukatov, G. D.; Zakharov, V. A. *Kinet. Catal.* **2007,** *48,* 2003.

(10) Cui, N.; Ke, Y.; Li, H.; Zhang, Z.; Guo, C.; Lv, Z.; Hu, J. *J. Appl. Polym. Sci.* **2006,** *99,* 1399.

(11) Zohuri, G.; Ahmadjo, S.; Jamjah, R.; Nekoomanesh, M. *Iran. Polym. J.* **2001,** *10* (3), 149.

(12) Potapov, A. G.; Bukatov, G. D.; Zakharov, V. A. *J. Mol. Catal. A: Chem.* **2006,** *246* (1-2), 248.

(13) Kissin, Y. V.; Liu, X. S.; Pollick, D. J.; Brungard, N. L.; Chang, M. *J. Mol. Catal. A: Chem.* **2008,** *287* (1-2), 45.

(14) Arzoumanidis, G. G.; Karayannis, N. M. *Appl. Catal.* **1991,** *76*, 221.

(15) Yang, C. B.; Hsu, C. C.; Park, Y. S.; Shurvell, H. F. *Eur. Polym. J.* **1994,** *30* (2), 205.

(16) Makwana, U.; Naik, D. G.; Singh, G.; Patel, V.; Patil, H. R.; Gupta, V. K. *Catal. Lett.* **2009,** *131* (3-4), 624.

(17) Singh, G.; Kaur, S.; Makwana, U.; Patankar, R. B.; Gupta, V. K. *Macromol. Chem. Phys.* **2009,** *210* (1), 69.

(18) Potapov, A. G.; Bukatov. G. D.; Zakharov. V. A. *J. Mol. Catal. A: Chem.* **2010,** *316* (3-4), 95.

(19) Stukalov, D. V.; Zakharov, V. A.; Potapov, A. G.; Bukatov, G. D. *J. Catal.* **2009,** *266* (1), 39.

(20) Ystenes, M.; Bache, Ǿ.; Bade, O. M.; Blom, R.; Eliertsen, J. L.; Nirisen, Ǿ.; Ott, M.; Svendsen, K.; Rytter, E. In *Future technology for Polyolefin and Olefin Polymerization catalysis;* Terano, M.; Shiono, T., Eds.; Technology and education Publishers: Tokyo, **2002,** 184.

(21) Chadwick, J. C. *Macromol. Symp.* **2001,** *173*, 21.

(22) Yang, A. C.; Garland, C. W. *J. Phys. Chem.* **1957,** *61* (11), 1504.

(23) Arai, H.; Tominaga, H. *J. Catal.* **1976,** *43* (1-3), 131.

(24) Srinivas, G.; Chuang, S. S. C.; Debnath, S. *J. Catal.* **1994,** *148* (2), 748.

(25) Chuang, S. S. C.; Brundage, M. A.; Balakos, M. W.; Srinivas, G. *Appl. Spectrosc.* **1995,** *49* (8), 1151.

(26) Balakos, M. W.; Chuang, S. S. C.; Srinivas, G.; Brundage, M. A. *J. Catal.* **1995,** *157* (1), 51.

(27) Rasband, P. B.; Hecker, W. C. *J. Catal.* **1993,** *139* (2), 551.

(28) Srinivas, G.; Chuang, S. S. C. *J. Catal.* **1993,** *144* (1), 131.

(29) Nakahama, K.; Kawaguchi, H.; Fujimoto, K. *Langmuir* **2000,** *16* (21), 7882.

(30) Cavanagh, R. R.; Yates, J. T. *J. Chem. Phys.* **1981,** *74* (7), 4150.

(31) Tan, C. D.; Ni, J. F. *J. Chem. Eng. Data* **1997,** *42* (2), 342.

(32) Bugay, D. E. *Adv. Drug Deliver. Rev.* **2001,** *48* (1), 43.

(33) Planinsek, O.; Planinsek, D.; Zega, A.; Breznik, M.; Srcic, S. *Int. J. Pharm.* **2006,** *319* (1-2), 13.

(34) Tickanen, L. D.; Tejedor-Tejedor, M. I.; Anderson, M. A. *Langmuir* **1991,** *7*, 451.

(35) Leewis, C. M.; Kessels, W. M. M.; van de Sanden, M. C. M.; Niemantsverdriet, J. W. (Hans). *J. Vac. Sci. technol.* **2006,** *24* (2), 296.

(36) Harrick, N. J. *J. Opt. Soc. Am.* **1965,** *55*, 851.

(37) Müller, M.; Keßler, B. *Langmuir* **2011,** *27* (20), 12499.

(38) Kaushik, V. K.; Gupta, V. K.; Naik, D. G. *Appl. Surf. Sci.* **2006,** *253* (2), 753.

(39) Andoni, A.; Chadwick, J. C.; Milani, S.; Niemantsverdriet, J. W. (Hans).; Thüne, P. C. *J. Catal.* **2007,** *247* (2), 129.

(40) Andoni, A.; Chadwick, J. C.; Niemantsverdriet, J. W. (Hans).; Thüne, P. C. *Macromol. Rapid Commun.* **2007,** *28* (14), 1466.

(41) Da Silva, A. A.; Alves, M. D. M.; dos Santos, J. H. Z. *J. Appl. Polym. Sci.* **2008,** *109* (3), 1675.

(42) Zhao, X.; Zhang, Y.; Song, Y.; Wei, G. *Surf. Rev. Lett.* **2007,** *14* (5), 951.

(43) Mori, H.; Hasebe, K.; Terano, M. *J. Mol. Catal. A: Chem.* **1999,** *140*, 165.

71

(44)  Xiao-hong, G.; Guang-hao, C.; Chii, S. *J. Environ. Sci.* **2007,** *19*, 438.

(45)  Andoni, A.; Chadwick, J. C.; Niemantsverdriet, J. W. (Hans).; Thüne, P. C. *Macromol.  Symp.* **2007,** *260*, 140.

(46)  Strother, T.; Knickerbocker, T.; Russell, J. N.; Butler, J. E.; Smith, L. M.; Hamers, R. J. *Langmuir* **2002,** *18* (4), 968.

(47)  De Giglio, E.; Cometa, S.; Cioffi, N.; Torsi, L.; Sabbatini, L. *Anal. Bioanal. Chem.* **2007,** *389*, 2055.

(48)  Ahmed, S. F.; Mitra, M. K.; Chattopadhyay, K. K. *Appl. Surf. Sci.* **2007,** *253* (12), 5480.

(49)  Snow, A. W.; Foos, E. E.; Coble, M. M.; Jernigan, G. G.; Ancona, M. G. *Analyst* **2009,** *134* (9), 1790.

(50)  Thomas, H. R.; O'Malley, J. J. *Macromolecules* **1979,** *12* (2), 323.

(51)  Thüne, P. C.; Niemantsverdriet, J. W. (Hans). *Surf. Sci.* **2009,** *603*, 1756-1762.

(52)  Andoni, A.; Chadwick, J. C.; Niemantsverdriet, J. W. (Hans).; Thüne, P. C. *Catal. Lett.* **2009,** *130*, 278.

(53)  Skrzypek, J.; Sadlowski, J. Z.; Lachowska, M.; Turzanski, M. *Chem. Eng. Process.* **1994,** *33* (6), 413.

(54)  Sozzani, P.; Bracco, S.; Comotti, A.; Simonutti, R.; Camurati, I. *J. Am. Chem. Soc.* **2003,** *125*, 12881.

(55)  Busico, V.; Causa, M.; Cipullo. R.; Credendino, R.; Cutillo, F.; Friederichs, N.; Lamanna, R.; Segre, A.; Castelli, V. V. A. *J. Phys. Chem C* **2008,** *112*, 1081.

(56)  Andoni, A.; Chadwick, J. C.; Niemantsverdriet, J. W. (Hans).; Thüne, P. C. *J. Catal.* **2008,** *257,*81.

# 4

# Isolation of MgCl$_2$/phthalate precursor phases: a combined experimental and DFT study

This study collects parts of results of a combined experimental and computational approach to supported Ziegler-Natta catalysts coming out of the cooperation between TU/e and Università di Napoli "Federico II"; most of them are still unpublished and they have been extracted by manuscripts in preparation of the two research groups.

73

# Abstract

*By exploiting the influence of the preparation method and of the Lewis bases in the precursor solution on the surface structure of $MgCl_2$ crystals, a variety of $MgCl_2$ films with different $MgCl_2$ surface structures were prepared. Interaction of $MgCl_2$ and various internal donors (Lewis bases)– used in industrial Ziegler-Natta catalysts – were monitored by attenuated total internal reflection - Fourier transform infrared spectroscopy (ATR-FTIR). IR spectra of different $MgCl_2$/diester donor surface species were isolated by in-situ adsorption of diesters exclusively/predominately on one particular $MgCl_2$ surface site. Molecular level structure of the $MgCl_2$/diester surface species was predicted by periodic DFT-D calculations. The morphology of $MgCl_2$ and $MgCl_2$/diester films was studied by transmission electron microscopy (TEM). TEM revealed a preferential orientation of ClMgCl layers (001) parallel to the lateral film dimensions. This orientation becomes pronounced upon annealing. In the absence of a donor, the $MgCl_2$ grows into large crystals aligned in large domains upon annealing. Both crystal growth and alignment are impeded by the presence of the donor. Based on IR results, we propose the reconstruction of $MgCl_2$ (110) surface site to $MgCl_2$ (104) and sintering of $MgCl_2$ crystals in the absence of internal donor. Compared to bidentate donors such as diisobutyl phthalate (DIBP) and 9,9'-bis(methoxymethyl)fluorene (BMMF), interaction of monodentate donor such as ethyl benzoate (EB) with $MgCl_2$ was very weak.*

# 4.1 Introduction

**M**gCl$_2$ is a key component in heterogeneous Ziegler-Natta olefin polymerization catalysts with the role of acting as a support material into which transition metal complexes, such as TiCl$_4$ are bound, thereby generating catalytically active sites.[1] The basal (001) surface of MgCl$_2$ is composed of fully saturated Cl atoms; therefore does not provide any site for a TiCl$_4$ molecule to adsorb. Alternative cuts of the crystal expose unsaturated Mg atoms which are possible sites for TiCl$_4$ adsorption. Most commonly, two different types of under-coordinated Mg ions are expected to be found. One type is five-coordinate, and the other is four-coordinate. The former is found in the (104) face and the latter is found on (110) face.[2] Structures of surface TiCl$_4$ species and active sites have been discussed based on the MgCl$_2$ (110) and (104) surfaces.[3-6] The incorporation of a Lewis base is essential in order to improve stereoselectivity in propylene polymerization. It is generally believed that donor molecules adsorb on MgCl$_2$ surface sites and interact with nearby Ti species in a non-bonded manner to improve the stereospecificity of the Ti species.[7-13]

Recently, Busico and coworkers reported a combined experimental and periodic DFT study about the relative stability of lateral faces in MgCl$_2$ crystals.[14,15] DFT-D studies indicate MgCl$_2$ (104) as the dominant lateral surface in well-formed large MgCl$_2$ crystals. The equilibrium crystal morphology was generated using Wulff's construction.[15] The translational mobility of silane molecules in ball milled MgCl$_2$/silane adducts were monitored using High-Resolution Magic-Angle-Spinning (HR-MAS) ^{1}H NMR. Based on the HR-MAS ^{1}H NMR results, they concluded that, MgCl$_2$ (104) is the dominant lateral surface in ball milled MgCl$_2$/silane adduct too. Meanwhile, they found a small fraction (ca. 20% of the total lateral surface) is representing the more unsaturated Mg sites which correspond to four-fold (110) and/or three-fold Mg (corners) or other defective sites in the MgCl$_2$ matrix.[14]

On the other hand, recent DFT calculations and experimental studies clearly indicated that TiCl$_4$ is predominantly adsorbed on the (110) sites (as a monomeric species).[2,16-20] TiCl$_4$ binding to (104) sites has been calculated to be weak.

Therefore, it was an interesting research question whether the electron donor affect the relative proportion of various surface sites during or after $MgCl_2$ crystal growth.

Earlier in our research group, Andoni and coworkers reported that the presence of 9,9'-bis(methoxymethyl)fluorene (BMMF) leads to the formation of $MgCl_2$ crystals with only 120° edge angles.[21] This is indicative of the predominant formation of one lateral surface. Turunen and coworkers modelled the methanol covered $MgCl_2$ crystallites to study the influence of electron donors on $MgCl_2$ crystallite microstructure.[22] They found that increasing crystallite size and the existence of higher coordination numbers in the edge Mg atoms enhance crystal stability. Pure $MgCl_2$ crystallites showed dominance of (104) crystal surface over (110). As opposed to pure $MgCl_2$ crystals, crystallites with the highest (110) to (104) surface site ratio became more stable when they saturate the crystals with methanol. Similar studies with dimethyl ether covered $MgCl_2$crystallites confirmed that, in the absence of donors, such as in the simple mechanical milling of $MgCl_2$, it is reasonable to expect large crystallites presenting (104) edges; whereas in the presence of an electron donor smaller crystallites with (110) edges should be formed.[23]

As a summary, the most stereoselective Ti species probably look very similar to an electron donor modified Ti species adsorbed on (110) lateral face of $MgCl_2$; however the predominant lateral face in the absence of an electron donor is the (104).[15,24] Upon titanation, monomeric and dimeric Ti species are formed on the (104) surface. It is quite accepted that the dimeric Ti species – $Ti_2Cl_8$– on (104) itself can generate stereospecificity. As a result, even in the absence of electron donor, $TiCl_4/MgCl_2$ + $AlEt_3$ catalysts produces a significant amount of isotactic polymer.

Figure 4.1 shows the differences in the proximity of internal donor to the active sites. The mechanism through which the electron donor enhances the stereoselectivity of active sites on (110) can be explained by the coordination of electron donors very close to active sites (coadsorption of $TiCl_4$ and electron donor).[25] On the other side, for (104) surface, the donor coordinates a bit far from

the active site. Compared to (110) surface, the influence of the donor on Ti species could be less pronounced on (104) surface.
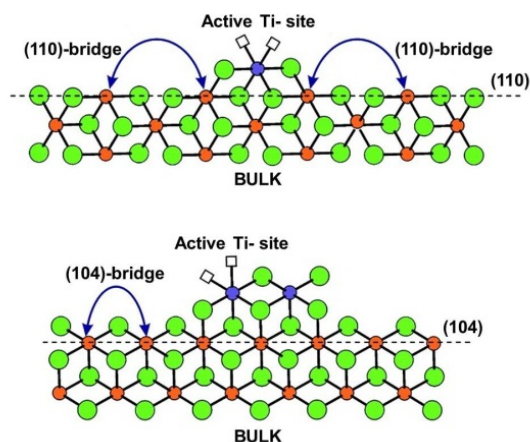


**Figure 4.1.** *A model of active Ti sites on (104) and (110) MgCl$_2$sites with adjacently bound Lewis bases.*[24]

There are four ways in which the donors (containing two oxygen atoms that can bind to Mg) can coordinate to MgCl$_2$ surface:[2,18,26]

- coordination of one oxygen of the donor molecule to one Mg atom, that is the 'monodentate' or monocoordination mode,
- coordination of both oxygens of the donor to the same Mg atom, namely the 'chelate' coordination mode (expected on four fold Mg sites),
- coordination of both oxygens of the donor to two Mg atoms on the same MgCl$_2$ surface, the 'bridge'; coordination mode,
- coordination of both oxygens of the donor to two mg atoms on the different (adjacent) MgCl$_2$ layers, the 'zip' coordination mode.[18]

As an example, four different coordination modes of a phthalate ester on surface Mg ion are given in Figure 4.2.
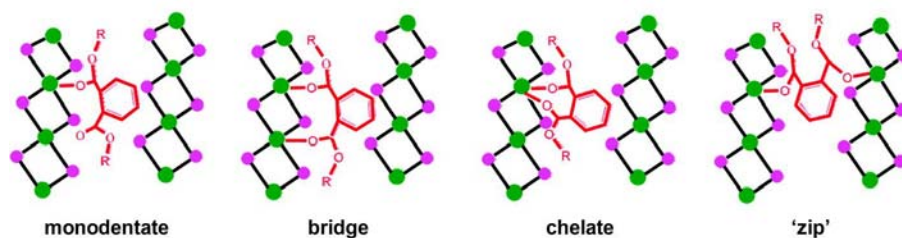
**Figure 4.2.** *Simplified scheme of four possible coordination modes of a phthalate electron donor on MgCl$_2$.*[26]

Vibrational spectroscopy is a powerful technique to provide information at the molecular level. The vibrational spectra are sensitive to the molecular properties, such as type of atoms, chemical bonding, geometry, and intra/intermolecular interactions.[27-29] Absorption bands characteristic of the chemical group interacting with MgCl$_2$, (such as C-O stretching vibrations in ethyl benzoate, dialkyl phthalate, dialkyl succinate or diether donors) have been used to confirm the binding of donors on MgCl$_2$. Especially, the intense and distinctive IR bands of MgCl$_2$/ester and MgCl$_2$/diester complexes became a topic of interest for researchers in Ziegler-Natta catalysis.[30-43] Due to the formation of different complexes of donor with MgCl$_2$ and TiCl$_4$, the envelope of $\nu$(C=O) is always broad. Some attempts were made to estimate the distribution of donor in different complexes by means of resolving the $\nu$(C=O) band into components.[35,38-43] The peak positions of the components selected for resolving the spectra were taken from the spectra of MgCl$_2$-donor molecular complexes.[33-35] In all cases, the components used to explain the spectra were really broad with a full width half maxima (FWHM) of more than 40 cm$^{-1}$. The adjacently positioned components cause large errors in the quantification due to covariance. The error due to covariance increases with the increase in the FWHM; and decreases with the increase in the distance between the adjacent components. Therefore, uncertainty in the peak assignment in combination with covariance results in large errors. In **Chapter 3** we made an attempt to explain the broad $\nu$(C=O) band of diisobutyl phthalate (DIBP) based on the values reported in literature, which is also not free from these errors. One solution to overcome the issue is to isolate/prepare MgCl$_2$ crystals with donor coordination preferably on one type of surface sites. The IR signatures of these complexes will give some idea about the position, shape and

78

broadness of the band. The other method is to predict the relative positions of IR signatures of MgCl$_2$/donor complexes using computational methods. Computational modelling of MgCl$_2$ bulk and surface structures by means of density functional theory methods including dispersion (DFT-D) has been reported.[14,15] More recently, binding of TiCl$_4$ to MgCl$_2$ surfaces using DFT and DFT-D methods has been published.[20] Adsorption of several small donor molecules (H$_2$O, NH$_3$ and EtOH) as well as dimethoxy silane (model for industrially used more bulky silane) on MgCl$_2$ surfaces have been obtained using the same approach.[44] Periodic DFT-based methods have been used (only in recent years) to calculate the IR spectra of crystalline solids.

In this chapter, we exploit the possibilities of isolating MgCl$_2$/DIBP surface species. MgCl$_2$/DIBP surface species can be isolated by altering the relative proportions of MgCl$_2$ surface sites in the crystals or blocking one particular site with some other molecule which does not have IR bands interfering with ν(C=O) regions of DIBP. From the introduction, it is clear that the preparation method have a large influence on the final structure of MgCl$_2$ crystallites. In **Chapter 3**, we observed changes in ν(C=O) DIBP along with removal of residual ethanol. A thin film analogue for MgCl$_2$ support was prepared by spin coating a solution of MgCl$_2$ in ethanol, followed by removing different amounts of ethanol by means of annealing under Ar flow. These films were then exposed to hydrocarbon solutions of DIBP and monitored by *in-situ* ATR-FTIR. We compared the ν(C=O) DIBP signals in these films. We also studied the *in-situ* coordination of ethyl benzoate (EB) on MgCl$_2$ films with different ethanol concentration. EB binds to MgCl$_2$ surface only in monodenate fashion; which results in a relatively simple ν(C=O) signal compared to ν(C=O) DIBP. The comparison of ν(C=O) EB and ν(C=O) DIBP will provide some idea about the coordination mode of DIBP in these complexes. Earlier in our research group, Andoni and coworkers reported that the presence of 9,9'-bis(methoxymethyl)fluorene (BMMF) leads to the formation of MgCl$_2$ (110) lateral termination, which results in MgCl$_2$ crystals with only 120° edge angles.[21] We also studied the coordination behaviour of DIBP on MgCl$_2$/BMMF films, which is believed to be a MgCl$_2$ crystal with exclusively/predominantly (110) lateral terminations. Meanwhile, the morphology

of $MgCl_2$ and $MgCl_2$/DIBP films, supported on window etched silicon based grids, were studied by TEM.

Using periodic DFT-D calculations, the chemisorption of phthalate ester (dimethyl phthalate – dimethyl homologue of DIBP) on $MgCl_2$ (104) and (110) surfaces were modelled, and the corresponding vibrational spectra were simulated (these works were performed by our collaborators at the University of Naples).

## 4.2 Experimental

### 4.2.1 Materials

Anhydrous magnesium chloride (ball milled, 99.9%), heptane (99%) and ethyl benzoate (99%)were purchased from Aldrich Chemicals and used as received. Absolute ethanol (99.9%) and diisobutyl phthalate (97%) were purchased from Merck Chemicals and used as received. 9,9'-bis(methoxymethyl)fluorene (99%) was obtained from LyondellBasell[®] and used as received. Argon (grade 6.0) was purchased from Linde and used after passing through a $Cr/\gamma-Al_2O_3$ tube.

### 4.2.2 Preparation of $MgCl_2$/donor thin films

From a bulk solution of $MgCl_2$ (105 mmol $dm^{-3}$) in ethanol, a series of solutions with donor/$MgCl_2$ molar ratios of 0.05, 0.15, 0.20 and 0.25 was prepared. Donor-free $MgCl_2$ films also were prepared. All these preparations were carried out in $N_2$ atmosphere. In a typical procedure, the solution was spin coated (2800 r.p.m.) under glovebox conditions onto the ZnSe crystals (for ATR-FTIR studies) or$SiO_2$/$SiN_X$ TEM wafers (for TEM studies). Donor/$MgCl_2$ films (co-impregnated donor) were used for temperature programmed *in-situ* ATR-FTIR studies on the changes in donor coordination behaviour. Donor free $MgCl_2$ films were used for monitoring the *in-situ* coordination of internal donor on $MgCl_2$; by means of ATR-FTIR.

### 4.2.3 Preparation and loading of donor/heptane solution

A solution of the donor in heptane, was prepared under glovebox conditions (20 μL/mL heptane). We choose heptane as the solvent for monitoring *in-situ* coordination of donor on $MgCl_2$, since the IR spectrum of heptane does not contain

any signals around 1800 cm$^{-1}$ to 1600 cm$^{-1}$ where the ν(C=O) bands of esters, diesters and succinates appear. The solution was filled in one of the lines of small volume dispenser (discussed in **Chapter 2**) using a syringe. In the same manner, the remaining three lines were filled with pure heptane. The dispenser unit is then transferred from the glovebox and connected to the ATR reactor line.

## 4.2.4 Analytical techniques

All FTIR spectra were collected using a Nicolet Protégé 460 Fourier transform infrared spectrometer equipped with a heated HATR flow cell for Spectra-Tech ARK with a ZnSe 45° crystal (cut-off at 800 cm$^{-1}$). The FTIR spectra of uncoordinated EB, DIBP, BMMF and DIPS were recorded using Nicolet Smart Golden Gate equipment with a diamond crystal (cut-off at 800 cm$^{-1}$). The coated ZnSe crystal was mounted and sealed under a nitrogen atmosphere in an ATR-cell. In order to control the amount of residual ethanol in the film (to make it comparable with the films that did undergo high vacuum conditions prior to TEM measurements) and simultaneously prevent moisture and oxygen from atmosphere entering into the system, Ar gas was flowed (controlled flow) through the cell for 30 min at 2 bar and 30°C. FTIR spectra were measured in absorbance mode using a ZnSe background (taken at 30 °C) with a resolution of 4 cm$^{-1}$ and 4 scans per measurement.

For temperature programmed *in-situ* studies, the ATR set up was gradually heated under argon flow with isothermal steps (10 °C difference) from 30 °C up to 150 °C. FTIR spectra were recorded at the end of each isothermal step (5 min), against ZnSe background (taken at that particular temperature).

For monitoring *in-situ* coordination of internal donor, donor/heptane solution (from the small volume dispenser) was flowed through the cell for 20 min at a flow rate of 0.1 mL donor solution/min. Then heptane (from the small volume dispenser) was flowed through the cell for 60 min at a flow rate of 0.1 mL heptane/min. A solution of the donor in heptane, was prepared under glovebox conditions (20 μL/mL heptane). FTIR spectra were measured at the regular intervals (approximately every two minutes).

TEM studies were carried out on an FEI Tecnai 20 (Sphera), operated at 200 kV. The custom-made TEM wafers have dimensions of 20x20 mm$^2$ to allow homogenous distribution of solution during spin coating. After deposition of MgCl$_2$/DIBP solution via spin coating, the TEM wafer was carefully broken into individual TEM grids. A single TEM grid was mounted on the sample holder. Then it was transferred to the transmission electron microscope, under an inert atmosphere (using TEM transfer tube). This methodology was already applied for flat-model systems with iron oxide nanoparticles in morphology studies related to the carbon nanotube growth and Fischer-Tropsch catalysis[45,46] and tin oxide nanoparticles produced by atmospheric pressure chemical vapor deposition.[47]

## 4.2.5 Computational modelling

All *ab initio* calculations were performed using the CRYSTAL09 periodic code; the code employs a Guassian type basis set.[48] All the calculations were done within the framework of Density Functional Approximation (DFT). The hybrid Becke, three parameters, Lee-Yang-Parr (B3LYP) functional was adopted. A general drawback of all common GGA functionals, including hybrids, is that they cannot describe long-range electron correlations that are responsible for van der Waals (dispersive) forces. Since dispersion plays a key role in many chemical systems and, in particular, it has a role determining the orientation of donor molecules on surfaces, it was necessary to apply a correction to the energy obtained with the standard density functional methods. When dispersion is included in the system, the total computed energy is given by Equation 4.1.

$$E_{DFT-D} = E_{DFT} + E_{disp} \qquad (4.1)$$

in the equation $E_{disp}$ is the empirical dispersion correction originally proposed by Grimme[49] and referred to as the D2 correction (Equation 4.2).

$$E_{disp} = S_6 \sum_g \quad \sum_{ij} f\left(R_{ij,g}\right) \frac{C_6^{ij}}{R_{ij,g}^6} \qquad (4.2)$$

Where, the summation is over all atom pairs $i,j$ and lattice vectors g which define the cells of the $j^{th}$ atom, with the exclusion of the $i = j$ contribution for $\mathbf{g} = 0$; $C_6^{ij}$ is the dispersion coefficient for the ij$^{th}$ pair of atoms; $f$ is a damping function used to avoid near-singularities for small inter-atomic distances $Rij,\mathbf{g}$; $S_6$ is a scaling

factor that depends on the adopted DFT method (for B3LYP $S_6$= 1.0). For the specific case of B3LYP calculations, the modification proposed by Civalleri and coworkers[50] to a Grimme's standard set of parameters has been adopted. The corrections (when activated during a geometry optimization), were added to the energy and its gradient to determine the final geometry. The inclusion of dispersive forces during the optimization highlights their role in determining the most stable geometry of adsorption.

Split valence triple-$\zeta$ basis sets plus polarization (TZVP) functions have been applied to describe all the elements (Mg, Ti and Cl atoms)[20] and a Ahlrichs VTZ[51] plus polarization quality has been adopted for the adsorbed molecules. In the latter case, a preliminary study was also carried out to optimize the coefficients of the polarization Gaussian functions ($\alpha_{pol}$) thus enabling more accurate calculations of adsorption energy and vibrational frequencies. The choice was aimed at reducing the Basis Set Superposition Error (BSSE), since in this kind of system it can become quite large; particularly when the dispersion correction is included during the optimization process (when the molecule and the surface become closer). To check the quality of our predictions, the BSSE has been computed with the counterpoise method.[52]

The Gauss-Legendre quadrature and Lebedev schemes are used to generate angular and radial points of a pruned grid consisting of 75 radial points and maximum number of 974 angular points over which electron density and its gradient are integrated.[53] Values of the tolerance that control the Couloumb and exchange series in periodical systems were set to 7 7 7 7 20. All the bielectonic integrals, Coloumb and exchange, were evaluated exactly.

For all B3LYP-D calculations, 10 K points have been adopted. Internal coordinates and cell parameters have been optimized using the analytical gradient method to optimize the atomic positions. The largest system [dimethyl phthalate interacting with (110) surface at $\theta$ = 1/2] considered for vibrational analysis includes 144 atoms in the unit cell.

The interaction energy, $\Delta E_{ads}$, per unit cell per adsorbate molecule is a negative quantity (for a bounded system), defined according to the Equation 4.3:

$$\Delta E_{ads} = \frac{(E_{adduct} - E_{slab} - x\,E_D)}{x} \qquad (4.3)$$

$E_{adduct}$ is the electronic energy of a fully relaxed surface slab S in interaction with the adsorbate molecule M; $E_{slab}$ is the energy of a fully relaxed slab alone; $E_D$ is the molecular energy of the free fully optimized adsorbate molecule.

All $\Delta E_{ads}$ values are given per coordinated mole of donor (regardless of its coordination mode), using fully relaxed unit cells for bare and covered crystals. Vibrational analysis was then carried out to calculate $\Delta S_{ads}$ at standard conditions (p = 1 bar, T = 298 K) and hence evaluate the Gibbs free energy of adsorption. Periodic DFT-based methods have only recently been used to perform vibrational analysis of crystalline solids. Differently from most available periodic codes which are based on the plane-wave basis sets in combination with pseudo-potentials, the CRYSTAL09 code employ Gaussian type local basis sets and therefore allowed easy implementation hybrid functionals such as B3LYP, which is important in view of the proven reliability of these functionals in computing vibrational properties.[54-56] The vibrational analysis used is similar to the computational scheme of may molecular codes, using analytical gradients of energy with respect to nuclear positions and numeric differentiation to obtain the hessian at the central point of the first Brillouin zone (Γ point, point $k = 0$ in BZ). For the geometrical treatment of edges, the development version of the CRYSTAL09 code was adopted for all the *ab initio* calculations.

Due to the complex nature of adsorbed donors and adsorbing surfaces, many models have been built, also on the basis of those proposed in literature, in particular different degree of coverage have been also considered studying the effect of donor molecules crowding on surfaces.

## 4.3 Results and discussion

### 4.3.1 Morphology of MgCl$_2$ and MgCl$_2$/DIBP films

Transmission electron microscopy was used to study the morphology of MgCl$_2$ and MgCl$_2$/DIBP films. The TEM images of annealed (at 150 °C, for 1 h) and non-annealed (as spin coated) MgCl$_2$ and MgCl$_2$/DIBP films were compared (Figure 4.3).
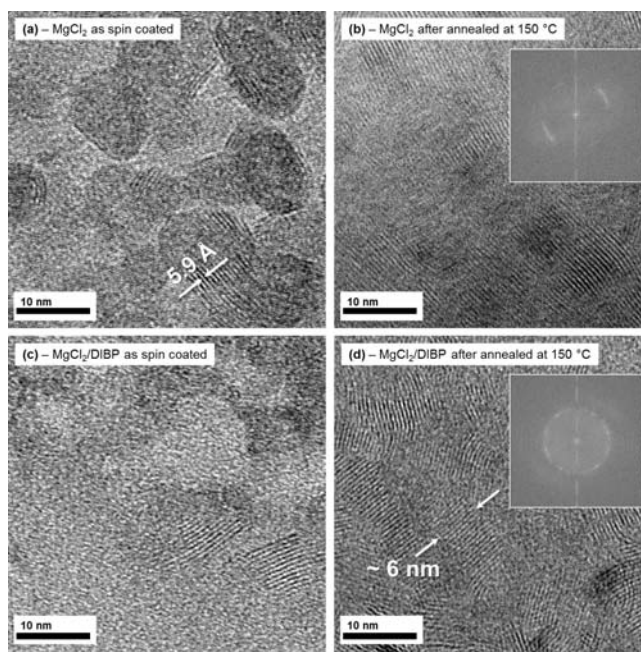
84

**Figure 4.3.** *TEM images of MgCl₂ and MgCl₂/DIBP films: (a) MgCl₂ film at 30 °C. (b) MgCl₂ film after annealing at 150 °C for 1h; FFT view of the same as inset. (c) MgCl₂/DIBP film at 30 °C. (d) MgCl₂/DIBP film after annealing at 150 °C for 1h; FFT view of the same as inset.*

The concentration of DIBP in the precursor solution for MgCl₂/DIBP film preparation was 15 mol% with respect to Mg. Note that the non-annealed films are already going through the vacuum conditions of TEM measurements. Therefore, we expect these samples to be compared to the ATR films after a 30 minute treatment in flowing argon. In all cases, MgCl₂ platelets were observed. In contrast to films prepared by chemical vapour deposition in ultra-high vacuum on metallic surfaces,[57-59] these platelets were arranged parallel to the surface normal (edge-on orientation). This may be due to the chemical affinity of coordinatively unsaturated crystal side edges with the underlying SiO₂ layer of TEM grid. The diffraction patterns of MgCl₂ and MgCl₂/DIBP films (annealed and non-annealed) were compared (Figure 4.4).
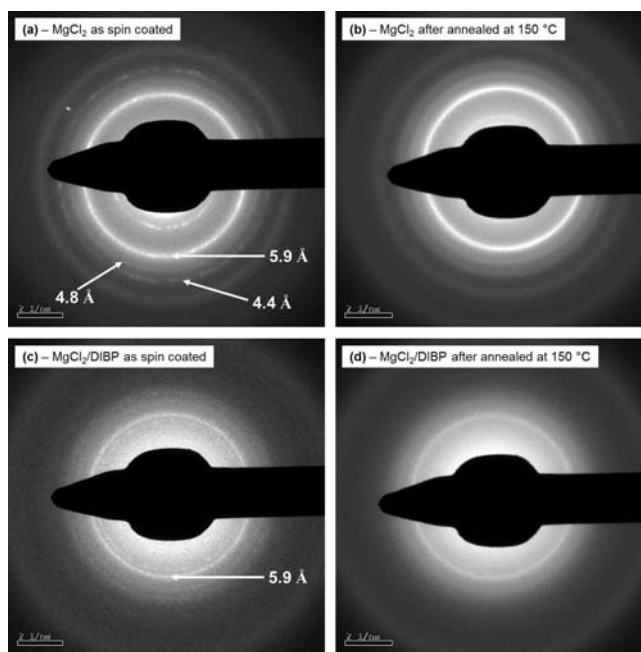
85

**Figure 4.4.** *Electron diffraction patterns of MgCl$_2$ and MgCl$_2$/DIBP films: (a) MgCl$_2$ film at 30 °C. (b) MgCl$_2$ film after annealing at 150 °C for 1h. (c) MgCl$_2$/DIBP film at 30 °C. (d) MgCl$_2$/DIBP film after annealing at 150 °C for 1h. In all figures, the intense signal (at d spacing of 5.9 Å) represents the basal plane of MgCl$_2$.*

The most intense signal in the diffraction pattern of all these films corresponds to a 'd spacing' of 5.9 Å, which represent the basal (001) plane of MgCl$_2$.[18,60] This is diagnostic for the stacking of MgCl$_2$ structural layers (003 planes for the α modification, 001 planes for the β and γ modifications). The intensity of this signal in the diffraction pattern is related to the stacking order of MgCl$_2$ layers. From the diffraction pattern, it is clear that the stacking was more ordered in MgCl$_2$ films compared to the MgCl$_2$/DIBP films. In the diffraction pattern of non-annealed MgCl$_2$, two more signals were also observed at a 'd spacing' of 4.4 and 4.8 Å (Figure 4.4a). The signals at 4.8 and 4.4 Å correspond to MgO (overtones of signals at 2.2 and 2.4 Å), which was probably formed due to the action of the electron beam on residual ethanol and MgCl$_2$.

The TEM images reveal that MgCl$_2$ crystals are already present in the film at 30 °C itself. In the non-annealed films, the crystalline regions are small, both in the lateral dimensions of the MgCl$_2$ platelets as well as in the degree of stacking along the (001) direction. After annealing, we observe a more extensive stacking of the MgCl$_2$ crystals in both films. In the annealed, donor-free MgCl$_2$ film (Figure 4.4b), the platelets also grow in their lateral dimensions leading to large domains of slightly bent and twisted MgCl$_2$ platelets in parallel alignment. These observations demonstrate that the nanocrystalline MgCl$_2$ platelets reorganize and sinter upon heating. The annealed MgCl$_2$/DIBP film features comparatively smaller crystals, which leads to a smaller degree of platelet stacking as compared to the annealed MgCl$_2$ film. We attribute this effect to DIBP stabilizing the coordinatively unsaturated magnesium sites at the perimeter of MgCl$_2$ platelets. The lateral dimensions of the MgCl$_2$ crystals in the annealed DIBP/MgCl$_2$ film were around 4 – 8 nm.

## 4.3.2 *In-situ* coordination of DIBP onto MgCl$_2$/EtOH film

MgCl$_2$/EtOH solutions were spin coated and the films were transferred to the ATR cell, followed by annealing the film under Ar flow. DIBP was exposed to MgCl$_2$/EtOH films with different amounts of coadsorbed ethanol and monitored by *in-situ* ATR-FTIR. The amount of residual ethanol in the film was controlled by a pre-annealing process. Three different situations were compared; non-annealed, pre-annealed at 80 °C and pre-annealed at 150 °C. A comparison of ν(C=O) DIBP in the three different cases is shown in Figure 4.5.

As the DIBP in heptane flows into the ATR cell containing a non-annealed MgCl$_2$/EtOH film, a broad band around 1695 cm$^{-1}$ appeared. This band had a distinguishable shoulder around 1737 cm$^{-1}$. The ν(C=O) band of DIBP around 1737 cm$^{-1}$ can be attributed to the free (uncoordinated) DIBP. The intensity of the ν(C=O) band increases with time and saturates at some stage. At the same time intensity of ν(O-H) band decreases. When the heptane was flowed through the film, the free (or physisorbed) DIBP was washed away, in turn results in the disappearance of the shoulder at 1737 cm$^{-1}$. The final spectra after heptane flow showed a peak maxima around 1690 cm$^{-1}$. The FWHM of the band was around 50 cm$^{-1}$. The broadness of the band indicates the presence of more than one DIBP

surface species; either on different surfaces or on the same surfaces with different coordination modes. During the period of the experiment, the amount of ethanol in the film decreased from 12.5 mol% to 3.4 mol% w.r.t $MgCl_2$. The amount of adsorbed DIBP at the end of the experiment was 15 mol% w.r.t. $MgCl_2$ (which was less than the maximum amount of DIBP appeared in annealed $MgCl_2$/DIBP films, see **Chapter 3**). Series of ATR-FTIR spectra measured during the *in-situ* adsorption of DIBP on non-annealed $MgCl_2$/EtOH film is shown in Figure 4.5a.
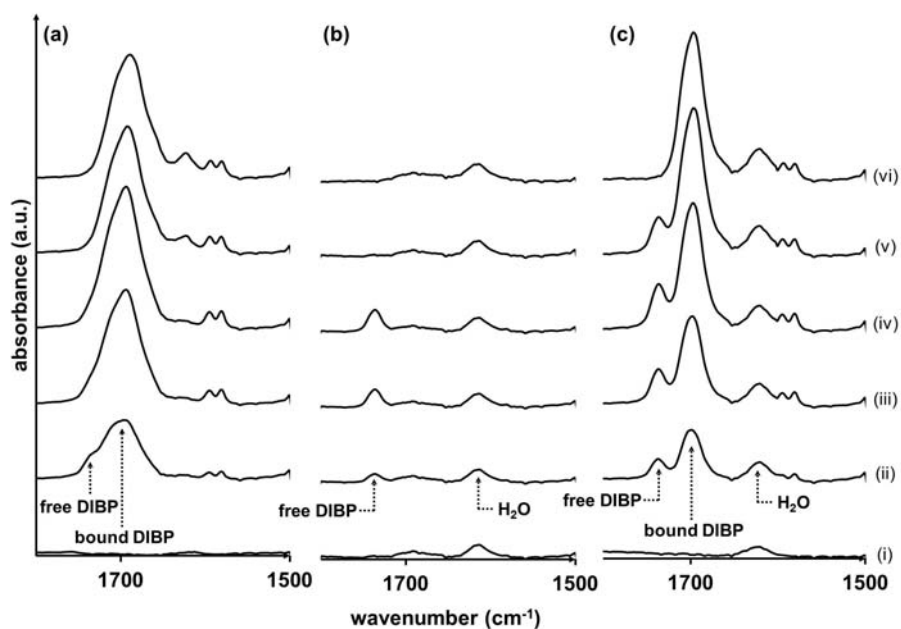


**Figure 4.5.** *Series (bottom to top) of ATR-FTIR spectra measured during attempts of in-situ adsorption of DIBP on (a) non-annealed MgCl₂/EtOH film. (b) completely annealed MgCl₂/EtOH film. (c) mild annealed MgCl₂/EtOH film. In all figures; (i) represent the film (post treated) at 30 °C, prior to DIBP dosing, (ii) to (iv) represent the film during DIBP/heptane flow, (v) and (vi) represent the film during heptane flow.*

When DIBP was exposed to completely annealed (at 150 °C for 1 hr, then cooled down to 30 °C) $MgCl_2$/EtOH film (ethanol content is less than 1 mol%), the band corresponding to DIBP in heptane was observed and disappeared during

heptane flow. However, the band of adsorbed DIBP did not show up. Series of ATR-FTIR spectra measured during attempts of *in-situ* adsorption of DIBP on ethanol-free MgCl$_2$ films are shown in Figure 4.5b. We noticed that DIBP did adsorb *in-situ* on non-annealed MgCl$_2$ films, even in the presence of water. Therefore, saturation of MgCl$_2$ sites by moisture is unlikely to be the reason for the inability of DIBP to be untaken onto annealed films. Our interpretation of these facts is that ethanol removal from spin coated MgCl$_2$/EtOH films in the absence of DIBP produces large MgCl$_2$ crystals with correspondingly low specific surface area; this would result into the low uptake of DIBP at a later stage (i.e., below the threshold of detectability of ATR-FTIR). TEM studies reported in the **Section 3.3.1** gave evidence for the formation of extended crystals. DFT calculations on the stability of MgCl$_2$ and MgCl$_2$ crystals saturated with small molecules such as ethanol and dimethyl ether was also in line with the results.[22,23,44] In fact, in the absence of small donors (in naked MgCl$_2$), the (104) surfaces are favoured, whereas in the presence of Lewis bases, smaller crystallites presenting (110) edges should be formed.[23] DFT calculations reported by Busico and coworkers predict a change in Gibbs energy during the process of ethanol adsorption; -23.7 kJ/mol for the adsorption of one molecule of ethanol on (104) surfaces whereas -80.0 kJ/mol were obtained free after the adsorption of two ethanol molecules on the four-fold Mg ion on (110) surfaces.[44]

As the ATR-FTIR studies discussed in **Chapter 3,** the changes in the IR envelope of ν(C=O)DIBP occur in the temperature range of 50 – 90 °C. The majority of ethanol is removed from the film at this range of temperature. When a MgCl$_2$/EtOH film pre-annealed at 80 °C for 15 min, the quantity of residual ethanol in the film reduced from 13 mol% to 5 mol% w.r.t Mg. The ATR cell was cooled down to room temperature, followed by introducing DIBP/heptane. As opposed to the ethanol free MgCl$_2$, DIBP binds to MgCl$_2$; and the sharp ν(C=O) envelope (FWHM of 33 cm$^{-1}$) is different from the broad envelope of DIBP on non-annealed MgCl$_2$/EtOH film. The peak positions of the final spectra are also different; 1700 cm$^{-1}$ instead of 1690 cm$^{-1}$. The amount of adsorbed DIBP at the end of the experiment was 13 mol% w.r.t. MgCl$_2$. The different stages of *in-situ* experiments are shown in Figure 4.5c. The peak position of DIBP carbonyl band (1700 cm$^{-1}$) remained almost same throughout the course of *in-situ* coordination of

DIBP and washing with heptane. The relatively sharp envelope of $\nu$(C=O)DIBP can be due to the predominant adsorption of DIBP on one type of surface site.

According to the $\nu$(C=O) DIBP values reported in literature (see Table 3.2), a band with peak maxima around 1700 cm$^{-1}$ represents a phthalate ester bound to (104) $MgCl_2$ surface sites. DFT predicts the formation of large $MgCl_2$ crystallites with (104) surfaces as the predominant lateral termination in the absence of adsorbate. On the other hand, in the presence of adsorbates, small crystallites of $MgCl_2$ with (110) as the predominant surface will be formed. TEM studies (discussed in the previous section) revealed the sintering of small $MgCl_2$ crystallites to large well-ordered $MgCl_2$ crystallites upon the removal of ethanol. These observations would indicate that ethanol desorption from a donor-free $MgCl_2$ film results in the reconstruction of $MgCl_2$ (110) sites to $MgCl_2$ (104).

### 4.3.3 *In-situ* coordination of EB onto MgCl$_2$/EtOH film

Ethyl benzoate (EB) belongs to the first family of donors used in Ziegler-Natta catalysis, and one of the simplest ester type donor. Replacing DIBP with ethyl benzoate (EB) can minimize the complexity of IR signatures due to the fact that the donor contains only a single donor atom hence the monodentate coordination on $MgCl_2$ sites is the unique possible way of binding. As a bidentate ligand (assuming that donor to Mg binding is via carbonyl oxygen), DIBP can have at least two different coordination modes on each type of $MgCl_2$ surface sites; monodenate and bridge on (104) and monodentate and chelate on (110). As discussed in the case of DIBP (**Chapter 3**), we made an attempt to make a co-impregnated $MgCl_2$/EB film. Even at 1:1 mol ratio of EB w.r.t. $MgCl_2$, EB signals were not seen in the ATR spectra of $MgCl_2$/EB film.

Compared to DIBP, the boiling point of EB is low. Despite the fact that the boiling point of ethanol is much lower than that of EB; IR signals of ethanol is present in the spin coated films. This indicates that the coordinated molecules of the adsorbate (irrespective of boiling point) survive high speed spinning conditions of spin coating. As discussed in **Chapter 3**, DIBP remains uncoordinated in the ethanol rich $MgCl_2$/DIBP/EtOH film; and ethanol is believed to be bound to $MgCl_2$ at this stage. The absence of EB signals in the spectra of $MgCl_2$/EB film could be due to the evaporation of uncoordinated EB along with solvent at high

90

speed spinning conditions of spin coating. With this method, we cannot compare the stability of coordinated EB versus coordinated DIBP. It is essential to eliminate the effects due to the difference in boiling point.

We performed *in-situ* coordination of EB on the MgCl$_2$ film (similar method used for DIBP; discussed in the previous section). Since the donor is always under heptane flow, the effects due to the differences in boiling point can be minimized. Non-annealed MgCl$_2$ film (11.5 mol% of ethanol w.r.t. Mg) and pre-annealed (80 °C, 15 min, 5.5 mol% of ethanol w.r.t Mg) was exposed to EB solution in heptane. The different stages of *in-situ* coordination of EB on MgCl$_2$ are shown in Figure 4.6.
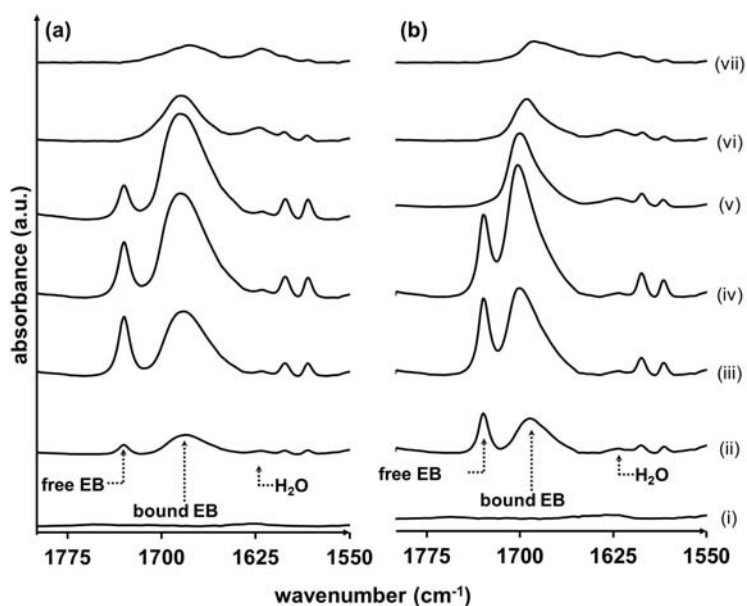


**Figure 4.6.** *Series (bottom to top) of ATR-FTIR spectra measured during attempts of in-situ adsorption of EB on (a) non-annealed MgCl$_2$/EtOH film. (b) mild annealed MgCl$_2$/EtOH film. In all figures; (i) represents the film (post treated) at 30 °C, prior to EB dosing, (ii) to (iv) represent the film during DIBP/heptane flow, (v) and (vii) represent the film during heptane flow.*

In the former case, we observed two distinctive carbonyl bands of EB around 1730 cm$^{-1}$ and 1685 cm$^{-1}$; representing uncoordinated and coordinated EB respectively. In the latter case, the uncoordinated EB appeared on the same position. However, the band of coordinated EB appeared at 1700 cm$^{-1}$. A similar trend was observed in the case of pre-annealed MgCl$_2$/DIBP films too. The carbonyl bands of coordinated EB are relatively sharper than that of analogous DIBP carbonyl bands (FWHM of 40 cm$^{-1}$ and 27 cm$^{-1}$ instead of 50 cm$^{-1}$ and 33 cm$^{-1}$). This could be due to unique coordination behaviour (monodentate) of EB, in comparison with the monodentate and bidentate coordination possibilities of DIBP.

Upon heptane flow, the band corresponding to uncoordinated EB disappeared. Even before complete elimination of uncoordinated donor, the band of coordinated EB also starts to diminish. Before completing the heptane flow, the band corresponding to bound EB was almost disappeared. This indicates the weaker adsorption of EB on MgCl$_2$, in comparison with DIBP adsorption on MgCl$_2$. In the case of pre-annealed MgCl$_2$/EB film, the peak position of bound EB was shifted from 1700 cm$^{-1}$ to 1694 cm$^{-1}$ along with the decrease in peak intensity. In non-annealed MgCl$_2$/EB film, the band of bound EB shifted from 1685 cm$^{-1}$ to 1677 cm$^{-1}$.

As explained in **Section 4.3.3**, reconstruction of MgCl$_2$ (110) sites to MgCl$_2$ (104) sites occurs during annealing. On a pre-annealed MgCl$_2$ film, the relative abundance of MgCl$_2$ (110) should be lower due to the surface reconstruction. The difference in the peak maxima of bound EB on mild-annealed ($\sim$ 1700 cm$^{-1}$) and non-annealed ($\sim$ 1685 cm$^{-1}$) films can be explained by the difference in the relative proportion of EB on MgCl$_2$ (104) and (110). Under heptane flow, EB removes relatively easier from less acidic (104) surface sites in comparison with (110) sites. This in turn, increase the relative ratio of EB distributed on MgCl$_2$ (110) sites [compared to EB on (104) sites]. This might be the reason for the shift in peak maxima of bound EB to lower wavenumber. Since, we were not able to calibrate the EB signals either by ATR-FTIR (IR signals of ethyl benzoate were missing in the co-impregnated MgCl$_2$/EB films) or XPS (F1s signal of 4-fluoro ethyl benzoate was the co-impregnated MgCl$_2$/FEB films) we will not comment on the amount of EB in the film.

If the coordination of both donors is via the monodentate mode, EB should bind stronger than DIBP. Since, the steric and electronic environments near the carbonyl band of EB makes it much stronger Lewis base than that of DIBP. However, *in-situ* experiments showed that DIBP binds stronger than EB. This strongly suggests that the DIBP coordination mode in the complexes with Mg is in a bidentate fashion (either in bridge or chelate mode).

If EB binds to Mg using carbonyl and ether oxygen, EB can also be a bidentate ligand. Chien and coworkers asserted that possibility.[61] Combined Solid state Nuclear Magnetic Resonance (NMR) and IR studies supported the bidentate coordination of EB using both carbonyl and ether oxygen. They observed two new bands at 1327 cm$^{-1}$ and 1305 cm$^{-1}$ in the IR spectra of MgCl$_2$/EB complexes, whereas in the neat EB these bands were 1279 cm$^{-1}$ and 1109 cm$^{-1}$. They attributed these bands to α-C-O bands in complexes. Ferreira and Damiani proposed it in a different way; the two new bands are generated by two different forms of the surface complex (monodentate and bidentate), whereas the band originally placed at 1280 cm$^{-1}$.[62]

On the other hand, Bache and coworkers proposed EB binds to Mg only through the carbonyl group.[63,64] That was based on the similarity in the shifts of TiCl$_4$/EB and MgCl$_2$/EB complexes. In TiCl$_4$/EB complexes, ether oxygen does not involve in bonding. Furthermore, they observed only one Mg-O stretch band (from carbonyl oxygen). If ether oxygen participates in complex formation, one more Mg-O band should appear at a lower frequency.

These authors explained the appearance of the IR bands at 1327 and 1305 cm$^{-1}$ in a completely different way. The upshift of ν(C-O) vibration from 1270 cm$^{-1}$ in neat EB to 1327 cm$^{-1}$ using the Scheme 4.1. The scheme shows the resonance hybridization of neat and complexed EB to a Mg$^{2+}$ ion. The contributions from the right hand hybrids give rise in general to a strengthening of the α-C-O band, a more nucleophilic character of carbonyl oxygen and a more electrophilic character of ether oxygen. Complexation of metal ion to the carbonyl oxygen will increase the contribution from the right hand hybrid, hence increasing the double bond character of the α-C-O band, results in the increase of stretching frequency from 1270 cm$^{-1}$ to 1327 cm$^{-1}$.
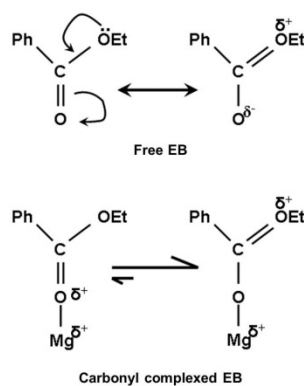
**Scheme 4.1.** *Resonance stabilization of free EB and carbonyl complexed EB in stoichiometric complexes or surface species.*

On the other hand, the upshift of the other α-C-O band from 1110 cm$^{-1}$ in neat EB to 1305 cm$^{-1}$ was due to the difference in the coupling with other skeletal modes. In neat EB, $\nu$(C-O) band at 1279 cm$^{-1}$ mode couples with the $\nu$(C-O) band at 1110 cm$^{-1}$. In the complex, the $\nu$(C-O) band at 1279 cm$^{-1}$ couples with the phenyl stretch mode at 1314 cm$^{-1}$. Therefore, in the neat EB $\nu$(C-O) band at 1110 cm$^{-1}$ is strong and phenyl stretching mode is weak (1314 cm$^{-1}$). On the other hand, in the complex, the intensities are opposite.

All these shifts are demonstrated in the ATR spectra of neat EB and EB bound to MgCl$_2$ (Figure 4.7). The aforementioned bands were appeared at 1328 cm$^{-1}$, 1307 cm$^{-1}$, 1270 cm$^{-1}$, 1107 cm$^{-1}$ and 1313 cm$^{-1}$ in our experimental spectra. So, the net effect of carbonyl complexation will be a weakening of the $\nu$(C=O) bond and a strengthening of the $\nu$(C-O) compared to free donor. This causes a negative and positive shift for the frequency of the former and the latter band respectively. A similar trend was observed for MgCl$_2$/DIBP complex too. An ethanol free MgCl$_2$/DIBP co-impregnated film is compared with free DIBP in Figure 4.8.
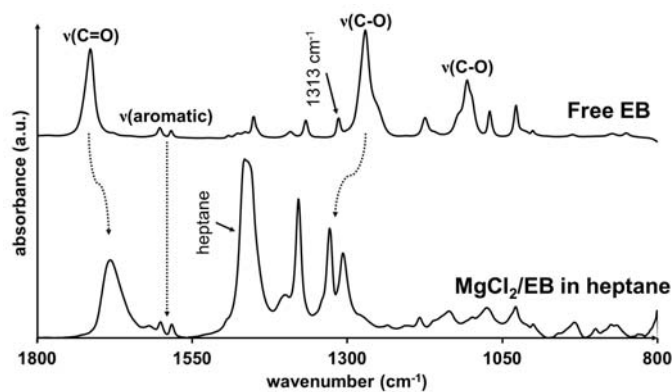
**Figure 4.7.** *Comparative IR spectra of free EB (top) and EB bound on mild annealed MgCl₂ in a heptane environment (bottom).*
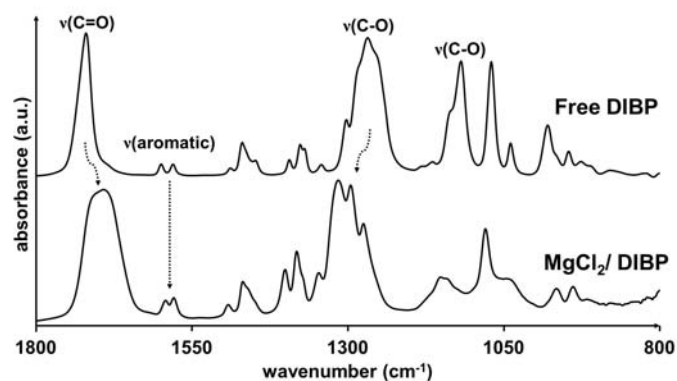


**Figure 4.8.** *Comparative IR spectra of free DIBP (top) and DIBP in annealed MgCl₂/DIBP film (bottom).*

## 4.3.4 ATR-FTIR studies on MgCl₂/BMMF/EtOH films

The chelating ability, the suitable conformation to give a distance between the oxygen atoms in the range 2.5-3.3 Å, and the capability to bind with MgCl₂ even in the presence of TiCl₄ and AlEt₃, makes diethers as the ideal donors for Ziegler-Natta catalysis. Uncoordinated BMMF shows a strong band of C-O stretching frequency around 1100 cm⁻¹ and shift to lower wavenumber upon coordination with Mg.[65] Figure 4.9 represents the MgCl₂/EtOH and MgCl₂/BMMF/EtOH films at 30 °C and 150 °C.
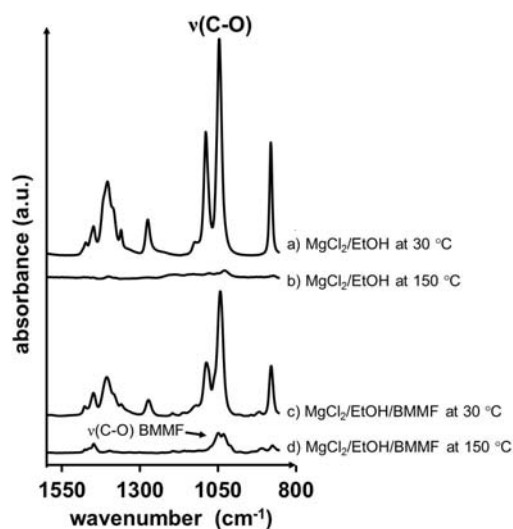
95

**Figure 4.9.** *ATR-FTIR spectra of (a) MgCl$_2$/EtOH at 30 °C, (b) MgCl$_2$/EtOH at 150 °C, (c) MgCl$_2$/EtOH/BMMF at 30 °C, (d) MgCl$_2$/EtOH/BMMF at 150 °C.*

At room temperature, the ν(C-O) band of BMMF in MgCl$_2$/EtOH/BMMF film is masked by intense ν(C-O) bands of ethanol (which appears in the same region, 1088 cm$^{-1}$ to 1040 cm$^{-1}$). At this stage, the only distinguishable band of BMMF is the in plane C-C-C and C-C-H bending motions of the aromatic rings that appear around 1192 cm$^{-1}$(1200 cm$^{-1}$in literature).[65] Compared to the intensities of the ethanol bands, it is very weak.

However, the ethanol free (annealed) spectra of MgCl$_2$/BMMF film clearly shows that the ν(C-O) band of BMMF appeared as a twin peak at 1050 cm$^{-1}$ and 1039 cm$^{-1}$ respectively. The integrated area of ATR-FTIR signals for the ν(C-O) twin bands are linearly proportional to the concentration of BMMF in the spin coating solution (Figure 4.10).
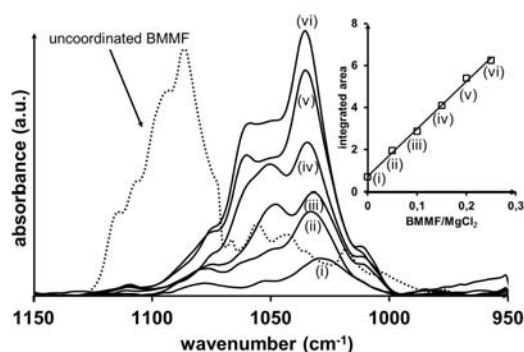
**Figure 4.10.** *ν(C-O) band of BMMF in MgCl₂/BMMF films after annealing at 150 °C (uncoordinated BMMF is shown in dotted lines). Plot of the ν(C-O) integrated intensities versus the BMMF/Mg ratio in ethanol solution prior to spin coating is shown as inset.*

### 4.3.5 *In-situ* coordination of DIBP and EB on MgCl₂/BMMF film

Based on DFT and experimental studies, it is generally believed that diether donors exclusively bind on MgCl₂ (110) sites.[18,43] In other words, the formation of MgCl₂ crystals from MgCl₂.EtOH adducts in the presence of BMMF leads to the preferential formation of MgCl₂ (110) sites.[21] By complete annealing (150 °C, 1 h) of a MgCl₂/EtOH/BMMF (BMMF to Mg ratio 0.20) film, we prepared a MgCl₂/BMMF film. Since the ethanol was removed from the film in the presence of BMMF, the MgCl₂ crystal should be having (110) sites as the preferred lateral terminations. The film was then exposed to DIBP/heptane flow. In the beginning, the ν(C=O) band of uncoordinated DIBP appeared around 1737 cm⁻¹. Subsequently, a new sharp band around 1690 cm⁻¹ appeared. The band representing uncoordinated DIBP was disappeared under heptane flow, but the new band remained unchanged. The intensity of the DIBP band was very weak compared to the band of *in-situ* coordinated DIBP on non-annealed MgCl₂/EtOH films. Amount of DIBP in the film was around 5 mol% w.r.t. MgCl₂. A decrease in the intensity of the BMMF ν(C-O) band is observed. This indicates that a small amount of DIBP could bind to MgCl₂ surface by replacing some of the BMMF donor. The sharpness of ν(C=O) band (FWHM of 25 cm⁻¹) can be explained as the exclusive coordination of DIBP on to MgCl₂ (110). Figure 4.11a represents the series of

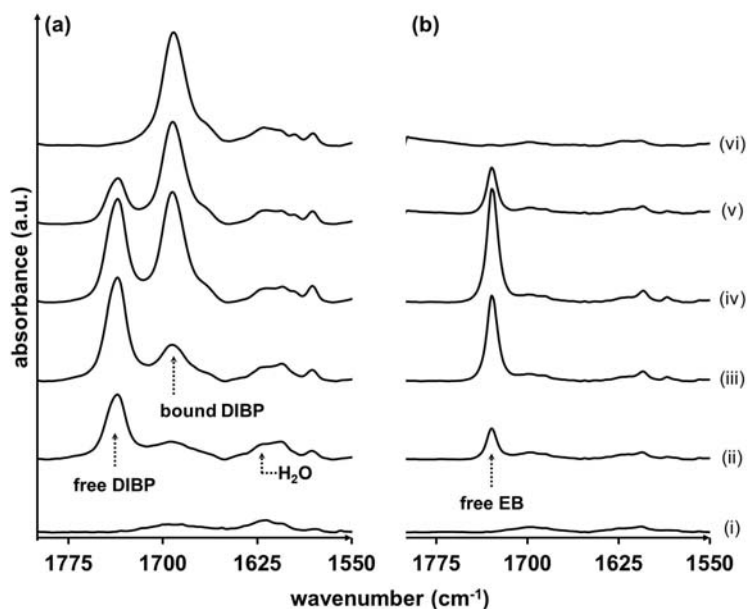spectra measured during the attempts of *in-situ* adsorption of DIBP on MgCl$_2$/BMMF films.



**Figure 4.11.** *Series (bottom to top) of ATR-FTIR spectra measured during attempts of in-situ adsorption of (a) DIBP on an ethanol-free MgCl$_2$/BMMF film. (b) EB on an ethanol-free MgCl$_2$/BMMF film. In all figures; (i) represents the MgCl$_2$/EtOH/BMMF film (after annealing at 150 °C for 1h) at 30 °C, prior to EB dosing, (ii) to (iv) represent the film during DIBP or EB in heptane flow, (v) and (vii) represent the film during heptane flow. BMMF to Mg ratio in the spin coating solution was 0.2.*

The same experiment was performed with EB instead of DIBP. In this case, we did not observe the *in-situ* coordination of EB on MgCl$_2$ surface. While purging the EB/heptane solution, the band of uncoordinated EB appears; which disappeared under heptane flow. As opposed to the case of MgCl$_2$/EtOH films, $\nu$(C=O) band of bound EB did not appear. This once again confirms that the coordination modes of EB is different from DIBP. As bidentate ligand, DIBP was able to replace trace amounts of BMMF which is also a bidentate ligand. On the other hand, replacing a

98

bidentate donor (BMMF) with a monodentate donor was not energetically favourable. As like DIBP, BMMF also stabilize the $MgCl_2$ surface sites and thereby prevent the sintering of crystallites at high temperature. Figure 4.11b represents the series of spectra measured during the attempts of *in-situ* adsorption of EB on $MgCl_2$/BMMF films.

## 4.3.6 Competitive adsorption of BMMF and DIBP onto $MgCl_2$/EtOH film

In the previous section, we demonstrated the exchange of BMMF donor with DIBP. Since the ν(C-O) band of BMMF is completely masked by ethanol at room temperature, it is difficult to monitor *in-situ* coordination of BMMF on $MgCl_2$/EtOH. We designed an experiment to monitor the competitive adsorption of BMMF and DIBP on to non-annealed $MgCl_2$/EtOH film. Figure 4.12 represents the series of spectra measured during *in-situ* adsorption of DIBP and BMMF on $MgCl_2$/EtOH film.



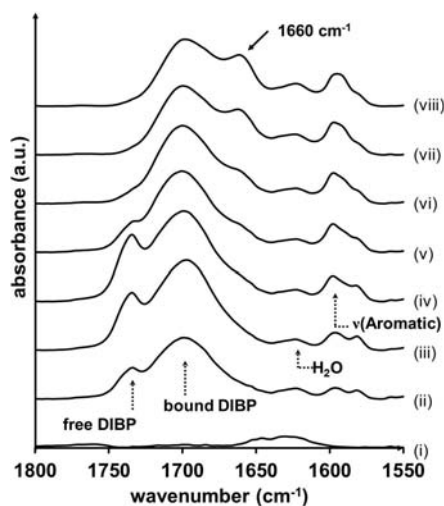**Figure 4.12.** *Series (bottom to top) of ATR-FTIR spectra measured during in-situ adsorption of DIBP and BMMF on a MgCl₂/EtOH film. (i) represents the non-annealed MgCl₂/EtOH film, (ii) to (v) represent the film during DIBP/BMMF in heptane flow, (vi) and (viii) represent the film during heptane flow. The BMMF to Mg ratio in the spin coating solution was 0.2.*

20μL/mL solution of DIBP and BMMF in heptane, was purged through the ATR cell. As expected, carbonyl bands of free and bound DIBP (a broad band with peak maxima around 1700 cm$^{-1}$) appeared. The free DIBP and excess BMMF was washed away under heptane stream. Meanwhile, a new shoulder around 1660 cm$^{-1}$ developed with the band of bound DIBP. The concentration of DIBP in the film was around 7 mol% wr.t. $MgCl_2$. The symmetric twin bands of an aromatic ring mode become asymmetric and intensified along with the formation of a 1660 cm$^{-1}$ band.

## 4.3.7 Periodic DFT-D model of DMP on $MgCl_2$ (104) and (110)

By means of periodic DFT-D, the chemisorption of the dimethyl homologue of DIBP (DMP) on $MgCl_2$ (104) and $MgCl_2$ (110) surfaces was modeled. Several factors were considered before building the model.

- **Coordination mode**: For donors containing only single donor atom this is trivial. Donors with two donor atoms like phthalates could bind in a monodentate, chelate-bidentate or bridge-bidentate fashion. Cavallo and coworkers[18] and Zakharov and coworkers[41] have suggested the formation of "zipped" models (bridged-bidentate spanning different $MgCl_2$ layers) or of bridged phthalates on (110) surface which was not considered here (for details, see following paragraphs in this section). For monodentate ligands binding to (110) surface, one could also envision coordination of two donor molecules to a single surface Mg.

- **Coverage**: The maximum degree of coverage, $\theta = 1.0$ as the one having every exposed Mg atom coordinated the same way by one donor molecule thus achieving the completeness in the coordination sphere. At lower coverage, coordinated Mg atoms are separated from each other by non-coordinated ones. Simulating lower coverage is expensive because it requires the use of much larger unit cells. Obviously the quantitative evaluations of free energies are affected by an error depending also on the selected approach and the peculiarity of adopted density functional. However, a certain number of reliable models of adsorption were identified (on the basis of both thermodynamics and plausible infrared spectra coming out of the proposed models).

**Adsorption of DMP on MgCl$_2$ (104)**: For the MgCl$_2$ (104) surface, a stable 'bridge' mode, with the two ester carbonyls bound to adjacent Mg, only at $\theta$ = 2/3, was obtained (Figure 4.13a). At full coverage, the bridge mode is not stable due to the interaction between neighbouring adsorbate molecules.

**Table 4.1.** *Dimethyl phthalate (DMP) adsorption energy ($\Delta E_{ads}$) to MgCl$_2$ cuts for different ways of binding at maximum degree of coverage (B3LYP-(D2)/TZVP, VTZp Ahlrichs level of computation) achievable for each binding type.*

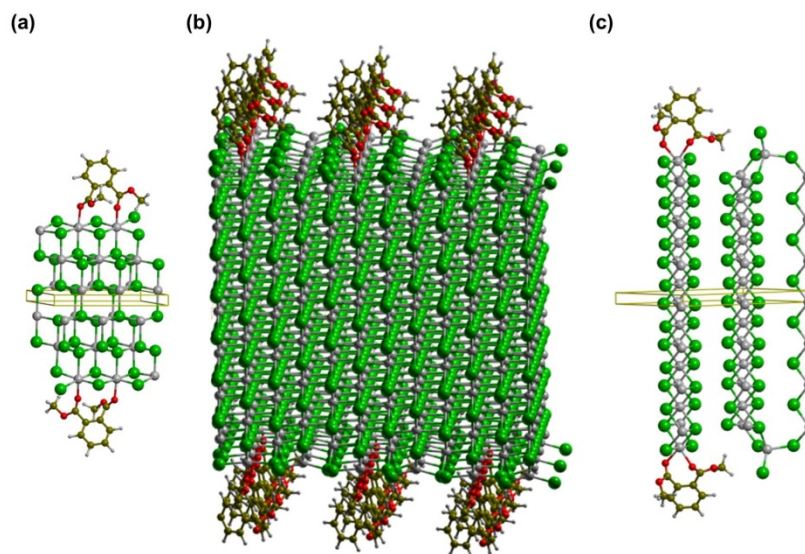| Surface (hkl) | Binding mode | Coverage ($\theta$) | $\Delta E_{ads}$(kJ/mol) |
|---|---|---|---|
| (104) | Bridge | 2/3 | -118.9 |
| (110) | Monodentate | 1/2 | -57.8 |
| (110) | Chelate | 1/2 | -79.5 |
| (110)/(001) | Monodenate | 1/2 | -60.6 |
| (110)/(001) | Chelate | 1/2 | -128.7 |



**Figure 4.13.** *Models of (a) dimethyl phthalate adsorbed on MgCl$_2$ (104) surface in 'bridge' mode, at optimum coverage of $\theta$ = 2/3.*

*(b)dimethyl phthalate adsorbed on MgCl₂ (110) surface in 'monodentate' mode, at optimum coverage of θ = 1/2. (c) dimethyl phthalate adsorbed on MgCl₂ (110) surface in 'chelate' mode, at optimum coverage of θ = 1/2; along with the surface reconstruction.*

**Adsorption of DMP on MgCl$_2$ (110)**: On MgCl$_2$ (110), the only reasonable coordination modes are chelate and monodentate. For the sake of completeness, feasibility of bridged and "zipped" binding modes on (110) were checked. Both of these ways turned out to be unstable, presumably because the spacing between the hypothetical binding Mg sites is too large. A previous Molecular Dynamics study by Boero and coworkers arrived at similar conclusions.[66]

While small donors adsorb normally on both surfaces even at full coverage, full coverage by phthalate was found to be not favourable. At full coverage, even with the minimal model, dimethyl phthalate chelate coordination is unfavourable. Steric hindrance between donor molecules, and between the donor and neighbouring MgCl$_2$ layers, results in spontaneous rearrangement to monodentate binding (Figure 4.13b). Because of the bulkier isobutyl ester moiety instead of the methyl ester moiety, the instability of chelate mode will be more pronounced for the industrially used DIBP. This result appears to conflict with decades of literature claims for DIBP,[67] but agrees with the Boero and coworker's Molecular Dynamics study.[66] When θ is lowered to 1/2, the chelate structure appears to be more stable, but considerable surface reconstruction occurs due to the interaction of bound DMP with neighbouring MgCl$_2$ layers (Figure 4.13c). A monodentate binding with θ equal to 1/2 has also been modeled and results are reasonable.

About the monodentate adsorption on (110) surface it is important to note that Becke-based exchange functionals tend to be more repulsive than those based on Perdew's exchange,[68] hence while B3LYP performs well in the calculation of vibrational frequencies (necessary for accurate thermal corrections), it tends to produce (much) lower adsorption and complexation energies than many other functionals. For example, in preliminary tests, the PBEO functional yields $\Delta E_{ads}$ values about 6-8 kcal/mol larger than B3LYP. Therefore, the use of other functionals would further lower the Gibbs free energy in particular in the case of monodentate binding, moreover that adsorption would be favored further by a

coadsorption with ethanol present in high quantities in spin coated samples.

However, it remains also possible that coordination to (110) at lower coverage, or on a 'rougher' surface or defective positions would also result in strong binding. As reported in the literature and also revealed by the TEM measures, presence of ethanol during the formation of MgCl$_2$ crystallites leads to small crystallites with MgCl$_2$ (110) as the preferred lateral surface termination. In that crystallites, the regular stacking is also easily lost.

Hence, together with perfect flat surfaces, the adsorption process on defective positions like the edges was also modeled (by the same periodic DFT approach). The adsorption on DMP as a chelate phthalate on the edge between the (110) surface exposing four-fold Mg atoms and the most abundant (001) surface (basal) has been modeled. That species can be indicated as the (110)/(001) chelate; that is a DMP bidentate molecule on a protruding (110) layer (Figure 4.14).
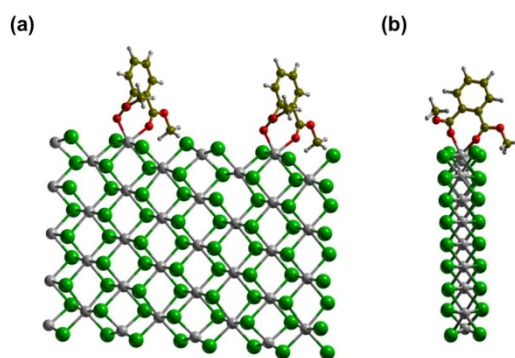


**Figure 4.14.** *Models of dimethyl phthalate adsorbed on the edge between MgCl$_2$ (110) surface and MgCl$_2$ basal (001) surface, in 'chelate' mode, at optimum coverage of θ = 1/2.*

The contemporary presence of a bridge DMP on MgCl$_2$ (104) with θ = 2/3, chelate DMP on (110)/(001) edge (θ = 1/2) and a small amount of monodentate DMP on MgCl$_2$ (110) surface with θ = 1/2 (maybe also in coadsoprtion with ethanol molecules) emerging from the modelling methodologies are compatible with IR experiments.

The vibrational analysis of DMP in the gas phase was performed. Obviously DMP is present as physisorbed molecule, but the variation in stretching frequency

from the gas phase to 'uncoordinated'/'physisorbed to the basal plane' is expected to be almost negligible. The predictions are within the harmonic approximation, and a further improvement would be gained when anharmonic correction is also applied.

## 4.4 Summary

TEM studies showed that sintering of $MgCl_2$ films occurs during annealing. In the absence of a donor, this sintering leads to very large $MgCl_2$ platelets that offer only a very small number of coordination sites. ATR-FTIR studies supported this observation; adsorption of DIBP does not occur on the annealed (ethanol free) $MgCl_2$ films. Preferential formation of $MgCl_2$ (104) in the absence of an electron donor and preferential formation of $MgCl_2$ (110) in the presence of an electron donor are predicted by computational studies. The relatively sharp carbonyl band of DIBP on ethanol-poor $MgCl_2$ can be explained as the preferential adsorption of DIBP on $MgCl_2$ (104) sites. Based on this, we propose a reconstruction of $MgCl_2$ (110) into $MgCl_2$ (104) upon removal of an electron donor (in this case, removal of ethanol by means of annealing).

It is well known that diether donors such as BMMF bind to $MgCl_2$ (110) edges only and induce the formation of $MgCl_2$ crystals with mostly (110) sites as lateral terminations. The symmetric and sharp carbonyl band observed during adsorption of DIBP on $MgCl_2$/BMMF film can be assigned to DIBP bound on the $MgCl_2$ (110) surface.

The significant differences in the coordination behaviour of DIBP and EB throughout the *in-situ* ATR-FTIR studies lead to the assumption that the preferential coordination mode of DIBP is bidentate: chelate on (110) and bridge on (104).

Periodic DFT-D simulations predicted the IR spectra corresponding to the different modes of DMP adsorption on $MgCl_2$ (104) and (110) surfaces. The DMP adsorption was energetically favourable when (i) binding on $MgCl_2$ (104) in bridge mode, (ii) binding on $MgCl_2$ (110)/(001) edge in chelate mode and (iii) binding on $MgCl_2$ (110) in monodenate mode. Chelated DMP on $MgCl_2$ (110) surface and monodentate DMP on $MgCl_2$ (110)/(001) edge were less favourable situations.

In summary, three distinctive ν(C=O) features of adsorbed DIBP can be distinguished by *in-situ* ATR-FTIR (at ~ 1700 cm$^{-1}$, ~ 1690 cm$^{-1}$ and ~ 1660 cm$^{-1}$). The most reasonable assignments for these three bands might be:

- ~1700 cm$^{-1}$ band represents ν(C=O)DIBP bound to MgCl$_2$ (104) in 'bridge' mode.

- ~1690 cm$^{-1}$ band represents ν(C=O)DIBP bound to MgCl$_2$ (110) in 'chelate' mode.

- ~1660 cm$^{-1}$ band represents ν(C=O)DIBP bound to MgCl$_2$ (110) in a 'monodentate' mode.According to DFT, the other carbonyl bond remains uncoordinated and gives another ν(C=O) signal at higher wavenumber (near to the uncoordinated DIBP signal).

The band of physisorbed DIBP ν(C=O) at ~ 1725 cm$^{-1}$ was reported in **Chapter 3**. The broad and complex ν(C=O) DIBP bands of co-impregnated MgCl$_2$/DIBP films (reported in **Chapter 3**) can be explained as the linear combination of the above-mentioned components. This will help us to understand the coordination behaviour of DIBP at different temperature. The relative distribution and stability of MgCl$_2$ surface sites in the presence / absence of donor (ethanol, DIBP) also can be found out.

## 4.5 References

(1) Chadwick, J. C.; Garoff, T.; Severn, J. R. *Tailor-Made Polymers via Immobilization of Alpha-Olefin Polymerization Catalysts;* Severn, J. R.; Chadwick, J. C., Eds.; WILEY-VCH: Weinheim, **2008,** Ch. 2.

(2) Seth, M.; Margl, P. M.; Ziegler, T. *Macromolecules* **2002,** *35,* 7815.

(3) Busico, V.; Corradini, P.; de Martino, L.; Proto, A.; Savino, V.; Albizzati, E. *Makromol. Chem.* **1985,** *186,* 1279.

(4) Albizzati, E.; Giannini, U.; Morini, G.; Smith, C. A.; Ziegler, R. C. In *Ziegler Catalysts: Recent Scientific Innovations and Technological Improvements;* Flink, G.; Mülhaupt, R.; Brintzinger, H. H., Eds.; Springer-Verlag: Berlin, **1995.**

(5) Soga, K.; Chen, S. I.; Ohnishi, R. *Polym. Bull.* **1982,** *8,* 473.

(6) Giannini, U. *Macromol. Chem. Suppl.* **1981,** *5,* 216.

(7) Zambelli, A.; Ammendola, P. *Prog. Polym. Sci.* **1991,** *16,* 203.

(8) Sacchi, M. C.; Tritto, I.; Locatelli, P. *Prog. Polym. Sci.* **1991,** *16,* 331.

(9) Chadwick, J. C.; Morini, G.; Balbontin, G.; Camurati, I.; Heere, J. J. R.; Mingozzi, I.; Testoni, F.*Macromol. Chem. Phys.* **2001,** *202,* 1995.

(10)   Busico, V.;  Cipullo, R.; Polzone, G.; Talarico, G.; Chadwick, J. C. *Macromolecules* **2003,** *36*, 2616.

(11)   Busico, V.; Chadwick, J. C.; Cipullo, R.; Ronca, S.; Talarico, G. *Macromolecules* **2004,** *37*, 7437.

(12)   Terano, M.; Kataoka, T.; Keii, T. *Macromol. Chem.* **1987,** *188,* 1477.

(13)   Busico, V.; Cipullo, R.; Monaco, G.; Talarico, M.; Vacatello, J. C.; Chadwick, J. C.; Segre, A. L.; Sudmeijer, O. *Macromolecules* **1999,** *32,* 4173.

(14)   Busico, V.; Causa, M.; Cipullo. R.; Credendino, R.; Cutillo, F.; Friederichs, N.; Lamanna, R.; Segre, A.; Castelli, V. V. A. *J. Phys. Chem. C* **2008,** *112*, 1081.

(15)   Credendino, R.; Busico, V.; Causa, M.; Barone, V.; Budzelaar, P. H. M.; Zicovich-Wilsone, C. *Phys. Chem. Chem. Phys.* **2009,** *11,* 6525.

(16)   Boero, M.; Parrinello, M.; Terakura, K. *J. Am. Chem. Soc.* **1998,** *120,* 2746.

(17)   Monaco, G.; Toto, M.; Guerra, G.; Cavallo, L. *Macromolecules* **2000,** *33,* 8953.

(18)   Correa, A.; Piemontesi, F.; Morini, G.; Cavallo. L. *Macromolecules* **2007,** *40,* 9181.

(19)   Brambilla, L.; Zerbi, G.; Piementosi, F.; Nascetti, S.; Morini, G. *J. Mol. Catal. A: Chem.* **2007,** *263,* 103.

(20)   D'Amore, M.; Credendino, R.; Budzelaar, P.; Causa, M.; Busico, V. *J. Catal.* **2012,** *286,* 103.

(21)   Andoni, A.; Chadwick, J. C.; Niemantsverdriet, J. W. (Hans).; Thüne, P. C. *J. Catal..* **2008,** *257,* 81.

(22)   Turunen, A.; Linnolahti, M.; Karttunen, V, A.; Pakkanen, T, A.; Denifl, P.; Leinonen, T. *J. Mol. Catal. A: Chem.* **2011,** *334,* 103.

(23)   Credendino, R.; Pater, J. T. M.; Correa, A.; Morini, G.; Cavallo, L. *J.Phys. Chem. C* **2011,** *115,* 13322.

(24)   Correa, A.; Credendino, R.; Pater, J. T. M.; Morini, G.; Cavallo, L. *Macromolecules* **2012,** *45* (9), 3695.

(25)   Taniike, T.; Terano, M. *J. Catal.* **2012,** *293,* 39.

(26)   Vanka, K.; Singh, G.; Iyer, D.; Gupta, V. K. *J. Phys. Chem. C* **2010,** *114* (37), 15771.

(27)   Socrates, G. C. *Infrared and raman Charecteristic Group Frequencies. Tables and Charts,* 3$^{rd}$ Ed.; John Wiley & Sons: Canada, **2001.**

(28)   Duncan, A. B. F.; Gordy, W.; Jones, R. N.; Matsen, F. A.; Sandorfy, C.; West, W. *Chemical Application of Spectroscopy;* Interscience Publisher, Inc.: New York, **1956.**

(29)   Wilson, E. B.; Decius, J. C.; Cross, C. P.*Molecular Vibrations: The Theory of Infrared and Raman Vibrational Spectra;* Dover Publications, **1980.**

(30)   Gordon, D.; Wallbridge, M. G. M. *Inorg. Chim. Acta.* **1984,** *88*, 15.

(31)   Zohuri, G.; Ahmadjo, S.; Jamjah, R.; Nekoomanesh, M. *Iran. Polym. J.* **2001,** *10* (3), 149.

(32)   Andoni, A.; Chadwick, J. C.; Niemantsverdriet, J. W. (Hans).; Thüne, P. C. *Catal. Lett.* **2009,** *130,* 278.

(33)   Arzoumanidis, G. G.; Karayannis, N. M. *Appl. Catal.* **1991,** *76*, 221.

(34)   Song, W. D.; Chu, K. J.; Chang, H, S.; Ihm, S, K. *J. Mol. Catal.* **1993,** *84,* 109.

(35)   Yang, C. B.; Hsu, C. C.; Park, Y. S.; Shurvell, H. F. *Eur. Polym. J.* **1994,** *30* (2), 205.

(36)   Ystenes, M.; Bache, Ǿ.; Bade, O. M.; Blom, R.; Eliertsen, J. L.; Nirisen, Ǿ.; Ott, M.; Svendsen, K.; Rytter, E. In *Future technology for Polyolefin and Olefin Polymerization catalysis;* Terano, M.; Shiono, T., Eds.; Technology and education Publishers: Tokyo, **2002,** 184.

106

(37)   Makwana, U.; Naik, D. G.; Singh, G.; Patel, V.; Patil, H. R.; Gupta, V. K. *Catal. Lett.* **2009,** *131* (3-4), 624.

(38)   Singh, G.; Kaur, S.; Makwana, U.; Patankar, R. B.; Gupta, V. K. *Macromol. Chem. Phys.* **2009,** *210* (1), 69.

(39)   Kissin, Y. V.; Liu, X. S.; Pollick, D. J.; Brungard, N. L.; Chang, M. *J. Mol. Catal. A: Chem.* **2008,** *287* (1-2), 45.

(40)   Potapov, A. G.; Bukatov, G. D.; Zakharov, V. A. *J. Mol. Catal. A: Chem.* **2006,** *246* (1-2), 248.

(41)   Stukalov, D. V.; Zakharov, V. A.; Potapov, A. G.; Bukatov, G. D. *J. Catal.* **2009,** *266* (1)*,* 39.

(42)   Potapov, A. G.; Bukatov. G. D.; Zakharov. V. A. *J. Mol. Catal. A: Chem.* **2010,** *316* (3-4), 95.

(43)   Potapov, A. G.; Politanskaya, L. V. *J. Mol. Catal. A: Chem.* **2013,** *368*, 159.

(44)   Capone, F.; Rongo, L.; D'Amore, M.; Budzelaar, P. H. M.; Busico, V. *J. Phys. Chem. C.* **2013,** http://pubs.acs.org/doi/abs/10.1021/jp406977h.

(45)   Moodley, P.; Loos, J.; Niemantsverdriet, J. W. (Hans).; Thüne, P. C. *Carbon.* **2009,** *47*, 2002.

(46)   Moodley, P.; Scheijen, F. J. E.; Niemantsverdriet, J. W. (Hans).; Thüne, P. C. *Catal. Today.* **2009,** *154* (1-2), 142.

(47)   Mannie, G. J. A.; van Deelen, J.; Niemantsverdriet, J. W. (Hans).; Thüne, P. C. *Appl. Phys. Lett.* **2011,** *98*, 051907.

(48)   Dovesi, R.; Saunders, V. R.; Orlando, R.; Zicovich-Wilson, C. M.; Pascale, F.; Civalleri, B.; Doll, K.; Bush, I. J.; D'Arco, P.; Lunell, M. *Crystal 2009 User Manual;* Turin University: Italy.

(49)   Grimme, S. *J. Comput. Chem.* **2006,** *27*, 1787.

(50)   Civalleri, B.; Zicovich-Wilson, C. M.; Valenzano, L.; Ugliengo, P. *Cryst. Eng. Comm.* **2008,** *10*, 405.

(51)   Schäfer, A.; Horn, H.; Ahlrichs, R. *J. Chem. Phys.* **1992,** *97*, 2571.

(52)   Boys, S. F.; Bernardi, F. *Mol. Phys.* **1970,** *19*, 553.

(53)   Prencipe, M.; Pascale, F.; Zicovich-Wilson, C. M.; Saunders, V. R.; Orlando, R.; Dovesi, R. *Phys. Chem. Miner.* **2004,** *31*, 1.

(54)   Pascale, F.; Zicovich-Wilson, C. M.; Gejo, F. L.; Civalleri, B.; Orlando, R.; Dovesi, R. *J. Comput. Chem.* **2004,** *25*, 888.

(55)   Zicovich-Wilson, C. M.; Pascale, F.; Roetti, C.; Saunders, V. R.; Orlando, R.; Dovesi, R. *J. Comput. Chem.* **2004,** *25*, 1873.

(56)   Pascale, F.; Zicovich-Wilson, C. M.; Orlando, R.; Roetti, C.; Ugliengo, P.; Dovesi, R. *J. Phys. Chem. B.* **2005,** *109*, 6146.

(57)   Magni, E.; Somorjai, G. A. *J. Phys. Chem. B.* **1998,** *102*, 8788.

(58)   Kim, S. H.; Somorjai, G. A. *Surf. Interface. Anal.* **2001,** *31*, 701.

(59)   Kim, S. H.; Tewell, C. R.; Somorjai, G. A. *Korean. J. Chem. Eng.* **2002,** *19* (1), 1.

(60)   Oleshko, V. P.; Crozier, P. A.; Cantrell, R. D.; Westwood, A. D. *J. Electron. Microsc.* **2002,** *51(Supplement)*, S27-S39.

(61)   Chein, J. C. W.; Dickinson, L . C.; Vizzini, J. *J. Polym. Sci. A: Polym. Chem.* **1990,** *28,* 2321.

(62)   Ferreira, M.; Damiani, D. E. *J. Polym. Sci. A: Polym. Chem.* **1994,** *32,* 1137.

(63)   Bache, Ǿ.; Ystenes, M. *Appl. Spec.* **1994,** *48* (8), 985.

(64)  Bache, Ǿ. *The Chemistry of MgCl₂-supported Ziegler-Natta catalyst studied by in-situ infrared spectroscopy;* Ph. D Thesis., Institutt for uorganisk kjemi Norges Tekniske i Trondheim: Norway, **1994.**

(65)  Brambilla, L.; Zerbi, G.; Piementosi, F.; Nascetti, S.; Morini, G. *J. Phys. Chem.* **2010,** *114,* 11475.

(66)  Boero, M.; Parrinello, M.; Weiss, Hüffer, S. *J. Phys. Chem. A.* **2001,** *105,* 5096.

(67)  Correa, A.; Talarico, G.; Morini, G.; Cavallo, L. In *Current Achievements on Heterogenous Olefin Polymerization Catalysts;* Terano, M.Ed.; Nagoya, **2004,** 44.

(68)  Wu, X.; Vargas, M. C.; Nayak, S.; Lotrich, V.; Scoles, G. *J. Chem. Phys.* **2001,** *115,* 8747.

# 5

# Resolution and assignment of phthalate bands: a combined experimental and DFT study

# **Abstract**

*IR spectra of dimethyl phthalate adsorbed on various MgCl$_2$ surface sites were simulated by DFT-D. The relative peak positions of DMP carbonyl bands were compared with the carbonyl bands of various experimentally isolated MgCl$_2$/DIBP surface species. By reconciling the experimental IR spectra and DFT simulated IR spectra, an approach was developed to explain the surface chemistry of DIBP in the MgCl$_2$/EtOH/DIBP co-impregnated films. With respect to the changes in temperature and donor concentration, variation in the relative abundance of DIBP on different MgCl$_2$ surface sites were observed. Changes in the carbonyl envelope of DIBP were the after effects of MgCl$_2$ crystal surface reconstruction and reorganization of DIBP between different MgCl$_2$ surfaces. Presence of ethanol in the spin coated film result in the formation of very small corrugated MgCl$_2$ crystallites with MgCl$_2$ (110) as the lateral surface termination. DIBP remains uncoordinated in the ethanol rich MgCl$_2$ film. In the presence of DIBP, removal of residual ethanol from the (110) sites result in the replacement of vacancies by DIBP. Removal of residual ethanol from the film in the absence of any adsorbate will result in the reconstruction of (110) site to (104) site. Annealing of MgCl$_2$ film leads to the sintering of MgCl$_2$ crystallites, which significantly reduce the amount of surface sites and hence the adsorbed DIBP in the film. Ordering of MgCl$_2$ platelets reduces the abundance of (110)/(001) edges, result in the selective desorption of DIBP from that particular surface*

# 5.1 Introduction

**T**ypical formulations of a MgCl₂-supported Ziegler-Natta catalyst for ethylene polymerization include a solid pre-catalyst (TiCl₄ adsorbed on an 'activated' MgCl₂ matrix) and an Al-trialkyl activator (known as the cocatalyst). When it comes to the case of propylene (or higher α-olefins) polymerization, Lewis bases (known as electron donors) also become the essential part of the catalyst.[1,2] The selectivity of the catalyst was improved by the use of Lewis bases as additives, in the solid pre-catalyst (internal donor) and in the cocatalyst/monomer solution (external donor).[1,2] While Ziegler-Natta catalysts have evolved to become a highly active and selective olefin polymerization catalyst that is still monopolizing the worldwide production of polypropylene, the nature of the active site responsible for stereospecific polypropylene remains elusive.[3] It is generally believed that TiCl₄ and the internal donor are independently chemisorbed on MgCl₂ (110) and/or (104) lateral terminations of MgCl₂; followed by the reduction and alkylation of the TiCl₄ adsorbates. This creates the active site for polymerization. The adjacently bound internal or external donor molecules modulate the steric and electronic properties of the active sites.[2] These concepts however retain a vague and speculative character. An important reason for this uncertainty regarding the molecular level details of the catalyst is a lack of reliable spectroscopic information about the reactive surface.[4]

In recent years, two strategies have led to significant new insight on the molecular level structure of Ziegler-Natta catalyst. One is the experimental investigation of flat-model catalysts made via spin coating of MgCl₂ and internal donor solutions in EtOH on silica wafers, followed by treatment with TiCl₄ (with or without a previous step of Ostwald crystal ripening).[5-8] Using Ostwald ripening, spin coated support precursor MgCl₂.nEtOH can be converted to well-defined MgCl₂ crystallites large enough to facilitate morphological characterization by microscopic techniques such as SEM, and to identify polymer formation on the lateral faces of the crystallite. Andoni and coworkers reported the crystal growth of small MgCl₂.nEtOH crystallites in the MgCl₂/EtOH (donor free) films into large well-defined MgCl₂ crystallites with 120° and 90° edge angles.[7] The hexagonal structure (120° edge angle) indicates a preference for the formation of a particular

crystallite face i.e., (110) versus (104) or vice versa. Later, they found the formation of $MgCl_2$ crystallites with only 120° edge angle in the presence of diether donor, and both 120 ° and 90° edge angle in the presence of monoester and diester donor.[8] They found the polymerization activity was exclusively on these edges and suggested the formation of $MgCl_2$ (110) edges exclusively in the presence of diether; on the other hand, both $MgCl_2$ (104) and (110) in the presence of monoester and diester. SEM images (Figure 5.1) shows exclusive formation of polypropylene on the edges of $MgCl_2$ crystallites and the relative proportion of 90 ° and 120 ° edge angles are dependent on the internal donor present in the film during the Ostwald ripening.[8]
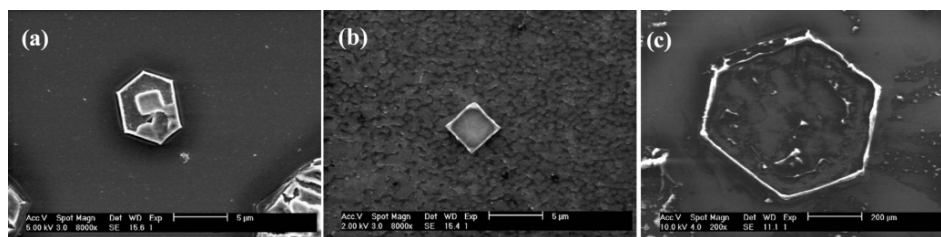


**Figure 5.1.** *(a) SEM images of polypropylene on the edges of $MgCl_2$ crystal formed in the presence of DIBP; edge angles 120° and 90°. (b)SEM images of polypropylene on the edges of $MgCl_2$ crystal formed in the presence of DIBP; edge angle 90°. (c) SEM images of polypropylene on the edges of $MgCl_2$ crystal formed in the presence of BMMF; edge angle 120°.*[8]

The second approach, which made significant progress in finding out the molecular level structure of active sites, is computational modelling of $MgCl_2$/$TiCl_4$/internal donor bulk and surface structures by means of periodic Density Functional theory methods including dispersion (DFT-D). Recent DFT studies show that the well-formed $MgCl_2$ crystals in the absence of adsorbates predominantly feature $MgCl_2$ (104), but crystals formed in the presence of Lewis bases (especially small molecules such as methanol, dimethyl ether) should mainly expose $MgCl_2$ (110) terminations.[9-13]

In **Chapter 4**, we discussed the isolation of different DIBP/$MgCl_2$ species and the corresponding IR spectra. DFT-D simulations (performed by our

collaborators) provide the most probable surface structure for DIBP on MgCl$_2$ (104) and (110) sites. In this chapter, we present the results of the first investigation combining the two approaches. The relative wavenumbers of different DIBP/MgCl$_2$ species observed during experiments were compared with the DFT simulated IR spectra and assigned to the corresponding structure. Based on the information from DFT-D, experiments and literature, we derived a set of components to resolve the ν(C=O) envelope of DIBP. This DFT-experiment reconciled approach will help to understand MgCl$_2$/EtOH/DIBP catalyst precursor phases. Using this approach, we revisit all the important experimental spectra shown in **Chapter 3** and **4**; and explain the changes in the IR features as the changes in the relative distribution of DIBP on different surfaces and/or the changes in the coordination mode of DIBP.

## 5.2 DFT simulated wavenumbers of DMP surface species

Our collaborators calculated the symmetrical (s) and antisymmetrical (as) C=O stretching vibrations of chemisorbed dimethyl phthalate (DMP) using DFT-D. The binding site and binding mode of DMP (discussed in **Chapter 4.3.7**), corresponding ν(C=O) wavenumbers and intensities are shown in Table 5.1. The wavenumbers reported in Table 5.1 were not corrected for anharmonicity, neither for different alkyl group in the ester moiety. Just to add a further comment; it was found that, after the application of a 2$^{nd}$ order pertrubative anharmonic correction to DIBP molecule in the gas phase, the wavenumber values for the in-phase or out-of-phase C=O stretching vibrations decreased by ~30 cm$^{-1}$ upon going from harmonic to anharmonic. Therefore, changing the alkyl residue in the ester group and correcting for anharmonicity would achieve a reasonable agreement of the simulated data with experiment.

**Table 5.1.** *DFT-D predicted wavenumbers for DMP at different coordination sites and coordination modes.*

| Structure (B3LYP-D/TZVP, optVTZp Alrichs) | (C=O) stretching (after harmonic approximation) | |
|---|---|---|
| | wavenumber ($cm^{-1}$) | intensity (a.u.) |
| 'Free' DMP molecule | 1797 | 223 |
| (**gas phase**) | 1777 | 261 |
| | | |
| DMP bound to polymer edge | 1790 (dangling CO) | 376 |
| $MgCl_2$ (110)/(001) | 1698 (bound CO) | 579 |
| **monodentate mode** | | |
| | | |
| DMP bound to $MgCl_2$ (110) | 1761 (dangling CO) | 1015 |
| **monodentate mode** ($\theta = 1/2$) | 1720 (bound CO) | 284 |
| | 1703 (bound CO) | 278 |
| | | |
| DMP bound to $MgCl_2$ (104) | 1764 | 1014 |
| **bridge mode** ($\theta = 2/3$) | 1728 | 545 |
| | | |
| DMP bound to polymer edge | 1748 | 870 |
| $MgCl_2$ (110)/(001) | 1711 | 248 |
| **chelate mode** | | |
| | | |
| DMP bound to $MgCl_2$ (110) | 1753 | 1025 |
| **chelate mode** ($\theta = 1/2$) | 1669 | 501 |

## 5.3 Implications for comparing DFT simulated spectra with experimental spectra

Few approximations and simplifications were made before integrating the DFT and experiment results.

1. In order to minimize the number of components used to fit the experimental spectra the two components of same DMP species are merged to a single component (only if the difference in peak maxima is less than 40 cm$^{-1}$). The new peak position is fixed at the center of gravity. For example, DFT assigned wavenumbers for the $\nu$(C=O) band of DMP chelated to polymer edge MgCl$_2$ (110)/(001) are at 1748 cm$^{-1}$ and 1711 cm$^{-1}$ with intensity of 870 and 248 respectively. As per center of gravity, the new position will be 1740 cm$^{-1}$. On the other hand, the DFT assigned wavenumbers of DMP bound to MgCl$_2$ (110) surface are at 1753 cm$^{-1}$ and 1669 cm$^{-1}$. Since these components are separated by 84 cm$^{-1}$, these components cannot merge. Table 5.2 represents the wavenumbers after simplification.

2. The relative wavenumbers – not the absolute wavenumbers – are used to compare with experimental spectra. As discussed in **Chapter 4, Section 4.3.5**, the sharp $\nu$(C=O) band (at 1690 cm$^{-1}$) of *in-situ* coordinated DIBP on annealed MgCl$_2$/BMMF film strongly designates the DIBP bound to MgCl$_2$ (110) in chelate mode (Figure 5.2a). The DFT simulated $\nu$(C=O) band of chelated DMP on MgCl$_2$ (110)/(001) at 1740 cm$^{-1}$ is the only chelate species which is comparable with the experimental spectrum of DIBP chelated on MgCl$_2$ (110). A correction factor of -50 cm$^{-1}$ (1690 – 1740 = -50) applies to all other bands. Table 5.2 shows the wavenumbers after corrections. From **Chapter 3**, it is obvious that the $\nu$(C=O) envelope of DIBP lies between 1730 and 1650 cm$^{-1}$. The components at 1740cm$^{-1}$, 1648 cm$^{-1}$ and 1619 cm$^{-1}$ cannot contribute to the $\nu$(C=O) envelope of experimental spectra. Therefore, the donor species on MgCl$_2$ (110) chelate and monodentate species on the polymer edge (110)/(001) is not required for explaining experimental spectra.

3. The 'free' molecule shown in Table 5.1 represents the uncoordinated DMP in the gas phase. On the other hand, 'free' DIBP band in the experimental spectra is from uncoordinated DIBP trapped in the film or DIBP physisorbed to the basal pane of MgCl2. In order to explain experimental spectra, we choose the wavenumber of uncoordinated DIBP in the experimental spectra.

**Table 5.2.** *DFT-D predicted wavenumbers after (i) merging components of the same species and (ii) approximation to experimental values observed for DIBP.*

| DFT Structure | (C=O) stretching | |
|---|---|---|
| | merged components wavenumber ($cm^{-1}$) | approximation to experimental spectra wavenumber ($cm^{-1}$) |
| 'Free' donor | 1787 (gas phase) | 1725 (liquid phase) |
| Donor on (110)/(001) **monodentate mode** | 1790 (dangling CO) 1698 (bound CO) | 1740 1648 |
| Donor on (110) **monodentate mode** | 1761 (dangling CO) 1711 (bound CO) | 1711 1661 |
| Donor on (104) **bridge mode** | 1752 | 1702 |
| Donor on (110)/(001) **chelate mode** | 1740 | 1690 |
| Donor on (110) **chelate mode** | 1753 1669 | 1703 1619 |

4.  According to Table 5.2, monodentate DMP on polymer edge (110)/(001)appears as two ν(C=O) bands. A higher wavenumber band at 1711 $cm^{-1}$and lower wavenumber band at 1661 $cm^{-1}$corresponding to the dangling (uncoordinated) carbonyl band and bound carbonyl band respectively. In **Chapter 4**, **Section 4.3.6**, we demonstrated the appearance of a new band around 1660 - 1665 $cm^{-1}$. This band was attributed to the bound CO of DIBP. As per DFT-D simulated spectra, the intensity ratio between the two bands of monodentate DMP species was 1:0.2. On the other

hand, the best fit was observed when the intensity ratio between dangling and bound CO was fixed in 1:1 (Figure 5.2b). The peak maxima was varying from 1660 to 1665 cm$^{-1}$. The difference in the relative intensity and variation in peak position might be due to the difference in the nature of MgCl$_2$ support. DFT models were based on clean MgCl$_2$ and DMP. In real conditions, MgCl$_2$/DIBP film is not free from coadsorbed ethanol.
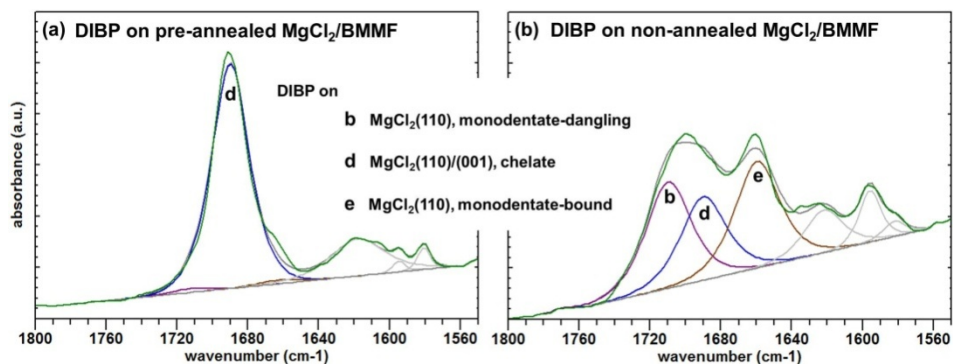


**Figure 5.2.** *Different DIBP species in the ν(C=O) envelope of in-situ coordinated DIBP on (a) annealed MgCl$_2$/BMMF film, (b) non-annealed MgCl$_2$/EtOH/BMMF film.*

The experimental ATR-FTIR spectra were simulated as a summation of Gaussian-Lorentzian function (GL – 70). Peak fitting simulations were carried out using casa XPS software (http://www.casaxps.com/). Infrared spectra were transferred to casa format. The ν(C=O) DIBP envelop was explained as the linear combination of five overlapping components correspond to the DIBP at four different chemical environments/phases;

i. Uncoordinated DIBP trapped in the film/physisorbed DIBP (component **'a'**).
ii. DIBP coordinated to two Mg ions on MgCl$_2$ (104) surface in 'bridge' mode (component **'c'**).
iii. DIBP coordinated to one Mg ion on MgCl$_2$ (110)/(001) edge in 'chelate' mode (component **'d'**).
iv. DIBP coordinated to one Mg ion on MgCl$_2$ (110) surface in 'monodentate' mode (component **'b'** and **'e'**).

The constraints used for peak fitting simulation of experimental spectra were summarized in the Table 5.3.

117

**Table 5.3.** *Constraints used for simulation of experimental spectra.*

| ID | Structure | Position (cm$^{-1}$) | FWHM |
|---|---|---|---|
| a | uncoordinated or physisorbed DIBP on (001) | 1727 - 1725 | 30 |
| b | DIBP on (110); mono - dangling | e + 50 | 30 |
| c | DIBP on (104); bridge | 1702 | 30 |
| d | DIBP on (110)/(001) ; chelate | 1690 | 30 |
| e | DIBP on (110); mono - bound | 1659 - 1663 | 30 |
| f | water (moisture) | 1622 - 1618 | 20, 40 |
| g | aromatic ring mode 1 | 1596 - 1592 | 0, 20 |
| h | aromatic ring mode 2 | 1582 - 1579 | 0, 20 |

As an example, the carbonyl stretching and aromatic ring mode bands of DIBP in the DIBP/MgCl$_2$ film (with 15 mol% DIBP loading) at various stages of the *in-situ* experiment is shown in Figure 5.3.
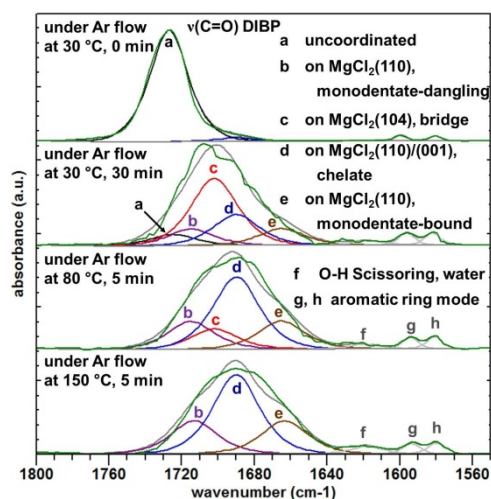


**Figure 5.3.** *Comparative in-situ ATR-FTIR spectra after peak fitting (DIBP to Mg mol ratio of 0.15).*

The relative amounts of the DIBP in various environments were calculated using the quantification method described in **Chapter 3**. In the following section,

the difference in the $\nu$(C=O) envelop of DIBP in various experiments were explained as different combinations of the above mentioned components.

## 5.4 Results and discussion

### 5.4.1 *In-situ* coordinated DIBP in pre-treated MgCl$_2$/EtOH film

As discussed in **Chapter 4.3.2**, $\nu$(C=O) envelops of *in-situ* coordinated DIBP on MgCl$_2$/EtOH film vary with the concentration of residual ethanol in the film. Carbonyl stretching and aromatic ring mode bands (after peak fitting) of *in-situ* coordinated DIBP on non-annealed and pre-annealed (80 °C) MgCl$_2$/EtOH films are shown in Figure 5.4. In the non-annealed MgCl$_2$ film, the majority of DIBP bound to MgCl$_2$ (110)/(001) edge (Figure 5.4a). DFT studies show that crystallization in the presence of a Lewis base can promote the formation of Lewis base covered MgCl$_2$ crystallites with (110) edges.[11-13] Therefore, the film formed by spin coating of the MgCl$_2$ solution in ethanol leads to the formation of MgCl$_2$ crystals with (110) edges and the edges covered by ethanol. Interaction of these MgCl$_2$ crystallites with DIBP solution in heptane leads to the replacement of ethanol with DIBP on (110) surface.

As opposed to the non-annealed MgCl$_2$/EtOH film, the majority of DIBP in the pre-annealed film is bound to MgCl$_2$ (104) site. Based on ATR-FTIR spectra shown in Figure 5.4b, we propose a reconstruction of MgCl$_2$ (110) surface into MgCl$_2$ (104) surface during the removal of ethanol. When MgCl$_2$/EtOH films annealed, the ethanol molecules desorb from (110) surface. This results in the destabilization of (110) surface. DFT studies showed that, in the absence of any adsorbate five-fold MgCl$_2$ (104) surface is more stable than four-fold MgCl$_2$ (110) surface.[9-10] If there is no other adsorbate to replace the vacancy created by the desorption of ethanol, the MgCl$_2$ (110) surface reconstructs into MgCl$_2$ (104). Therefore, the predominant lateral surface termination of the pre-annealed MgCl$_2$/EtOH crystal is MgCl$_2$ (104). Upon, *in-situ* coordination of DIBP the remaining (110) sites get saturated very fast and DIBP coordinate to MgCl$_2$ (104) surface as well.
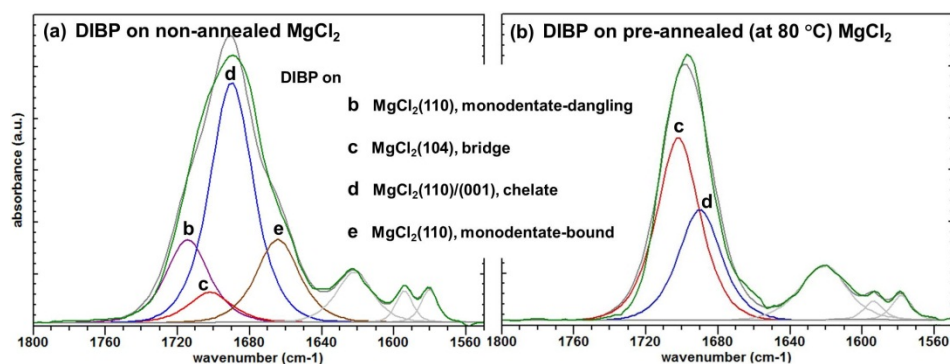
**Figure 5.4.** *Different DIBP species in the ν(C=O) envelope of in-situ coordinated DIBP on (a) non-annealed MgCl₂/EtOH film, (b)pre-annealed (80 °C) MgCl₂/EtOH film.*

## 5.4.2 Early stages of the formation of co-impregnated MgCl₂/EtOH/DIBP film

In **Chapter 3.3.3**, changes in the ν(C=O) DIBP bands in various co-impregnated MgCl₂/EtOH/DIBP films were monitored by *in-situ* ATR-FTIR. DIBP in the fresh out of the spin coat MgCl₂/EtOH/DIBP film remains uncoordinated. The ethanol concentration in this film was 18.5 mol% with respect to Mg. As soon as the co-impregnated MgCl₂/EtOH/DIBP films were exposed to an Ar flow at 30 °C, the sharp ν(C=O) DIBP band at 1725 cm⁻¹ (uncoordinated/physisorbed DIBP) shifted to a broad band at lower wavenumber. In the case of films with low donor loading, the band of uncoordinated DIBP completely disappeared within 30 minutes of Ar flow. Within this timeframe, the concentration of ethanol reduced to half of the initial amount.

Upon spincoating MgCl₂/DIBP/EtOH solutions, small corrugated MgCl₂ crystallites with (110) lateral cuts were formed. Recent DFT studies also support this phenomenon.[11,12] The changes in the ν(C=O) envelope upon exposing to Ar flow can be explained with two parallel/competing processes. The first process is the replacement of ethanol from MgCl₂ (110) surface by DIBP. The second process is the reconstruction of MgCl₂ (110) into MgCl₂ (104) surface as explained in the **Section 5.3.1**. DIBP also binds to the newly formed MgCl₂ (104) surface.

Peak resolved spectra of $\nu$(C=O) DIBP at early stages of MgCl$_2$/EtOH/DIBP (10 mol%) film formation is shown in Figure 5.5a. Initially DIBP has populated MgCl$_2$ (110)/(001) edges; since (110) is the most abundant (or may be the exclusive) surface site in the MgCl$_2$ crystallite formed from ethanol solution. When ethanol is removed from the film under an Ar stream, the (110) surface becomes unstable, and reconstruction of (110) surface to (104) surface occurs. As time progresses DIBP concentration on MgCl$_2$ (104) site increases faster than that of MgCl$_2$ (110)/(001) edges.
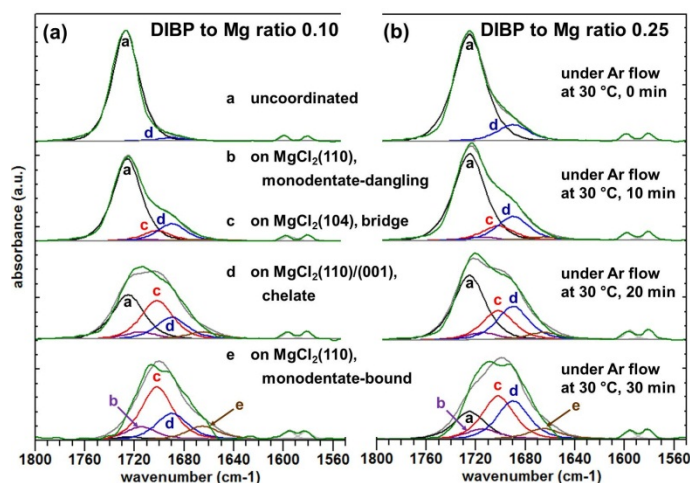


**Figure 5.5.** *Changes in the $\nu$(C=O) envelope of DIBP in co-impregnated MgCl$_2$/EtOH/DIBP films under Ar flow at 30 °C. (a) Donor to Mg ratio 0.10 (b)Donor to Mg ratio 0.25. Intensities of the bands are normalized.*

A similar trend was observed in the case of films with a high donor concentration. Due to the variation in the extent of MgCl$_2$ surface reconstruction, the relative abundance of DIBP on MgCl$_2$ (104) and (110) surfaces were different in films with different donor concentration. Peak resolved spectra of $\nu$(C=O) DIBP at early stages of MgCl$_2$/EtOH/DIBP (25 mol%) film formation is shown in Figure 5.5b.

After exposing the film under Ar flow for 30 minutes, the crystallites have both MgCl$_2$ (104) and MgCl$_2$ (110) surface. Both surfaces are populated by DIBP. Concentration of DIBP on MgCl$_2$ (104) reaches a saturation loading of ~10 mol% w.r.t. MgCl$_2$.

## 5.4.3 Annealing stage of co-impregnated MgCl$_2$/EtOH/DIBP film: effect of donor concentration and temperature

**Effect of donor concentration at 30 °C.** The ν(C=O) envelope of co-impregnated MgCl$_2$/EtOH/DIBP films at different initial donor concentrations are shown in Figure 5.6.
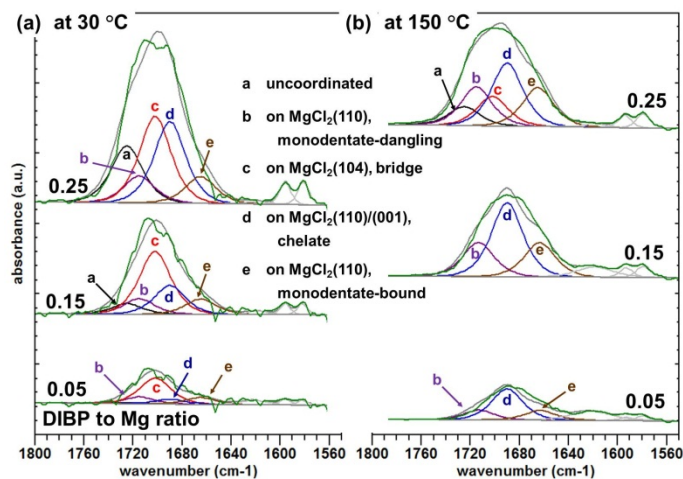


**Figure 5.6.** *Changes in the ν(C=O) envelope of DIBP in co-impregnated MgCl$_2$/EtOH/DIBP films. (a) At 30 °C, before annealing. (b) At 150 °C, after annealing.*

Within the 30 minutes of Ar flow, a significant amount of DIBP coordinates on MgCl$_2$ (104) and (110) sites. At low donor loading (DIBP to Mg mol ratio < 0.15), the DIBP concentration on MgCl$_2$ (104) site is higher than that of DIBP concentration on (110) sites. As the donor loading increases, the amount of DIBP on (104) increases and at a point becomes saturated (∼ 10 mol%); on the other hand the concentration of DIBP on (110) increases. In between the two different DIBP species on MgCl$_2$ (110), the amount of monodentate DIBP also reaches a saturation level (∼ 7 mol%), but the concentration of chelated DIBP on (110)/(001) edges increases constantly with the increase in the donor loading.

**Effect of temperature.** The ν(C=O) envelope of co-impregnated MgCl$_2$/EtOH/DIBP films before and after annealing process is shown in Figure 5.6. The changes in the ν(C=O) envelope of DIBP at different stages of annealing

122

is shown earlier in Figure 5.3. The relative amounts of the four DIBP components in the MgCl$_2$ films – with different initial DIBP loading – as a function of temperature are plotted in Figure 5.7.
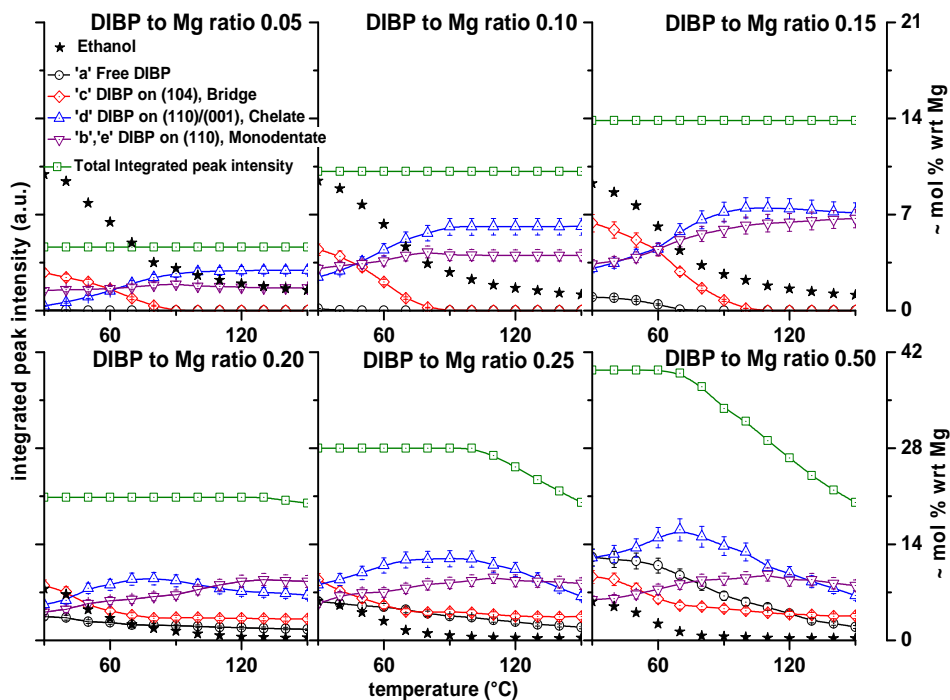


**Figure 5.7.** *Changes in distribution of DIBP among different components with respect to DIBP loading and temperature (the range of error due to the covariance of different components is shown along with each data point). The approximate amount of ethanol derived from the intensity of the (O-H) stretching band is included. The ethanol amounts are only a rough estimate due to the uncertainty of the XPS quantification of ethanol in MgCl$_2$ films.*

Ethanol preferably coordinates on MgCl$_2$ (110) site, and DIBP coordinates on the remaining surface sites. Upon thermal annealing, ethanol desorbs from the MgCl$_2$ (110) surface. As a Lewis base, DIBP prefers to bind the more acidic (110) surface. When the (110) surface become vacant by the removal of ethanol, DIBP migrates from less acidic MgCl$_2$ (104) sites to more acidic MgCl$_2$ (110) site and eventually binds on (110)/(001) edges [which is the least steric demanding sites on

(110) surface to form a chelated complex]. On a well-defined (110) surface, DIBP binds to monodenate mode. A minor increase in the amount of monodenate DIBP on (110) also occurs at low temperatures. In films with high donor loading, a small portion of uncoordinated DIBP also coordinates to (110) sites. This leads to the decrease in the intensity of uncoordinated DIBP signal. These effects were more pronounced in the temperature range of 30° – 80° C. Majority of the ethanol was desorbed from the film in this particular temperature range.

At temperatures above 80 °C, another phenomenon was observed. Especially in the case of films with donor to Mg ratio above than 0.20, the total intensity of the carbonyl band starts to decrease. It is assigned to the sintering of $MgCl_2$ crystals at high temperature. Irrespective of the initial loading, the maximum amount of donor coordinated to the $MgCl_2$ surface sites was around 18 mol% at 150 °C. The concentration of DIBP on (110)/(001) edge decreases at this particular temperature range. At the same time, the concentration of monodentate DIBP on (110) site increases to some extent. The ordering of $MgCl_2$ crystals at high temperature might result in the decrease of (110)/(001) edges. Due to this reorganization, chelated DIBP turned in to uncoordinated DIBP and released from the film under Ar flow at high temperature. Stacking of $MgCl_2$ layers turn the (110)/(001) edges to well-defined (110) surface. Subsequently, chelated DIBP forced to change the coordination mode into monodentate for relieving the steric hindrance. Concentration of DIBP on (104) sites remains constant at this stage.

## 5.5 Summary

Based on DFT-D predictions and *in-situ* ATR-FTIR results, we proposed an approach to explain the observed changes of the $\nu$(C=O) adsorption bands as a combination of five overlapping components assigned to uncoordinated/physisorbed DIBP, DIBP adsorbed to $MgCl_2$ (104) in 'bridge' mode, DIBP adsorbed to $MgCl_2$ (110)/(001) in 'chelate' mode and DIBP adsorbed to $MgCl_2$ (110) surface in 'monodentate' fashion. According to this approach, we reach the following conclusions.

1.  Ethanol – *not DIBP* – is the surfactant or coordinated species during the $MgCl_2$ crystallite formation.

2.  Small, highly disordered crystallites of $MgCl_2$ formed in the presence of ethanol. These crystallites have $MgCl_2$ (110) as the preferred lateral surface termination.

3.  Ethanol adsorbs stronger than DIBP on $MgCl_2$ (110); yet leaves the $MgCl_2$ surface easier than DIBP because of the low boiling point of ethanol compared to DIBP.

4.  In neat $MgCl_2$, five-fold (104) surface is more stable than four-fold (110) surface. However, the adsorption of Lewis bases on these two surfaces lowers the surface energies in different extent; eventually $MgCl_2$ (110) with the adsorbed Lewis base turn out to be more stabilized than $MgCl_2$ (104) surface.

5.  At room temperature, a significant amount of chelated DIBP species on (110)/(001)is present in the film. Especially at higher donor concentration, this was the major species at room temperature. In an adsorbate rich environment (ethanol + DIBP), highly discorded $MgCl_2$ crystallites with a very high relative abundance of (110)/(001) edges can be formed. TEM studies shown in **Chapter 4.3.1** supports the existence of highly disordered $MgCl_2$ crystallites in the ethanol rich environment (irrespective of the presence or absence of DIBP).

6.  Conversely, desorption of ethanol/Lewis base from $MgCl_2$ (110) surface makes the surface unstable. This leads to the reconstruction of $MgCl_2$ (110) surface into $MgCl_2$ (104) surface. If any uncoordinated DIBP is present in the film, DIBP coordinates to (104) surface in abridge mode.

7.  The reconstruction (110) surface to (104) surface was intense in the absence of any other adsorbate molecule. On the other hand, if any other adsorbate (such as DIBP) present in the film, the adsorbate will replace the vacancy created by ethanol on (110), in turn stabilize the surface.

8.  In a co-impregnated $MgCl_2$/EtOH/DIBP film, ethanol prefers adsorption on $MgCl_2$ (110); therefore, it guides the weaker DIBP to adsorb on $MgCl_2$ (104) formed upon reconstruction.

9.  Upon annealing the $MgCl_2$/EtOH/DIBP film under Ar flow at a temperature range of 30 – 80 °C; an increase in the quantity of chelated DIBP species on (110)/(001) and monodentate DIBP species on (110) surface, along with the

decrease in bridge DIBP species on (104), was observed. This might be due to the redistribution of DIBP from weakly Lewis acidic (104) site to strongly Lewis acidic (110) site.

10. Annealing the $MgCl_2$/EtOH/DIBP film under Ar flow, also induces a mild sintering (compared to the severe sintering of donor free $MgCl_2$ crystals) of $MgCl_2$ crystallites. This could explain the decrease in the overall intensity of DIBP envelope. This phenomenon can detect with IR only in the films with a high initial concentrationof DIBP.

11. Upon annealing (especially at a temperature range of 80 – 150 °C), stacking/ordering of $MgCl_2$ layers occur, which reduces the abundance of (110)/(001) edges. This could be the reason for the selective desorption of chelate DIBP species from (110)/(001) edges at high temperature. At the same time, improvement in the stacking/ordering leads to the increase the abundance of (110) surface and hence the concentration of monodentate DIBP species.

In conclusion, our combined flat model and DFT-D approach proved to be a powerful tool for understanding the genesis and surface structure of $MgCl_2$/EtOH/DIBP Ziegler-Natta catalyst precursor phases. In fact, semi-quantitative measurements of local siting for DIBP molecules on $MgCl_2$ were successfully achieved. The ability of such molecules to relocate on different crystal terminations was highlighted. At the same time, the rapid reconstruction of $MgCl_2$ surfaces, in order to minimize the instability caused by the Lewis base desorption was also noted. Information about the surface chemistry of $MgCl_2$ support is important to design the tailor made electron donors, which can improve the performance of $MgCl_2$ supported Ziegler-Natta catalysts.

## 5.6 References

(1)  Moore, E. P. Jr. *Polypropylene Handbook: Polymerization;* Hanser Publishers: New-York, **1996,** Chapter 2.

(2)  Chadwick, J. C.; Garoff, T.; Severn, J. R. *Tailor-Made Polymers via Immobilization of Alpha-Olefin Polymerization Catalysts;* Severn, J. R.; Chadwick, J. C., Eds.; WILEY-VCH: Weinheim, **2008,** Ch. 2.

(3)  D'Amore, M.; Credendino, R.; Budzelaar, P.; Causa, M.; Busico, V. *J. Catal.* **2012,** *286,* 103.

(4)  Kim, S. H.; Somorjai, G. A. *Surf. Interface. Anal.* **2001,** *31*, 701.

(5)   Andoni, A.; Chadwick, J. C.; Milani, S.; Niemantsverdriet, J. W. (Hans).; Thüne, P. C. *J. Catal.* **2007,** *247* (2), 129.

(6)   Andoni, A.; Chadwick, J. C.; Niemantsverdriet, J. W. (Hans).; Thüne, P. C. *Macromol. Symp.* **2007,** *260,* 140.

(7)   Andoni, A.; Chadwick, J. C.; Niemantsverdriet, J. W. (Hans).; Thüne, P. C. *Macromol. Rapid Commun.* **2007,** *28* (14), 1466.

(8)   Andoni, A.; Chadwick, J. C.; Niemantsverdriet, J. W. (Hans).; Thüne, P. C. *J. Catal.* **2008,** *257,* 81.

(9)   Busico, V.; Causa, M.; Cipullo. R.; Credendino, R.; Cutillo, F.; Friederichs, N.; Lamanna, R.; Segre, A.; Castelli, V. V. A. *J. Phys. Chem C* **2008,** *112*, 1081.

(10)  Credendino, R.; Busico, V.; Causa, M.; Barone, V.; Budzelaar, P. H. M.; Zicovich-Wilsone, C. *Phys. Chem. Chem. Phys.* **2009,** *11,* 6525.

(11)  Turunen, A.; Linnolahti, M.; Karttunen, V, A.; Pakkanen, T, A.; Denifl, P.; Leinonen, T. *J. Mol. Catal. A: Chem.* **2011,** *334,* 103.

(12)  Credendino, R.; Pater, J. T. M.; Correa, A.; Morini, G.; Cavallo, L. *J.Phys. Chem. C* **2011,** *115,* 13322.

(13)  Correa, A.; Credendino, R.; Pater, J. T. M.; Morini, G.; Cavallo, L. *Macromolecules* **2012,** *45* (9), 3695.

127

128

**6**

**In-situ propylene polymerization over MgCl$_2$/DIBP/TiCl$_4$ films**

# Abstract

*In order to test the activity of the catalyst prepared from spin coated MgCl$_2$/DIBP precatalyst films and to correlate surface chemistry (studied by infrared and DFT) of the catalyst to polymer activity, in-situ propylene polymerization was carried out in the ATR-FTIR flow cell. The growth of polypropylene over the catalyst was monitored by attenuated total internal reflection Fourier transform spectroscopy (ATR-FTIR). Various steps in the catalyst preparation such as TiCl$_4$ grafting over MgCl$_2$ surface and MgCl$_2$/TiCl$_4$ catalyst activation using AlEt$_3$ were performed in-situ in the ATR flow cell. Interactions of DIBP with catalyst (TiCl$_4$) and co-catalyst (AlEt$_3$) have been investigated in-situ. The isotacticity of the polypropylene produced in the presence and absence of donor has been estimated based on characteristic peaks in the infrared. Changes in these characteristic peaks upon melting and recrystallization of polypropylene film were noticed. In parallel, the Ti loading in Ziegler-Natta catalysts with and without internal donor was estimated with X-ray photoelectron spectroscopy (XPS). Changes in the Ti 2p$^{3/2}$ signal upon internal donor (4-fluoro diisobutyl phthalate) incorporation and AlEt$_3$ treatment were investigated.*

# 6.1 Introduction

**M**ost of the heterogeneous $MgCl_2$-supported Ziegler-Natta catalysts for stereospecific olefin polymerization contain $MgCl_2$ as the support, $TiCl_4$ as the catalyst, a trialkyl aluminium as the co-catalyst, and two Lewis bases acting as internal and external donors.[1] The catalyst is generally described as particles of activated $MgCl_2$, composed of irregularly stacked Cl-Mg-Cl sandwich-like monolayers, with the microstructures terminated by the (110) and (104) lateral cuts.[2-4]

The reaction of the $MgCl_2$ support with $TiCl_4$ leads to the adsorption of $TiCl_4$ on the lateral cleavage surfaces of $MgCl_2$, such as the (110) and (104) cuts. On reaction with the cocatalyst (aluminium alkyls), $Ti^{4+}$ is reduced to $Ti^{3+}$, forming a Ti-C bond, which is essential for monomer insertion. For isotactic propylene polymerization, the incorporation of an internal donor is required in the catalyst preparation to control the amount and distribution of $TiCl_4$ on the support surface.[5] However, internal donors such as esters and diesters have a tendency to react with the $AlR_3$ cocatalyst during polymerization due to the nucleophilic attack of the Al-C bond to the carbonyl group and hence are easily displaced from the solid catalyst surface.[6,7]

The incorporation of internal donors such as EB and DIBP improves the stereospecificity of $MgCl_2$ supported catalyst, and the catalyst system provides high stereospecificity above 95% at a short polymerization time.[8] However, with the increase of polymerization time a part of the internal donor is removed from catalyst as the result of the interaction of the catalyst with cocatalyst ($AlR_3$). The removal a part of the internal donor from the catalysts is accompanied by drastic decrease catalyst selectivity (stereospecificity).

Therefore, good performance in terms of stereospecificity can be reached only by: (i) preventing the displacement of the $MgCl_2$-coordinated internal donor by the reaction with cocatalyst $AlR_3$ or (ii) using another Lewis acids (external donors such as alkoxysilanes) along with $AlEt_3$ to replace the vacancies created by internal donor displacement from $MgCl_2$ surface.

In spite of numerous efforts, questions regarding which of the $MgCl_2$ surface plane is the most preferred cut for the $TiCl_4$ fixation, and the precise structure of the titanium active centers formed by treatment of the catalyst with the aluminium alkyl cocatalyst, have still not yet found definitive answers.

Busico and coworkers proposed a model for the structure of aspecific and isospecific sites from a view point of the adsorption states of $TiCl_4$ precursors on catalytically active $MgCl_2$ (110) or (104) lateral cuts.[9] An aspecific $TiCl_4$ mononuclear species was dominant on the (110) surface, while an isospecific $TiCl_4$ dinuclear species was favoured on the (104) surface. Accordingly, the (110) and (104) cuts were respectively regarded as non-stereospecific and stereospecific.

An extended X-ray adsorption fine structure (EXAFS) analysis for a $TiCl_4/MgCl_2$ pre-catalyst indicated the dinuclear species on the (104) surface.[10] Nevertheless, an investigation of the Raman spectra of the products of the co-milling mixtures of $MgCl_2$ and $TiCl_4$ came to the conclusion, supported by *ab initio* calculations, that the adsorption of $TiCl_4$ gave a species with octahedrally coordinated titanium on the (110) lateral cut of $MgCl_2$.[11,12] This stable complex was not removed by washing with solvent, whereas dimeric species ($Ti_2Cl_8$) on the (104) cut were easily removed.

First principle calculations showed a consistent trend, preference of the $TiCl_4$ mononuclear species on the (110) surface, and that of the $TiCl_4$ dinuclear species on the (104) surface, which was as stable as the mononuclear species on the same surface, but absolutely less stable than the mononuclear species on the (110) surface.[13-16] DFT studies performed by Terano and coworkers predicted the formation of isospecific Ti dinuclear species on a $MgCl_2$ (110), as a consequence of Ti species reduction from $Ti^{4+}$ to $Ti^{3+}$ upon exposing to $AlEt_3$.[17]

Based on above researches, it is believed that the monomeric species with octahedrally coordinated titanium as the precursor for the stereospecific active sites in $MgCl_2$-supported catalysts.

X-ray photoelectron spectroscopy (XPS) has been widely used to investigate the oxidation state of Ti species in the Ziegler-Natta catalyst and the changes in the electronic structure around Ti metal upon the incorporation of electron donor.[18-25] Upon interaction with electron donor, the binding energy of Ti

signal lowers, and the FWHM of the signal broadens (Ti $2p^{3/2}$ signal at 458.9 eV shifts to lower number around 458.5 $\pm$3).[20,24] The Ti $2p^{3/2}$ signal lowers after treatment with aluminium alkyl compounds and the FWHM of the signal broadens. The interaction of the $TiCl_4/MgCl_2$ system with trialkylaluminum is known to result in the creation of the Ti (III) and Ti (II) species as well as alkylation of these species with the formation of Ti-C bonds.[26] The reduction reactions resulting in formation of $Ti^{3+}$ and $Ti^{2+}$ had close potential barriers, but the $Ti^{3+}$ species are more preferable due to steric reasons (complexation of $Ti^{3+}$ species by $AlR_2Cl$ would prevent subsequent reduction).[27] Due to the presence of unpaired electron the Ti(III) species are an appropriate object for electron spin resonance (ESR) detection, nevertheless only 10 – 20 % of Ti(III) give the ESR signal, and so the majority of Ti(III) was suggested to form polynuclear (aggregated) Ti species with low spin structure.[28-31] Alkylation of $TiCl_3$ species includes two steps; formation of complex $TiCl_3.AlEt_3$ and its dissociation. The dissociation is promoted by additional $AlEt_3$ molecule since it facilitates elimination of $AlEt_2Cl$ bound to $Ti^{3+}$ species due to the formation of complexes such as $AlEt_2Cl.AlEt_3$.[27]

Surface sensitive vibrational spectroscopic techniques could provide further information on the nature of the Ti species.[21] Far infrared spectra of Ziegler-Natta catalyst system provide direct information about metal-halogen bonds (such as Ti-Cl, Mg-Cl bonds). The mid-infrared spectroscopy only can be used to monitor the changes in IR bands of electron donor upon interaction with $TiCl_4$ and $AlEt_3$.[32-38]

In previous chapters **(Chapter 3, 4, 5)**, we have concluded that various surface complexes formed at the interaction of carbonyl groups of DIBP with different surface sites of $MgCl_2$ support can be characterized by *in-situ* ATR-FTIR. In this chapter, we explore the feasibility of applying ATR-FTIR to monitor titanation of $MgCl_2$/EtOH/DIBP films followed by *in-situ* propylene polymerization over the flat model catalyst. The interactions of diisobutyl phthalate (DIBP) with $TiCl_4$ and $AlEt_3$also studied by *in-situ* ATR-FTIR. Additionally, an attempt is made to estimate the isotacticity index (I.I.) of polypropylene (PP) prepared in systems with and without donor. Surface chemistry of various catalyst systems can be directly correlated to isotacticity of the polymer. Since mid-infrared spectra does not provide any characteristic bands of $TiCl_4$, estimation of Ti content in the films were performed by XPS. The composition of

$MgCl_2/FDIBP/TiCl_4/AlEt_3$ catalysts and the changes in the Ti species signals upon DIBP and $AlEt_3$ interaction were studied by XPS.

## 6.2 Experimental

### 6.2.1 Materials

Anhydrous magnesium chloride (ball milled, 99.9%), heptane (99%), benzene (99.8%), titanium tetrachloride (99.9%) and triethylaluminium solution in toluene (25 wt%) were purchased from Aldrich Chemicals and used as received. Absolute ethanol (99.9%) and diisobutyl phthalate (97%) were purchased from Merck Chemicals and used as received. Argon (grade 6.0) was purchased from Linde and used after passing through a $Cr/\gamma-Al_2O_3$tube. Propylene was supplied by Linde (grade 3.5).

### 6.2.2 Preparation of MgCl$_2$/donor thin films

From a bulk solution of $MgCl_2$ (105 mmol dm$^{-3}$) in ethanol, solutions with donor/$MgCl_2$ molar ratios of 0.15 were prepared.Donor-free $MgCl_2$ films were also prepared. All these preparations were carried out in $N_2$ atmosphere. In a typical procedure, the solution was spin coated (2800 r.p.m.) under the glovebox conditions onto a ZnSe crystal (for ATR-FTIR studies) or a Si(100)/SiO$_2$ wafer (for XPS studies).

### 6.2.3 Preparation and loading of DIBP/heptane, TiCl$_4$/heptane and AlEt$_3$/heptane solutions

DIBP/heptane (20 μL/mL heptane), $TiCl_4$/heptane (10% v/v) and $AlEt_3$/heptane (1 mg/mL) solutions were prepared under glovebox conditions. We choose heptane as the solvent, for monitoring *in-situ* coordination of donor on $MgCl_2$, since the IR spectra of heptane does not contain any signals around 1800 cm$^{-1}$ to 1600 cm$^{-1}$ where the $\nu(C=O)$ bands of esters, diesters and succinates appear. The solution was filled in one line of a small volume dispenser (discussed in **Chapter 2**) using a syringe. In the same manner, the remaining three lines were filled with pure heptane. The dispenser unit is then transferred from the glovebox and connected to the ATR reactor line.

### 6.2.4 Analytical techniques

All FTIR spectra were collected using a Nicolet Protégé 460 Fourier transform infrared spectrometer equipped with a heated HATR flow cell from Spectra-Tech ARK with a ZnSe 45° crystal (cut-off at 800 cm$^{-1}$).The coated ZnSe crystal was mounted and sealed under a nitrogen atmosphere in an ATR-cell. FTIR spectra were measured in absorbance mode using a ZnSe background (taken at 30 °C) with a resolution of 4 cm$^{-1}$ and 4 scans per measurement.

XPS measurements were performed with a Kratos AXIS Ultra spectrometer, equipped with a delay-line detector (DLD) and a monochromatic Al Kα X-ray source (Al Kα 1486.3 eV) operating at 150 W. The coated Si wafer was transferred (using the XPS transfer vessel) under a nitrogen atmosphere into the XPS-antechamber and then under high vacuum conditions into the measurement chamber. Spectra were recorded at a background pressure of 2 x 10$^{-9}$ mbar. XPS measurements of the grafting experiments of $SiO_2$ were calibrated using Si 2p signal of the $SiO_2$ wafer [Si 2p ($SiO_2$) = 103.30 eV].[39]

## 6.2.5 Internal donor – TiCl$_4$ or AlEt$_3$ interactions in ATR-FTIR flow cell

For monitoring internal donor interactions with TiCl$_4$ and AlEt$_3$, the corresponding heptane solutions (from the small volume dispenser) were flowed through the cell for 20 min at a flow rate of 0.1 mL donor solution/min. Then heptane (from the small volume dispenser) was flowed through the cell for 60 min at a flow rate of 0.1 mL heptane/min. FTIR spectra were measured at the regular intervals (approximately every two minutes).

### 6.2.6 *In-situ* propylene polymerization in ATR-FTIR reactor

The ZnSe ATR-FTIR crystal was assembled into the flow cell then closed / sealed and transferred afterwards to the ATR-FTIR set-up. The time-resolved ATR-FTIR polymerization experiment at room temperature was performed as follows. Anhydrous benzene was introduced into the flow cell, and an FTIR spectrum was collected for reference. We choose benzene as the solvent, for monitoring *in-situ* propylene polymerization, since IR spectrum of benzene do not

have any alkyl $\nu$(C-H) signals to interfere with $\nu$(C-H) signals of growing polypropylene film. In the meantime, an $Al(C_2H_5)_3$ solution in benzene had been saturated with propylene under a 2 bar pressure in a pre-reactor. After that, the $Al(C_2H_5)_3$ solution with propylene was allowed to flow into the ATR flow cell at a speed of 0.5 mL/min, which was the starting point of the reaction and collection of FTIR spectra. The data points of the collected spectra were the average of 4 scans at a spectral resolution of 4 cm$^{-1}$, and the spectra were automatically collected every 30 seconds. The polymer growth was continuously monitored by *in-situ* ATR-FTIR until the $\nu$(C-H) bands of polymer get saturated. The polymer film is then washed with pure benzene in order to remove excess AlEt$_3$ from the film (AlEt$_3$ turns to Al$_2$O$_3$ upon exposing the film to air; which in turn mislead polymer yield when weighing the polymer film. The ATR-FTIR flow cell set up has been described in **Chapter 2**.

## 6.3 Results and discussion

### 6.3.1 *In-situ* ATR-FTIR studies on MgCl$_2$/DIBP – TiCl$_4$ interactions

MgCl$_2$/EtOH/DIBP solutions were spin coated and the films were transferred to ATR cell, followed by annealing the film under Ar flow. The effect of TiCl$_4$ on MgCl$_2$/EtOH/DIBP films was then investigated by means of ATR-FTIR. The $\nu$(C=O) envelope of DIBP in the annealed MgCl$_2$/EtOH/DIBP film (ethanol free) did not change after *in-situ* TiCl$_4$ treatment. Exposure of TiCl$_4$ to a non-annealed MgCl$_2$/EtOH/DIBP caused a band shift towards lower wavenumber (similar to that noted upon annealing). Within one minute of TiCl$_4$ impregnation, complete removal of ethanol from the film was observed. The resemblances in the $\nu$(C=O) envelopes of DIBP after annealing and TiCl$_4$ treatment indicates that the removal of ethanol leads to the redistribution of various DIBP surface species. Thermal annealing, TiCl$_4$ treatment and AlEt$_3$ treatment are the three common processes to remove alcohol (dealcoholation) from MgCl$_2$.nROH adducts.[40] The $\nu$(C=O) DIBP envelopes were resolved into components as described in **Chapter 5**. Peak resolved $\nu$(C=O) DIBP envelopes and of pre-annealed and non-annealed MgCl$_2$/EtOH/DIBP films before and after TiCl$_4$ treatment is shown in Figure 6.1.

As mentioned earlier, TiCl$_4$ can be used to remove ethanol from the MgCl$_2$/EtOH film as an alternative to annealing. Within 1 – 2 minutes of TiCl$_4$ exposure, ethanol was completely removed from MgCl$_2$/EtOH film. The film was then exposed to heptane flow in order to remove excess unbound TiCl$_4$ in the cell and lines. Subsequent *in-situ* coordination of DIBP on MgCl$_2$/TiCl$_4$ film result in a sharp DIBP band around 1700 cm$^{-1}$. Peak fitting shows that the predominant DIBP species in the film was bridged DIBP on MgCl$_2$ (104) surface. This result was similar to the *in-situ* DIBP coordination on pre-annealed MgCl$_2$/EtOH film. Therefore, irrespective of the thermal or chemical method; removal of ethanol from MgCl$_2$ (110) surface result in the reconstruction of MgCl$_2$ (110) surface into (104) surface.
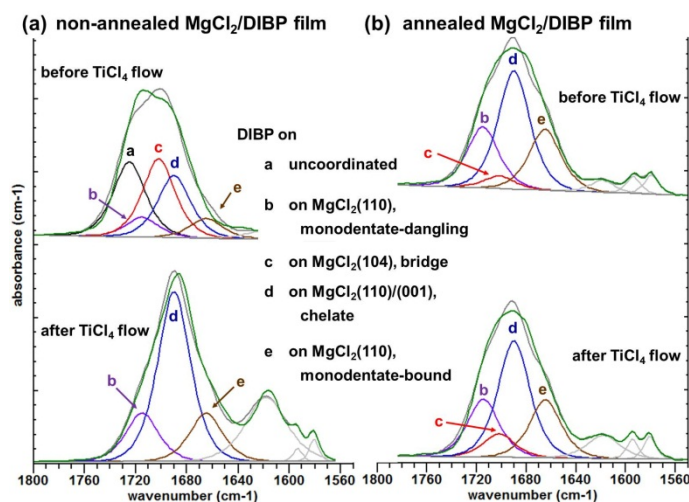


**Figure 6.1.** *(a) ν(C=O) DIBP envelope of non-annealed MgCl$_2$/EtOH/DIBP film; before (top) and after (bottom) TiCl$_4$ treatment. (b) ν(C=O) DIBP envelope of annealed MgCl$_2$/EtOH/DIBP (quasi ethanol free) film; before (top) and after (bottom) TiCl$_4$ treatment.*

Interaction of TiCl$_4$ with *in-situ* coordinated DIBP on MgCl$_2$ was monitored by ATR-FTIR. The ν(C=O) envelope of *in-situ* coordinated DIBP did not change during TiCl$_4$ treatment. The ν(C=O) envelope of *in-situ* coordinated DIBP in MgCl$_2$/EtOH film after TiCl$_4$ treatment is shown in Figure 6.2.

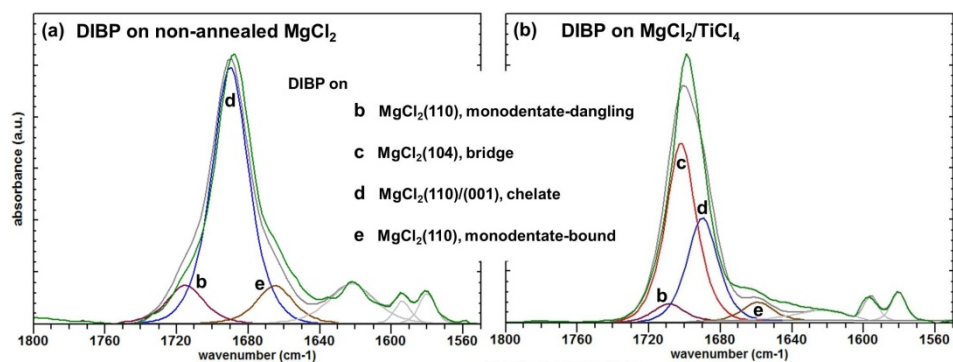**Figure 6.2.** *(a) ν(C=O) DIBP envelope of in-situ coordinated DIBP on non-annealed MgCl₂/EtOH film; followed by TiCl₄ treatment. (b) ν(C=O) DIBP envelope of in-situ coordinated DIBP on TiCl₄ pretreated MgCl₂/EtOH film.*

It is well known that the reaction of $TiCl_4$ with uncoordinated ester/diester donor result in the formation of $TiCl_4$.donor molecular complexes. The $\nu(C=O)$ signal of these complexes appeared at a lower wavenumber at a lower wavenumber, in comparison with $\nu(C=O)$ signal of donor bound to $MgCl_2$. According to the literature, the $\nu(C=O)$ envelope of DIBP in the $TiCl_4$/DIBP complex appears at 1640-1581 cm$^{-1}$ region.[41-43]

It is clear from the spectra shown in Figure 6.1 and 6.2 that we did not observe any characteristic $\nu(C=O)$ signals of $TiCl_4$.DIBP molecular complexes. After treatment of $MgCl_2$/DIBP film with $TiCl_4$, the $\nu(C=O)$ signals of DIBP bound to $MgCl_2$ surface was remained almost same; implying that DIBP remains strongly coordinated to $MgCl_2$. As opposed to the DRIFT studies performed by Potapov and coworkers, we did not observe any decrease in the $\nu(C=O)$ intensity upon $TiCl_4$ treatment.[37] This might be due to the fact that Ti finds the vacant sites on $MgCl_2$ surface; since the optimum coverage ($\theta$) of DIBP is well below one as per DFT.

## 6.3.2 *In-situ* ATR-FTIR studies on MgCl₂/DIBP – AlEt₃ interactions

Preliminary studies on the interaction of $AlEt_3$ cocatalyst with $MgCl_2$/DIBP/EtOH film were performed by means of *in-situ* ATR-FTIR. Figure

6.3 depicts the peak resolved ν(C=O) DIBP envelopes of pre-annealed and non-annealed $MgCl_2$/EtOH/DIBP films, before and after $AlEt_3$ treatment.

Upon exposing to $AlEt_3$ flow, ethanol signals from non-annealed $MgCl_2$/DIBP films were disappeared very quickly (similar to that noted upon annealing and $TiCl_4$ treatment). The redistribution of DIBP surface species was also similar to that of annealing or $TiCl_4$ treatment. Irrespective of initial ethanol concentration, we observed that $AlEt_3$ removed the half of (~ 55 %) of DIBP in the DIBP/$MgCl_2$ surface complexes. DRIFT studies by Potapov and coworkers noticed the removal of 50% EB upon interaction with $AlEt_3$.[38] In between various DIBP species, we did not observe any difference in the reactivity with $AlEt_3$.
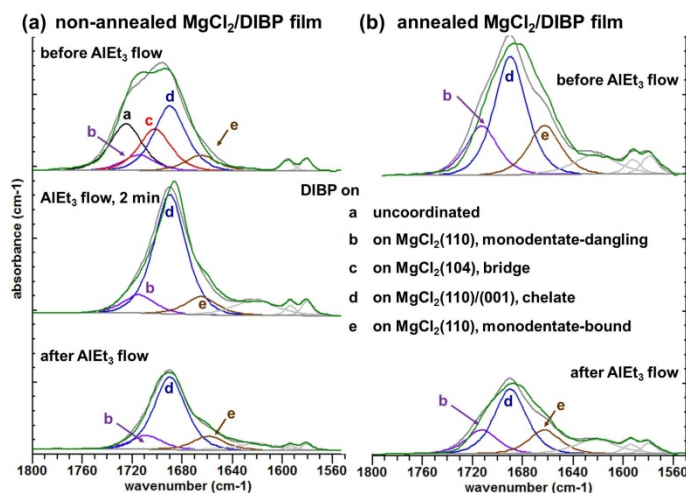


**Figure 6.3.** *(a) ν(C=O) DIBP envelope of non-annealed MgCl₂/EtOH/DIBP film; before (top), 2 minutes of AlEt₃ flow (middle) and after (bottom) AlEt₃ treatment. (b) ν(C=O) DIBP envelope of annealed MgCl₂/EtOH/DIBP (quasi ethanol free) film; before (top) and after (bottom) AlEt₃ treatment.*

## 6.3.3 XPS analysis on flat-model Ziegler-Natta catalyst composition

Since it is difficult to probe/quantify $TiCl_4$ using ATR-FTIR, we used the XPS technique to study the $TiCl_4$ – internal donor interactions on a fluorinated analogue of DIBP (4-fluorodiisobutyl phthalate, shortly denoted as FDIBP).

$MgCl_2$/ethanol/FDIBP solutions were spin coated on silicon wafers. Donor free $MgCl_2$/EtOH films were also prepared. Half of the wafers were annealed at 150 °C for 30 minutes and cooled down to room temperature. Annealing makes these films quasi ethanol free. All wafers then soaked in $TiCl_4$/heptane (10% v/v) solutions for 30 minutes. In order to remove the physisorbed $TiCl_4$ – if any – remaining in the film; the wafers were soaked in the heptane solution for 30 minutes. Using the same procedure used for $TiCl_4$ impregnation, we studied the action of $AlEt_3$ (1 mg/mL in heptane; same as the concentration used for olefin polymerization) on $MgCl_2$/FDIBP films and $MgCl_2$/FDIBP/$TiCl_4$ films. The general trends in the mol ratios of internal donor, Ti and Al with respect to Mg in all these samples are shown in Table 6.1.

**Table 6.1.** *Titanium and donor concentration with respect to Mg in various planar model Zigler-Natta precatalyst systems; estimated by XPS.*

| Catalyst / precatalyst system | Annealing | Mg : F | Mg : Ti | Mg : Al |
|---|---|---|---|---|
| $MgCl_2$/$TiCl_4$ | -- | -- | 0.36 | -- |
| ,, | 150 °C | -- | 0.04 | -- |
| $MgCl_2$/FDIBP | -- | 0.15 | -- | -- |
| ,, | 150 °C | 0.14 | -- | -- |
| $MgCl_2$/FDIBP/$TiCl_4$ | -- | 0.13 | 0.21 | -- |
| ,, | 150 °C | 0.15 | 0.14 | -- |
| $MgCl_2$/FDIBP/$AlEt_3$ | -- | 0.06 | -- | 0.16 |
| ,, | 150 °C | 0.08 | -- | 0.08 |
| $MgCl_2$/FDIBP/$TiCl_4$/$AlEt_3$ | -- | 0.11 | 0.16 | 0.11 |
| ,, | 150 °C | 0.10 | 0.12 | 0.05 |

Ti content in all these films was decreased upon pre-annealing of $MgCl_2$ or $MgCl_2$/FDIBP films. The Ti content in donor free film at room temperature was exceptionally high, which goes exceptionally low after annealing. The extreme low Ti loading might be related to the unavailability of lateral surface sites due to the sintering of $MgCl_2$ at high temperature. In the case of films containing internal

donor, the extent of reduction in Ti content upon annealing was low. Before and after $TiCl_4$ treatment the internal donor concentration remains almost same. This is in agreement with *in-situ* ATR-FTIR studies on DIBP – $TiCl_4$ interactions. When $MgCl_2$/FDIBP film was exposed to $AlEt_3$ solution, a significant reduction in the donor concentration was observed. The similar trend was observed in the case of $MgCl_2$/FDIBP/$TiCl_4$ systems. A wide scan of $MgCl_2$/FDIBP/$TiCl_4$/$AlEt_3$ catalyst's XPS spectra is shown in Figure 6.4a.
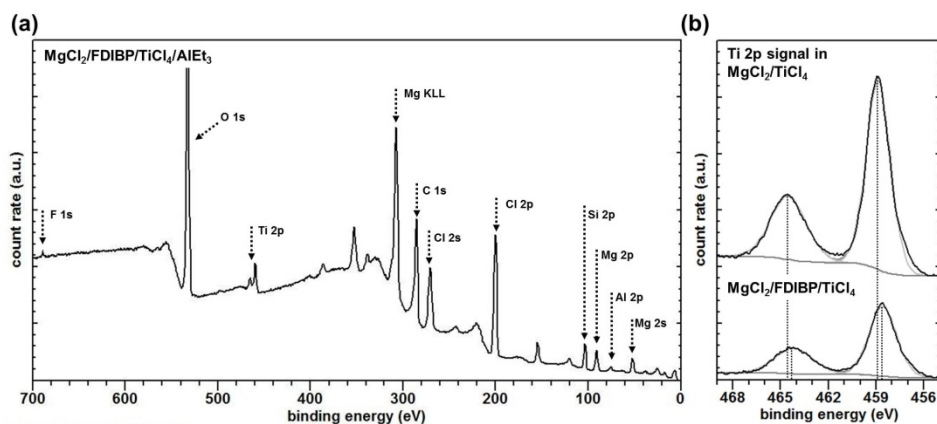


**Figure 6.4.** *(a) Wide scan of $MgCl_2$/FDIBP/$TiCl_4$/$AlEt_3$ XPS spectra. (b) Ti 2p signal from $MgCl_2$/$TiCl_4$ and $MgCl_2$/FDIBP/$TiCl_4$; differences in the binding energies of Ti 2p are evident.*

XPS studies on the Ti $2p^{3/2}$ binding energy shifts (to lower numbers) and band broadening upon interaction with electron donors and $AlR_3$ were widely reported in literature.[19,20,23-25] Binding energy shifts are due to the contributions from the changes in oxidation state of the target atom and/or the changes in electron density on the nearest neighbour atoms to the target atom. Ti $2p^{3/2}$ signal in $MgCl_2$/$TiCl_4$ was observed at 459.0 eV, whereas Ti $2p^{3/2}$ signal in the $MgCl_2$/FDIBP/$TiCl_4$ appeared at 458.5 eV. Upon $AlEt_3$ treatment, the signal was broadened and a very weak shoulder was appeared at $\sim$ 457 eV. The increase in FWHM of Ti $2p^{3/2}$ band (in this particular case, from 2.6 to 3.0) might indicate the formation of Ti species with oxidation states lower than $Ti^{4+}$. However, a well resolved peaks for $Ti^{3+}$ (should appear at 457.4 eV)[44] or $Ti^{2+}$ (should appear at

456.2 eV)[56] were not observed. As an example, a comparison of Ti 2p signal from the $MgCl_2$/$TiCl_4$ film and $MgCl_2$/$TiCl_4$/FDIBP/AlEt₃ film is shown in Figure 6.4b.

## 6.3.4 *In-situ* propylene polymerization over $MgCl_2$/DIBP/$TiCl_4$ and $MgCl_2$/$TiCl_4$ catalysts

Propylene polymerization was carried out in the *in-situ* ATR setup. $MgCl_2$/DIBP (DIBP to Mg ratio 0.15) solution in ethanol was spin coated over ZnSe ATR crystal inthe glove box. All further steps of the catalyst preparation and polymerization were done *in-situ*. The $MgCl_2$ films were exposed to $TiCl_4$/benzene (10% v/v) flow (0.1 mL/min for 60 min) followed by washing the film under benzene flow (0.1 mL/min, for 60 min) wash. The polymerization was performed under 1 mg/mL AlEt₃ flow (0.5 mL/min), 2 bar propylene pressure at 30 °C for 3 h. The polymerization was monitored by *in-situ* ATR-FTIR in every 30 seconds. It has to be noted that we did not use any external donor.

Kinetic investigations of ethylene or propylene polymerization using supported catalysts were usually carried out using an indirect method by measuring the consumption of the ethylene or propylene gas.[45,46] Application of ATR-FTIR to monitor the vibrational bands of polyethylene or polypropylene offers the possibility to study the catalyst performance in its working state and acquire *in-situ* information on the reaction kinetics.

ν(C-H) signals of growing polypropylene (PP) chain and diminishing ν(C-H) signals of benzene during the course of polymerization are shown in Figure 6.5a. The polymerization was carried out in benzene, which has a clear window in the region of 2800 – 2980 $cm^{-1}$. The integrated intensity of ν(C-H) signals in the range of 3000 – 2775 $cm^{-1}$ (asymmetric and symmetric $CH_2$ stretch) versus polymerization time is plotted in Figure 6.5b.
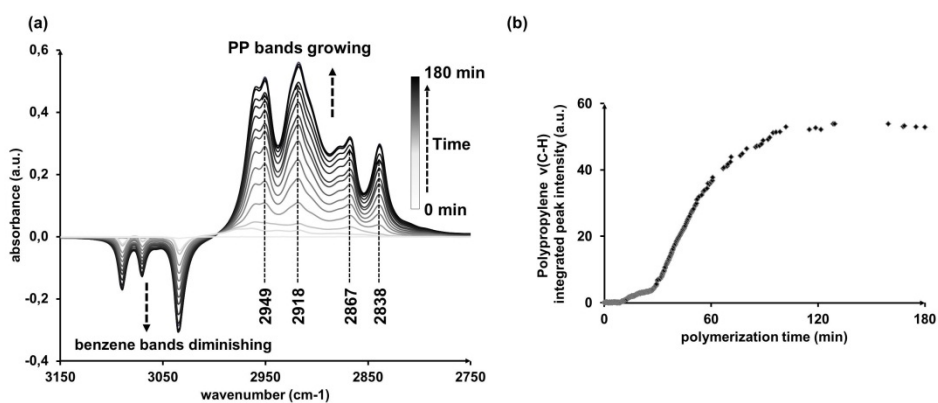
**Figure 6.5.** *(a) v(C-H) bands of growing polypropylene on MgCl₂/DIBP/TiCl₄ bound to flat ZnSe crystal; monitored by in-situ ATR-FTIR. The diminishing v(C-H) bands of benzene are also shown. (b) Plot of the integrated intensity of v(C-H) PP versus polymerization time.*

The intensity of $\nu$(C-H) signals of PP increases with polymerization time. After ~ 2 hours the $\nu$(C-H) signal was saturated. This is not necessarily indicating that the catalyst become inactive after 2 hours. Since the evanescent wave decays with distance from the crystal surface (as described in **Chapter 2**), the intensity does not depend linearly on the thickness of the film. For thin layers (< 200 nm) the measured integrated absorbance can be approximated to the scale linear with the concentration of the deposited material.[47] On the other hand, the polypropylene film is about more than 2 μm thick; leads to saturated band intensity. Therefore, to obtain kinetic information, a calibration curve of the dependence of the ATR-FTIR band intensity on the amount of PP formed is needed. The amount of PP formed on the crystal surface may be obtained by weight measurement or thickness determination. Our preliminary result of ATR-FTIR analysis during real-time polymerization demonstrates the future potential of the method to determine the polymerization kinetics.

ATR-FTIR spectroscopy offers the possibility of evaluating the isotacticity index (I.I) of PP. The ratio of $A_{997}/A_{974}$ has been used as a measure of tacticity.[48-53] Figure 6.6 shows transmission infrared spectra of 100% isotactic polypropylene and 100% atactic polypropylene in transmittance mode.[48]
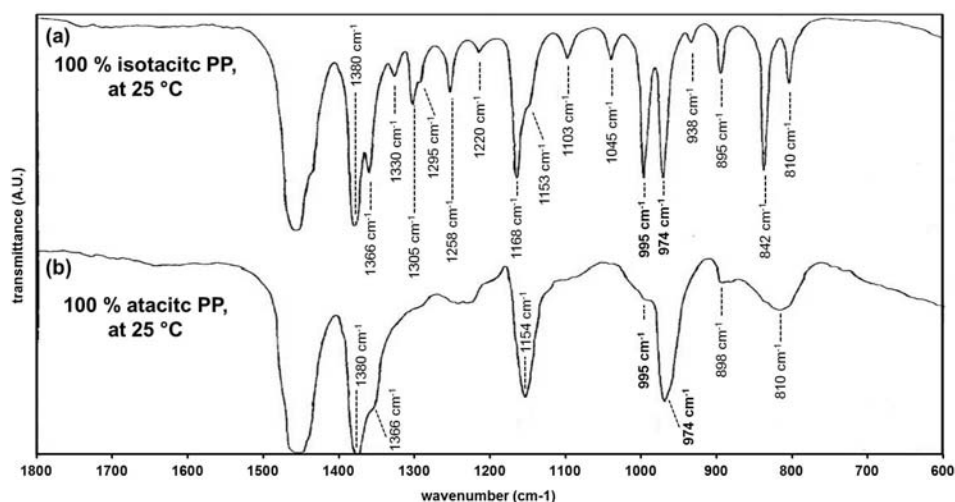
143

**Figure 6.6.** *Transmission infrared spectra of (a) 100 % isotactic (b) 100 % atactic polypropylene (both spectra measured at 25 °C).[48]*

The absorption band at 995 cm$^{-1}$ is due to isotactic helices.[48,49] The band at 974 cm$^{-1}$ is independent of isotacticity.[48,49] The bands of solid isotactic polypropylene at 974 and 1197 cm$^{-1}$ have been found to be due to the hybridized vibrations of the methyl rocking mode (asymmetric with respect to the H-C-methyl plane) and asymmetric stretching mode of the main chain CH-CH$_2$ bonds (axial and equatorial).[50] The bands at 1458 – 1376 cm$^{-1}$ might arise from CH$_2$ scissoring.[20]

The ATR-FTIR spectra of PP film grown on MgCl$_2$/DIBP/TiCl$_4$ catalyst is shown in the Figure 6.7a. The spectra reveals features similar to those of an IR spectrum of isotactic PP (Figure 6.6a). The band located at 997 cm$^{-1}$ in the ATR-FTIR spectra (noted as 995 cm$^{-1}$ in Figure 6.6) originating from isotactic helices of PP (hybridized vibration of methyl and methylene groups).[50]
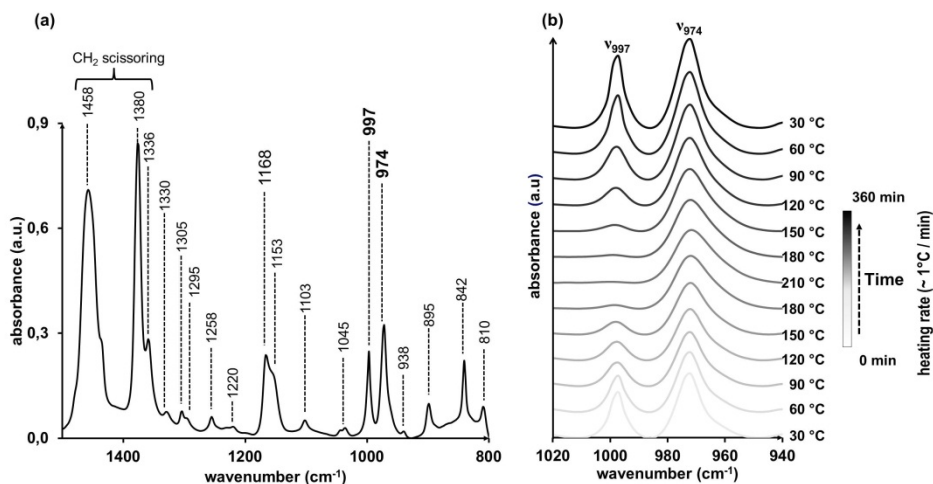
**Figure 6.7.** *(a) ATR-FTIR spectra of PP film produced over the MgCl$_2$/DIBP/TiCl$_4$ catalyst (measured at 25 °C, benzene free). (b) Changes in the ν$_{996}$ band during the melt-recrystallization of nascent polypropylene; monitored by in-situ ATR-FTIR.*

At this point, it would be appropriate to discuss the terms 'isotacticity' versus 'crystallinity'. When the nascent PP film shown in Figure 6.7 was heated, the band at 997 cm$^{-1}$ started to diminish; and at 210 °C the band was completely disappeared (Figure 6.7b). Upon cooling down, the band regains its intensity. It is reported that the volume fraction of long isotactic sequences is reflected in the intensity of this band at 997 cm$^{-1}$.[51] The intensity of this band is sensitive not only to the helical configuration but also to the long-range lateral packing.

*In-situ* propylene polymerization was also performed on donor free MgCl$_2$/TiCl$_4$ films. Figure 6.8a shows the infrared spectra of polypropylene obtained in the absence and presence of DIBP donor (measured at 25 °C, benzene free). The absorption band at 997 cm$^{-1}$ due to isotactic helices and absorption band at 974 cm$^{-1}$, along with the fitted curves are shown in the spectra. Images of PP films produced inside the ATR cell are shown in Figure 6.8b.
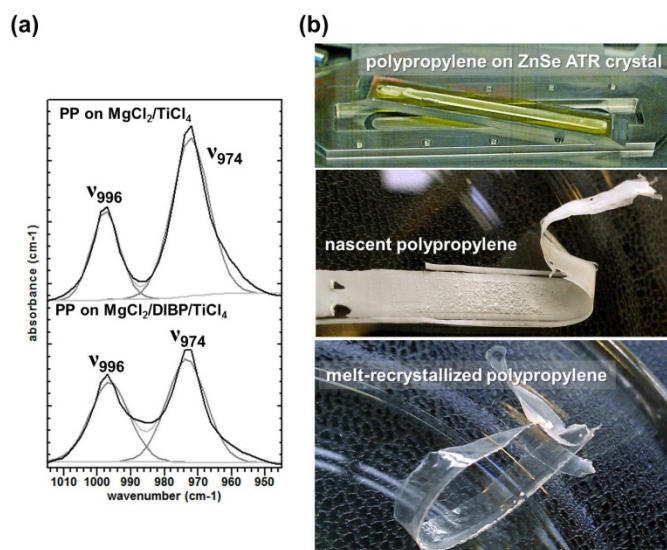
**Figure 6.8.** *(a) Infrared spectra of nascent polypropylene produced over catalyst including no donor (top) and catalyst including DIBP as internal donor (bottom). (b) Polypropylene film grown on ZnSe crystal from a flat model MgCl₂/DIBP/TiCl₄ catalyst (top); nascent polypropylene film peeled off from ATR crystal (middle); polypropylene film after melt recrystallization performed in ATR flow cell (bottom).*

The estimated ($A_{997}/A_{974}$ x 100) isotacticity for PP, from donor free catalyst was ~ 45 % and donor incorporated catalyst was ~ 70 % respectively. According to Andoni and coworkers, the estimated isotacticities of PP produced (via *ex-situ* propylene polymerization) over $MgCl_2/TiCl_4$, $MgCl_2/DIBP/TiCl_4$ and $MgCl_2/BMMF/TiCl_4$ flat-model catalysts were 60 %, 75 % and 80 % respectively.[43,54] Relatively low isotacticity of $MgCl_2/DIBP/TiCl_4$ systems compared to industrial catalyst (I.I ≥ 95 %) might be due to the absence of external donor to counter the removal of DIBP upon reaction with $AlEt_3$. In industry, DIBP based catalysts were always used in combination with external donors. Moreover, industrial process run at 70 °C and in the presence of hydrogen; which are the factors known to increase the isotacticity.[55] Whereas, our polymerization experiments were run at 30 °C, without hydrogen.

The successful trials of propylene polymerization show the potential of this method for correlating the surface chemistry of various Ziegler-Natta catalyst systems (prepared by altering the thermal pre-treatments or donor concentration as discussed in previous chapters) with the *in-situ* measured isotacticity of nascent polypropylene. Unfortunately, it was difficult to reproduce the polymerization activity after extensive donor studies. *In-situ* experiments were very sensitive to the moisture accumulation in the *in-situ* ATR-FTIR setup.

We analyze the key difference between a successful (Trial 1) and unsuccessful (Trial 2) propylene polymerization trials. The only difference we noticed was the moisture accumulation in the ATR flow cell during $TiCl_4$ impregnation. The $v(O-H)$, $v(C-H)$ and $v(C=O)$ regions of corresponding $MgCl_2$/DIBP films during $TiCl_4$ impregnation was shown in Figure 6.9. In the Trial 1 shown in Figure 6.9a, the ethanol was removed from the film under $TiCl_4$ impregnation without any significant moisture pickup. This catalyst showed activity towards propylene polymerization.
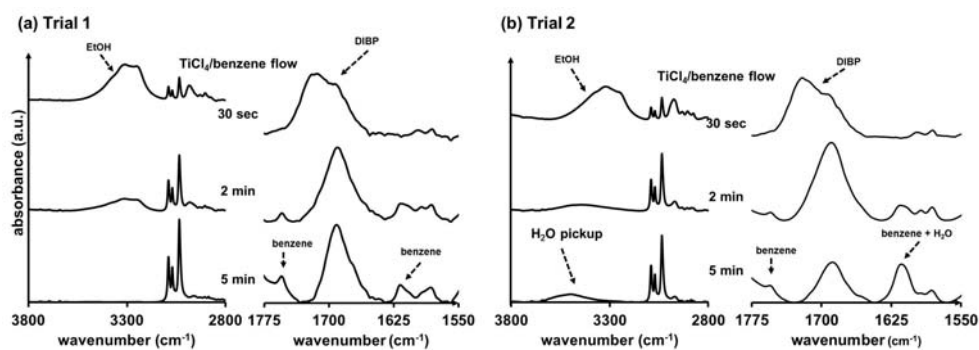


**Figure 6.9.** *$v(O-H)$, $v(C-H)$ and $v(C=O)$ regions of MgCl$_2$/DIBP films during TiCl$_4$ impregnation. Catalyst (a) shows activity towards propylene polymerization. Catalyst (b) was not active towards propylene polymerization.*

Another polymerization trial (Trial 2), performed at different time, shows significant moisture build up in the film during $TiCl_4$ impregnation (Figure 6.9b). Even though, the benzene bands interfere with the O-H scissoring band around 1630 cm$^{-1}$, the increased intensity of the particular band in Figure 6.9b clearly

indicates the incorporation of water to catalyst. Subsequent polymerization of the catalyst shown zero activity towards propylene polymerization.

Removal of ethanol from the $MgCl_2$/EtOH upon contact with $TiCl_4$ leaves back very hygroscopic anhydrous $MgCl_2$. The moisture from the gas/solvent flow adsorb/absorb to anhydrous $MgCl_2$. This could be the reason for the inactivity of catalysts.

To overcome the issues with moisture, we suggest a very drastic approach. Rebuilding the entire ATR setup in the glovebox can reduce the moisture accumulation on the connectors during transfer from glovebox to ATR setup. *Ex-situ* propylene polymerization (in glove box) trials on the same catalyst system was always successful and extensively reported by Andoni and coworkers.[54]

## 6.4 Summary

As a proof of principle, propylene polymerization was successfully carried out in *in-situ* ATR-FTIR setup. Application of ATR-FTIR to monitor the vibrational bands of the polyolefin offers the possibility to study the catalyst activity in its working state and acquire *in-situ* information on the reaction kinetics. At the same time, catalyst selectivity (or isotacticity of polymer) also can be estimated. However, the correlation of surface chemistry of various catalyst system versus the isotacticity of polypropylene was not achieved due to the reproducibility issues in propylene polymerization.

$TiCl_4$ and electron donors strongly interact with each other, but in the presence of $MgCl_2$, the DIBP strongly coordinate to the $MgCl_2$ support and remain relatively unperturbed by the presence of $TiCl_4$. At the same time, XPS studies shows that electron density around Ti species is increased when FDIBP is present in the film. $AlEt_3$ interacts with DIBP coordinated on $MgCl_2$, leads to the desorption of DIBP from the $MgCl_2$ film.

Once again, irrespective of the thermal (annealing) or chemical ($TiCl_4$ treatment or $AlEt_3$ treatment) method used to dealocohloate the $MgCl_2$/EtOH film; ethanol desorption leads to the reorganization of adsorption sites in the same manner.

148

# 6.5 References

(1) Moore, J. P. Jr. *Polypropylene Handbook: Polymerization;* Hanser Publishers: New-York, **1996,** Ch 2.

(2) Giannini, U. *Macromol. Chem. Suppl.* **1981,** *5,* 216.

(3) Busico, V.; Causa, M.; Cipullo. R.; Credendino, R.; Cutillo, F.; Friederichs, N.; Lamanna, R.; Segre, A.; Castelli, V. V. A. *J. Phys. Chem. C* **2008,** *112*, 1081.

(4) Correa, A.; Piemontesi, F.; Morini, G.; Cavallo. L. *Macromolecules* **2007,** *40,* 9181.

(5) Chadwick, J. C. *Macromol. Symp.* **2001,** *173,* 21.

(6) Sacchi, M. C.; Tritto, I.; Locatelli, P. *Prog. Polym. Sci.* **1991,** *16,* 331.

(7) Sacchi, M. C.; Florini, F.; Tritto, I.; Locatelli, P. Morini, G.; Noristi, L.; Albizzati, E. *Macromolecules* **1996,** *29* (10), 3341.

(8) Barbe, P. C.; Noristi, L.; Baruzzi, G.*Makromol. Chem.* **1992,** *193,* 229.

(9) Busico, V.; Corradini, P.; de Martino, L.; Proto, A.; Savino, V. *Makromol. Chem.* **1985,** *186,* 1279.

(10) Potapov, A. G.; Kriventsov, V. V.; Kochubey, D. I.; Bukatov, G. D.; Zakharov, V. A. *Macromol. Chem. Phys.* **1997,** *198,* 3477.

(11) Brambilla, L.; Zerbi, G.; Nascetti, S.; Piemontesi, F.; Morini, G. *Macromol. Symp.* **2004,** *213,* 287.

(12) Brambilla, L.; Zerbi, G.; Piemontesi, F.;Nascetti, S.; Morini, G. *J. Mol. Catal. A: Chem.* **2007,** *263,* 103.

(13) Monaco, G.; Toto, M.; Guerra, G.; Corradini, P.; Cavallo, L. *Macromolecules* **2000,** *33,* 8953.

(14) Martinsky, C.; Minot, C.; Ricart, J. M. *Surf. Sci* **2001,** *490,* 237.

(15) Boero, M.; Parrinello, M.; Weiss, H.; Hüffer, S. *J. Phys. Chem. A.* **2001,** *105,* 5096.

(16) D'Amore, M.; Credendino, R.; Budzelaar, P.; Causa, M.; Busico, V. *J. Catal.* **2012,** *286,* 103.

(17) Taniike, T.; Terano, M. *Macromol. Rapid. Commun.* **2008,** *29,* 1472.

(18) Hasebe, K.; Mori, H.; Terano, M. *J. Mol. Catal. A: Chem.* **1997,** *124,* L1**.**

(19) Hideharu, M.; Hasebe, K.; Terano, M. *Polymer* **1999,** *40,* 1389.

(20) Fregonese, D.; Glisenti, A.; Mortara, S.; Rizzi, G. A.; Tondello, E.; Bresadola, S. *J. Mol. Catal. A: Chem.* **2002,** *178,* 115.

(21) Pilling, M. J.; Fonseca, A. A.; Cousins, M. J.; Waugh, K. C.; Surman, M.; Gardner, P. *Surf. Sci.* **2005,** *587,* 78.

(22) Kaushik, V. K.; Gupta, V. K.; Naik, D. G. *Appl. Surf. Sci.* **2006,** *253,* 753.

(23) Yang, S.; Mingzhi, G.; Xi, Z.; Bingquan, M. *Chinese. Sci. Bull.* **2006,** *51,* 1393.

(24) Zhao, X.; Zhang, Y.; Song, Y.; Wei, G. *Surf. Rev. Lett.* **2007,** *14,* 951.

(25) Filho, A. A. S.; Alves, M. C. M.; Santos, J. H. Z. *J. Appl. Polym. Sci.* **2008,** *109,* 1675.

(26) Stukalov, D. V.; Zilberberg, I. L.; Zakharov, V. A. *Macromolecules* **2009,** *42,* 8165.

(27) Stukalov, D. V.; Zakharov, V. A. *J. Phys. Chem. C.* **2009,** *113,* 21376.

(28) Sergeev, S. A.; Poluboyarov, V. A.; Zakharov, V. A. *Makromol. Chem.* **1985,** *186,* 243.

(29) Brant, P.; Speca, A. *Macromolecules* **1987,** *20,* 2740.

(30) Chien, J. C. W.; Hu, Y. *J. Polym. Sci. A: Polym. Chem.* **1989,** *27,* 897.

(31)    Tregubov, A. A.; Zakharov, V. A.; Mikenas, T. B. *J. Polym. Sci. A: Polym. Chem.* **2009,** *47,* 6392.

(32)    Rytter, E.; Nirisen, Ø.; Ystenes, M.; Øye, H. A. *Mikrochim. Acta.* **1988,** *II,* 85.

(33)    Ystenes, M.; Rytter, E. *Spectrochim. Acta.* **1992,** *48A,* 543.

(34)    Song, W. D.; Chu, K. J.; Chang, H. S.; Ihm, S. *J. Mol. Catal.* **1993,** *84,* 109.

(35)    Yang, C. B.; Hsu, C. C.; Park, Y. S.; Shurvell, H. F. *Eur. Polym. J.* **1994,** *30,* 205.

(36)    Ferreira, M. L.; Damiani, D. E. *J. Polym. Sci. A: Polym. Chem.* **1994,** *32,* 1137.

(37)    Potapov, A. G.; Bukatov, G. D.; Zakharov, V. A. *J. Mol. Catal. A: Chem.* **2006,** *246,* 248.

(38)    Potapov, A. G.; Bukatov, G. D.; Zakharov, V. A. *J. Mol. Catal. A: Chem.* **2009,** *301,* 18.

(39)    Chastrain, J. *Handbook of X-ray photoelectron spectroscopy;* Perkin-Elmer Corporation: **1992.**

(40)    Marques, M.; Almeida, L.; Cruz, K. *Chem. Chem. Technol.* **2010,** *4,* 291.

(41)    Terano, M.; Katakoa, T.; Hosaka, M.; Keii, T. *Transition metals and organometallics as catalysts for olefin polymerization;* Kamisnky, W.; Sinn, H., Eds.; Springer: Berlin, **1988.**

(42)    Jeong, Y, T.; Lee, D. H. *Macromol. Chem.* **1990,** *191,* 1487.

(43)    Andoni, A.; Chadwick, J. C.; Niemantsverdriet, J. W. (Hans).; Thüne, P. C. *Catal. Lett.* **2009,** *130,* 278.

(44)    Magni, E.; Somorjai, G. A. *J. Phys. Chem.* **1998,** *102,* 8788.

(45)    Kaul, F. A. R.; Puchta, G. T.; Schneider, H.; Bielert, F.; Mihalios, D.; Herrmann, W. A. *Organometallics* **2002,** *21,* 74.

(46)    Semikolenova, N. V.; Zakharov, V. A.; Talsi, E. P.; Babushkin, D. E.; Sobolev, A. P.; Echevskaya, L. G.; Khysniyarov, M. M. *J. Mol. Catal. A: Chem.* **2002,** *182,* 283.

(47)    Müller, M.; Keßler, B. *Langmuir* **2011,** *27* (20), 12499.

(48)    Luongo, J. P. *J. Appl. Poly. Sci.* **1960,** *9*(3), 302.

(49)    Boor, J. Jr. *Ziegler-Natta Catalysts and Polymerization;* Academic Press: New-York, **1979,** Ch 3.

(50)    Miyazawa, T. *Polym. Lett.* **1964,** *2,* 847.

(51)    Koenig, J. L.; van Roggen, A. *J. Appl. Polym. Sci.* **1965,** *9,* 359.

(52)    Burfield, D. R.; Loi, P. S. T. *J. Appl. Polym. Sci.* **1988,** *36,* 279.

(53)    Koranyi, T. I.; Magni, E.; Somorjai, G. A. *Top. Catal.* **1999,** *7,* 179.

(54)    Andoni, A., *A Flat Model Approach to Ziegler-Natta Olefin Polymerization Catalysts;* Ph. D Thesis., Eindhoven University of Technology: The Netherlands, **2009.**

(55)    Chadwick, J. C.; Morini, G.; Balbontin, G.; Sudmeijer, O. *Macromol. Chem. Phys.* **1998,** *199,* 1873.

# 7

# Conclusions and outlook

# Abstract

*The objective of this chapter is to provide an overview or evaluation of the results achieved throughout this research work and its relevance in the broad picture of Ziegler-Natta catalysis research. This chapter also discusses the possibilities of extending the research in the future and the challenges to overcome.*

## 7.1 Conclusions

During the course of this research, we have developed a realistic (and active) model for a Ziegler-Natta catalytic system that allows detailed study by *in-situ* ATR-FTIR, XPS (surface chemistry) and TEM (morphology). Our approach in the preparation of Ziegler-Natta planar model catalyst involved spin coating of $MgCl_2$ from the ethanol solution (optionally containing internal donor) onto an ATR crystal/Si wafer/TEM grid, followed by contacting with $TiCl_4$ in hydrocarbon at room temperature. In this way, we attempt to mimic an industrial catalyst preparation; in which supports formed by cooling emulsions of molten $MgCl_2.nEtOH$ adducts in paraffin oil, subsequently react with $TiCl_4$.[1] The model catalyst was used to gain a fundamental understanding, in particular with regard to the molecular level picture of internal donor (DIBP) – $MgCl_2$ support interactions.

A sensitive method was developed for the quantitative investigation of DIBP on $MgCl_2$ support by means of ATR-FTIR (**Chapter 3**). The method is based on the linear relationship between the integrated peak intensity of a carbonyl stretching band of DIBP and the concentration of DIBP (in the solutions used for spin coating) in $MgCl_2$ films. The results were confirmed by XPS studies on an F-labelled homologue of DIBP (4-fluorodiisobutyl phthalate or FDIBP), which showed a sufficient similarity in coordination behaviour compared to DIBP. Since ethanol is involved in the preparation method of $MgCl_2$ crystallites, it was essential to examine the effect of ethanol on the DIBP coordination behaviour. We found that ethanol – *not DIBP* – act as the surfactant at the stage of $MgCl_2$ crystal formation. A set of $\nu(C=O)$ DIBP components representing various surface species of DIBP was derived from 'chemical intuition'. In order to explain the surface chemistry of $MgCl_2$/DIBP films, these components were used to resolve the $\nu(C=O)$ envelope of DIBP. Ethanol, as a strong adsorbate saturates the surface sites on $MgCl_2$ crystal, leaving DIBP as uncoordinated molecule. Upon heating, evaporation of ethanol occurs; first from the weakly acidic sites (104), later from the strongly acidic sites (110). DIBP colonizes the available surfaces on $MgCl_2$ in the same order as the ethanol removal; first on (104) sites later on (110) sites. The red shift in the $\nu(C=O)$ was explained as the transfer of DIBP from uncoordinated state to coordinated on (104) state and then to coordinated on (110) site. Using this

approach based on experimental spectra and 'chemical intuition', we were not able to predict/understand the coordination modes of adsorbed DIBP using this model.

TEM results (morphology) on $MgCl_2$ and $MgCl_2$/DIBP films indicates that, removal of adsorbate from the film leads to the sintering of $MgCl_2$ crystallites. Since, ethanol plays a key role in the $MgCl_2$ crystallite surface structure and coordination behaviour of DIBP; *in-situ* coordination of DIBP on $MgCl_2$/EtOH films with different concentration of ethanol was performed. It is generally believed that, the presence of diether donors promotes the formation of $MgCl_2$ (110) as the lateral surface termination. $MgCl_2$ crystals consist of only (110) lateral terminations were prepared by co-impregnation of surface selective donors such as 9, 9'-bis (methoxymethyl) fluorene.[2] Subseqently, *in-situ* coordination of DIBP on (110) surface was carried out. With this strategy, we isolated sets of $MgCl_2$/DIBP films with sharp $\nu$(C=O) bands, indicative of DIBP coordination exclusively (or predominantly) on one surface site of $MgCl_2$ (**Chapter 4**). Similar studies were performed on ethyl benzoate (EB); which is a monodentate donor. The significant differences between the coordination behaviour of monodentate donor EB and bidentate donor DIBP indicates that DIBP prefers to coordinate $MgCl_2$ in a bindentate mode.

In order to elucidate the binding modes of DIBP on $MgCl_2$ surfaces, our collaborators conducted a DFT-D study to model the possible modes of dimethyl phthalate (DMP, methyl homologue of DIBP) coordination on various $MgCl_2$surfaces (**Chapter 4**). The corresponding IR spectra were also simulated by DFT-D.

Using these simulated IR bands as input, a set of components were derived to resolve the experimental IR bands; and a more accurate approach (DFT-experiment reconciled approach) was developed to explain the surface chemistry of $MgCl_2$/DIBP films (**Chapter 5**). Figure 7.1 represents experimentally isolated $\nu$(C=O) envelope of various DIBP species on $MgCl_2$ and the most appropriate assignment by DFT (based on matching wavenumbers).
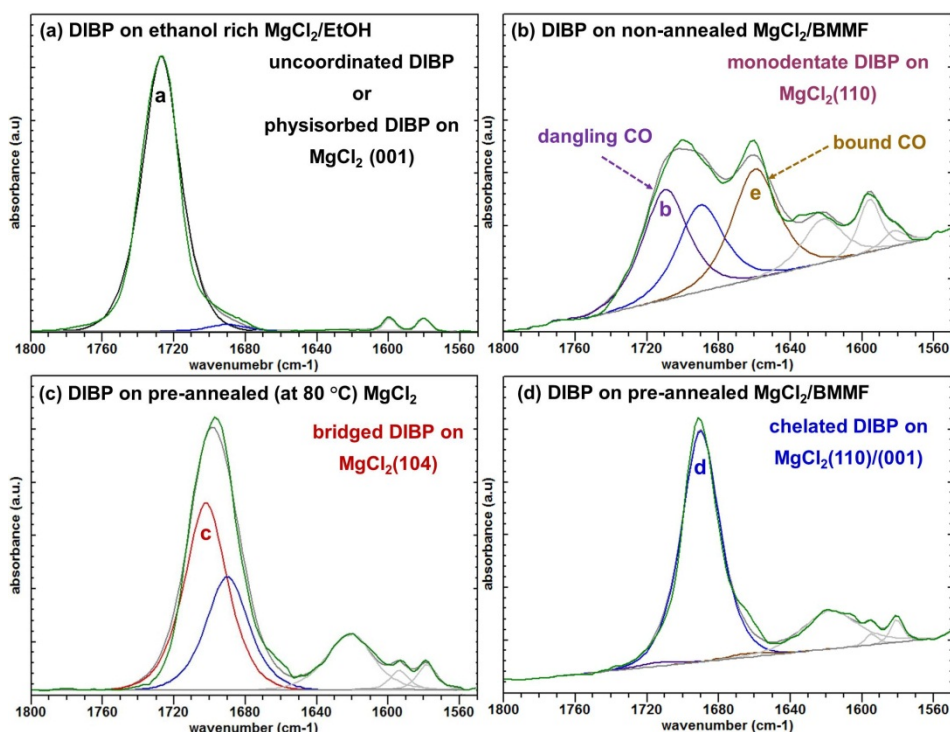
**Figure 7.1.** *v(C=O) DIBP of various DIBP surface species (isolated by adsorbing DIBP over MgCl₂ support with known surface structure).*

When two sets of components (derived from 'chemical intuition' approach and DFT-experiment reconciled approach) used to explain the surface chemistry of DIBP on MgCl$_2$ surface were compared, the conclusions achieved by both approaches are in qualitative agreement. The migration of uncoordinated DIBP to (104) surface and then to (110) surface was predicted by both approaches. Also, the reconstruction of MgCl$_2$ (110) surface into MgCl$_2$ (104) in the absence of adsorbate, can be explained by both approaches.

Changes in the surface chemistry of the MgCl$_2$ film with respect to temperature can be summarized (**Chapter 5**) in Figure 7.2.



**Figure 7.2.** *Surface chemistry of in-situ coordinated DIBP in MgCl$_2$/EtOH films at different temperatures [based on resolving v(C=O) bands using components derived by DFT-experiment reconciled approach]. The TEM image of well-defined and sintered MgCl$_2$ film is also shown in the figure. The hexagonal structure indicates only one type of lateral surface termination is present.[2] Rectangular/square structures indicate both lateral surface terminations are present in the system.[2] The difference in the length of surfaces is a symbolic representation of relative abundance of both surfaces.*

Changes in the surface chemistry of MgCl$_2$/DIBP film with respect to temperature can be summarized (**Chapter 5**) in Figure 7.3.
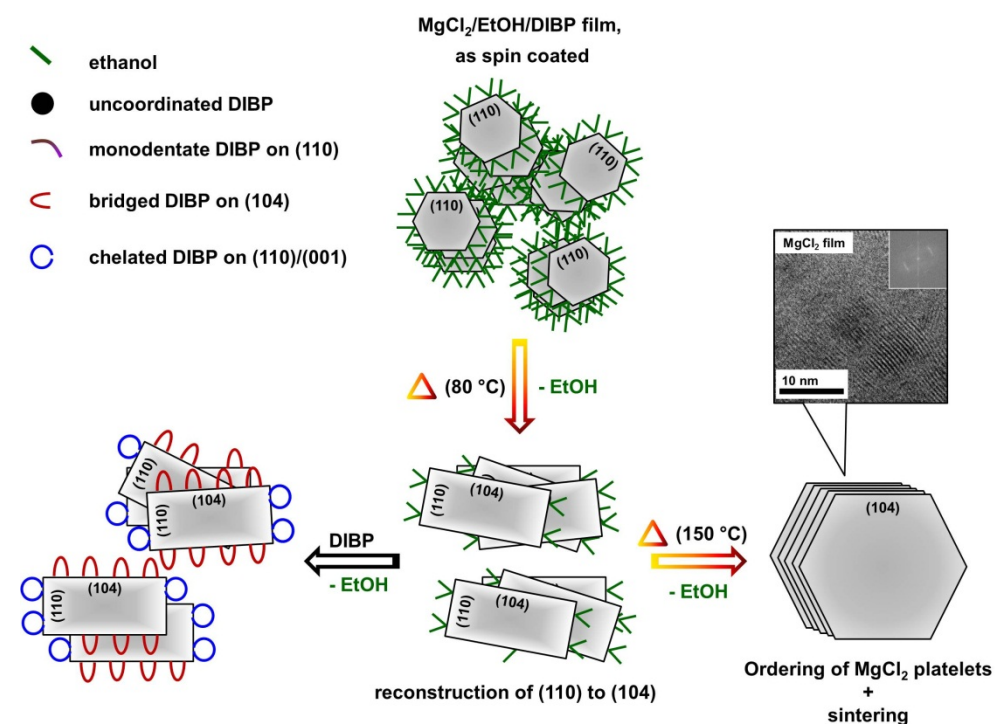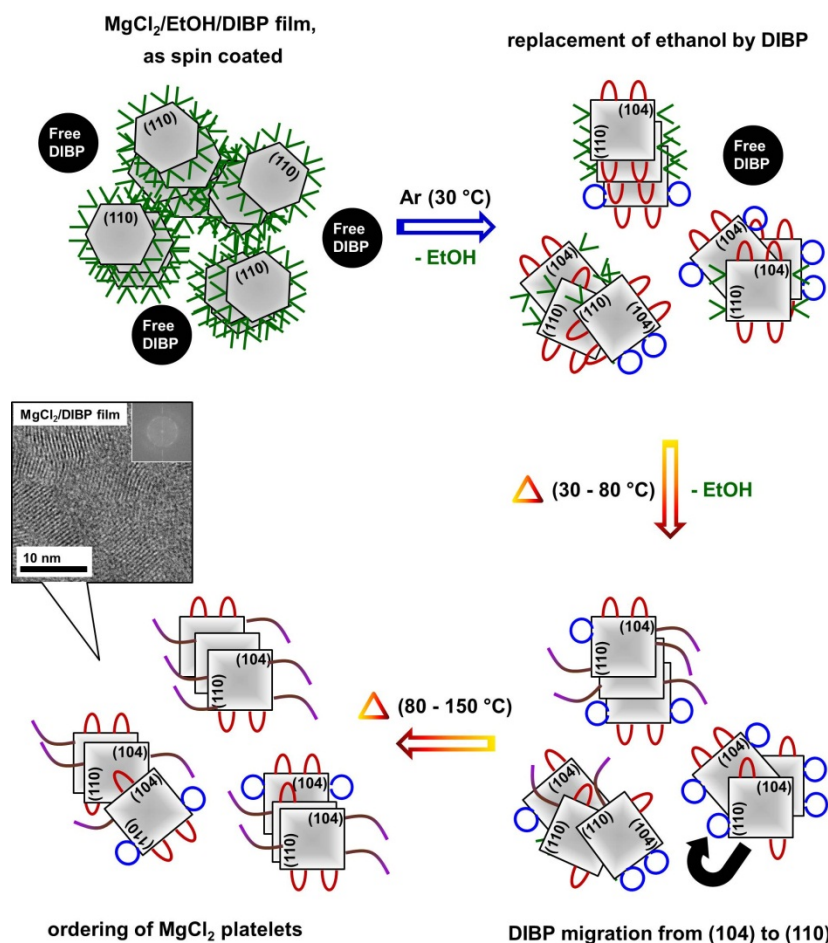


**Figure 7.3.** *Surface chemistry of DIBP in the co-impregnated MgCl$_2$/EtOH/DIBP films at different temperatures [based on resolving v(C=O) bands using components derived by DFT-experiment reconciled approach]. TEM image of well-defined but randomly oriented small crystallites of MgCl$_2$ in the MgCl$_2$/DIBP film is also shown in the figure. The hexagonal structure indicates only one type of lateral surface termination is present.[2] Rectangular/square structures indicate both lateral surface terminations are present in the system.[2]*

As a proof of principle, *in-situ* propylene polymerization was carried out on the *in-situ* titanated $MgCl_2$/DIBP film (**Chapter 6**). However, *in-situ* experiments were very sensitive towards minute amounts of moisture accumulate during $TiCl_4$ impregnation step, makes it extremely difficult to obtain reproducible results. Therefore, the ultimate aim to correlate the surface chemistry of catalysts with stereoselectivity was not achieved.

The targets of this project were to (i) acquire a molecular level information on the $MgCl_2$ surfaces (believed to be the active sites in Ziegler-Natta catalysts), by probing internal donor bound to the $MgCl_2$ surface; (ii) correlate the surface chemistry (from the information attained by previous objective) to the catalyst performance (activity and selectivity towards propylene polymerization). The first objective was successfully achieved, but the latter one was not.

## 7.2 Future perspectives

Research projects are never really completed, which is also true in the case for the work described in this thesis. Our approach to flat-model catalyst still have lots of scope for future research.

- Solve the reproducibility issues with *in-situ* propylene polymerization, which will help to correlate surface chemistry with catalyst performance.

- Explore the surface chemistry of $MgCl_2$/succinate donors. As like phthalate esters, succinate donors are also very easy to detect with infrared. Preliminary studies with 2,3-diisopropyl diethyl succinate (DIPS) showed that the coordination behaviour of DIPS is similar to that of DIBP.

- Even though the silane donors are difficult to detect (in the sense of quantitative studies) with infrared (especially, in the presence of intense signals from ethanol), internal donor - external donor exchange studies can be done within *in-situ* ATR-FTIR set up. Probing the changes in co-impregnated internal donor with respect to the interaction with external donor – in the presence/absence of $AlEt_3$ – will help to understand the structure of internal donor complexes which easily removed from the $MgCl_2$ surface, in turn leads to the decrease in stereoselectivity.

- Extend the *in-situ* ATR-FTIR study to model supports and catalysts prepared and analyzed *ex-situ* (supports with known morphology, characterized by other techniques). Expansion of our model catalyst approach to this direction creates the opportunity to bridge the gap between model and industrial catalysts even further. The main challenge will be the method to fix the catalyst material on ATR crystal.

- Efforts to identify the crystallographic orientation of active surfaces by employing TEM were not successful until now. The small crystallites of $MgCl_2$ formed upon spin coating, prefers to have edge-on-orientation ($MgCl_2$ platelets arranged parallel to the surface normal) on a $SiO_2/SiN_X$ TEM grid. Relatively large crystallites of $MgCl_2$ prepared via Ostawld-ripening method might have flat-on-orientation over TEM grid, and the edges of the crystal can be pictured by TEM. Residual ethanol in the film can cause serious damage to the crystal when exposed to the strong electron beam. The crystals stabilized by small amounts of polymer (catalyst after polymerization for a very short time) might help to visualize the surface sites.

## 7.3 References

(1)  Albizzati, E.; Cecchin, G.; Chadwick, J. C.; Collina, G.; Giannini, U.; Morini, G.; Noristi, L. *Polypropylene Handbook, 2nd Edition;* Pasquini, N., Ed.; Hanser: Munich **2005,***Ch 2*.

(2)  Andoni, A.; Chadwick, J. C.; Niemantsverdriet, J. W. (Hans).; Thüne, P. C. *J. Catal.* **2008,***257,* 81.

# A

# Thesis summary / abstract

## <u>Surface Chemistry of Flat-Model Ziegler-Natta Catalysts</u>

**D**ue to the excellent properties as a thermoplastic polymer, polypropylene has become one of the fastest growing general resin since its commercialization in 1957. Ziegler-Natta catalysis is one of the most important industrial processes in the mass production of polypropylene with a high degree of stereoselectivity. Most of the Ziegler-Natta catalysts for stereospecific olefin polymerization contain $MgCl_2$ as support, $TiCl_4$ as the catalyst, a trialkyl aluminium as cocatalyst, and two Lewis bases acting as internal and external donors. This catalyst is generally described as particles of activated $MgCl_2$, composed of irregularly stacked Cl-Mg-Cl sandwich-like monolayers, with the microstructures terminated by the (110) and (104) lateral cuts. The reaction of $MgCl_2$ support with $TiCl_4$ leads to the adsorption of $TiCl_4$ on these lateral cuts of $MgCl_2$.

While Ziegler-Natta catalyst has been evolved to become highly active and selective olefin polymerization catalyst that still monopolize the worldwide production of polypropylene, the nature of active sites responsible for stereospecific polypropylene remains elusive. An important reason for this uncertainty regarding the molecular level details of the industrial catalyst is lack of reliable spectroscopic information about the reactive surface; especially the experimental details of the electron donor interactions with the support, catalyst and cocatalyst.

In an attempt to gain deeper insight into the surface chemistry of active Ziegler-Natta catalysts, we have developed a model system based on a thin film of nanocrystalline $MgCl_2$ prepared from $MgCl_2$/ethanol solution by means of spin-coating impregnation. This model system is allows to follow morphology and elemental composition by ex-situ surface characterization techniques such as X-ray Photoelectron Spectroscopy (XPS) and Transmission Electron Microscopy (TEM). Key steps in the evolution of active surface were followed by *in-situ* Attenuated Total internal Reflection – Fourier Transform Infrared Spectroscopy (ATR-FTIR).

We prepared a thin film analogue for Ziegler–Natta propylene polymerization catalyst support by spin-coating a solution of $MgCl_2$ in ethanol, optionally containing a diester internal donor (diisobutyl phthalate – DIBP) on a flat ATR crystal surface. The donor content of these films was quantified by ATR-FTIR. The results were calibrated against XPS data of F-labeled DIBP homologue (4-fluoro diisobutyl phthalate – FDIBP). $MgCl_2$ support with one type of lateral surface termination was prepared by the formation of $MgCl_2$ crystallites in the presence of surface sensitive electron donors such as diethers. Subsequent exchange of diether donor with DIBP result in the coordination DIBP exclusively on $MgCl_2$ (110). Relatively sharp IR bands of these DIBP surface species were useful for explaining the broad DIBP IR bands in Ziegler-Natta catalyst.

In order to elucidate the binding modes of DIBP on $MgCl_2$ surfaces, our collaborators conducted a DFT-D study to model the possible modes of dimethyl phthalate (DMP, methyl homologue of DIBP) coordination on various $MgCl_2$ surfaces. The corresponding IR spectra were also simulated by DFT-D. Using these simulated IR bands as input, a set of components were derived to resolve the experimental IR bands; and a more accurate approach (DFT-experiment reconciled approach) was developed to explain the surface chemistry of $MgCl_2$/DIBP films.

We explain the $\nu$(C=O) adsorption band of DIBP as a combination of four overlapping components assigned to uncoordinated DIBP, bridged to $MgCl_2$ (104), chelated to $MgCl_2$ (110)/(001) and bound to (110) in a monodentate mode. Based on the peak fitting, the changes in the $\nu$(C=O) adsorption band can be explained as the redistribution of DIBP on different $MgCl_2$ surface sites, induced by the removal of coadsorbed ethanol and $MgCl_2$ surface reconstruction. As a proof of principle, we managed to polymerize propylene over the catalysts we made. TEM studies showed that nanocrystallites of $MgCl_2$ in DIBP-free $MgCl_2$ films sinter upon annealing. On the other hand, presence of DIBP inhibits the sintering of $MgCl_2$ nanocrystallites up to an extent.

As a summary, $MgCl_2$ (110) sites are relatively unstable in the absence of adsorbates; leads to the reconstruction of to $MgCl_2$ (110) in to $MgCl_2$ (104). Presence of an internal donor as an adsorbate will stabilize $MgCl_2$ (110) from restructuring and prevents overall $MgCl_2$ nanocrystals from sintering. The knowledge about the relative stability of active sites and electronic structure of internal donor $MgCl_2$ complexes will help to design tailor made electron donors which can improve the performance of Ziegler-Natta catalysts.

# B

# Acknowledgments

**T**here are some stories behind a graph. There are even many more stories behind a thesis. In each story, there are people who play their own roles, which are in synergy with each other to make this thesis complete.

First, my utmost thanks go to Peter, my supervisor and co-promotor. Dear Peter, there has been hardly anyone as close as you to see this research evolve over time. Thank you for your guidance, help, enthusiastic discussions and an immeasurable amount of time provided during my doctoral education and dissertation process.

I am grateful to Hans, my promotor, for giving me an opportunity to carry out my Ph.D. in his excellent research group. Working on a Ph.D. Project is more than doing experiments and collecting data. It is about developing valuable attributes to be a good scientist. Thank you Hans, for supervising me to develop these skills. I appreciate your encouragement, advice and patience during the whole timeframe of Ph.D.

It is with immense gratitude that I acknowledge the other members of my defense committee – prof. Vincenzo Busico, prof. Peter Budzelaar, prof. René Janssen, dr. Gurram Kishan and prof. Jaap Schouten for kindly accepting our invitation and taking their precious time to evaluate my thesis in such a short period of time.

I am indebted to the Dutch Polymer Institute (DPI) for its financial support (project #712). Once again, I would like to express my gratitude to prof. Vincenzo Busico for his support, encouragement and scientific input throughout this thesis. Dear Magda, I would like to express my appreciation for allowing me to apply your DFT studies in my thesis. Reconciling your DFT studies with our results brought this thesis into a different height. I am thankful to prof. Minoru Terano and dr. Toshiaki Taniike, our collaborators in Japan, for their valuable support. I am thankful to all the industrial contact persons in DPI polyolefin community for their contribution to the success of our project #712.

Dear Tiny, many thanks to you for letting the lab run smoothly with your great effort to maintain, develop and repair equipment. This thesis will not be possible without the professional technical support from you. I wish to be an expert like you one day. I really

163

enjoyed the last two 'F1 manager' leagues and the post-race discussions. Hopefully, I can join the next season from a different location.

Dear Ernie, your background works on our ATR equipment helped me to 'drive' the project without any 'turbo lag'. I am thankful to your participation in the project.

Thanks to Therese-Anne, Marianne, José Jong and Susan Opgenoorth for their administrative help.

I consider it an honor to work with the members in the 'physical chemistry of surfaces' (PCS) group, namely Freek, Maarten, Henno, Vijay, Akthar, Jose Gracia, Manolo, Jasper, Gilbère, Kees-Jan, Başar, Remco, Ali, Hans F, Emad, Deshen, Huapeng, Zhenghang, Oluş, Yibin and Chenghua. I appreciate the productive and enthusiastic discussions we had during our group meetings and also during one to one discussions. Thanks for the wonderful time in the group and all the best for your venture (project/job). I would like to extend my gratitude to various members from the 'old' SKA and guest researchers for the discussions, support and fun through these four years. I always found my office room-mates cheerful and friendly. Dear Freek, Gilbère, Hans F, Zhenghang and Remco, special thanks for that. Dear Gilbère, thanks for the Kratos XPS measurements. Dear Jasper, many thanks for the fantastic CSV-DAT converter program you worte for me. Dear Emad and Deshen, I am going to miss our lunch break discussions about the trip to Antarctica, ManU, wild dreams, …

Dear Basale, many thanks for your constant support and motivation during the thesis writing time; especially to catch up with the deadline, which is always same for us. All the best wishes for your defense.

The time I spent in the Netherlands will remain memorable due to the enjoyable company of Indian friends. The list might be too long, and with a fear of forgetting someone, I would just say, thanks to all of you. Be it the cricket matches, cycling, dinner parties or other gatherings, I enjoyed each of them. Dear Shaneesh, words cannot do justice to what I owe you. Dear Eldhose, I really enjoyed our evening walk and debates. Best of luck with your defense. Many thanks to Rashija, Bobby, Deepak, Babu, Indu, Nishant, Sreema, Aromal, Thiru, Ratheesh, Vinod, Mukul, Hrishi, Mrinal and Dominic for making my life in Eindhoven enjoyable.

I would like to acknowledge Ajay for organizing road trips at the right time during the last four years. Those breaks were really helpful to refresh the mind and focus on work again. Sincere thanks to Sajin, Anish, Meera and Anjana for their support during past years, and I wish you all lot of success in your life.

It gives me tremendous pleasure to express my sincere gratitude to dr. Gurram Kishan. He was the one who aroused my interest in catalysis and encouraged me to pursue my Ph.D outside India. I am thankful to colleagues at GE Plastics / SABIC innovative plastics, especially dr. Ganesan, dr. Ram, dr. Pushpa, Vaidya and Anup Krishnan, for their constant support and motivation.

This thesis would not be possible without the support and prayers from my family members. I am deeply indebted to my papa Verghese and mamma Mary for their love, prayers, support and allowing me to go abroad for the studies. Deep appreciations to my sister Moly and brother-in-law Sabu for their encouragement throughout my stay abroad. I would like to express my gratitude to all cousins, nieces and nephews who keep me happy with their care and smiles.

Above all, I thank ALMIGHTY for enabling me to reach so far in my studies and complete this project successfully.

I will close this section with the statement *"though, many have not been mentioned here; none is forgotten"*.

Eindhoven

October 2013

# C

# List of publications / thesis output

Journal publications

- Ajin V. Cheruvathur, Ernie H. G. Langner, Hans (J. W.) Niemantsverdriet, Peter C. Thüne, *In-situ ATR-IR studies on MgCl$_2$-diisobutyl phthalate interactions in thin film Ziegler-Natta catalysts*, Langmuir, 28 (2012) 2643-2651.

- Ajin V. Cheruvathur, Maddalena D'Amore, Hans (J. W.) Niemantsverdriet, Peter C. Thüne, Vincenzo Busico, *Insight into the genesis and surface structure of MgCl$_2$-supported Ziegler-Natta catalysts: a combined flat-model and periodic DFT-D study of MgCl$_2$/EtOH/diisobutyl phthalate precursor phases*, Manuscript in preparation.

Oral presentations at conferences

- Ajin V. Cheruvathur, Ernie H. G. Langner, Hans (J. W.) Niemantsverdriet, Peter C. Thüne, *In-situ ATR-IR studies on MgCl$_2$-internal donor interactions*, XIIIth Netherlands Catalysis & Chemistry Conference, Noordwijkerhout, The Netherlands, March 5-7, 2012.

- Ajin V. Cheruvathur, Ernie H. G. Langner, Hans (J. W.) Niemantsverdriet, Peter C. Thüne, *Surface chemistry of MgCl$_2$/EtOH thin films*, International workshop on 'Molecular architecture of heterogeneous olefin polymerization catalysts', Ishikawa, Japan, December 14-15, 2009.

Poster presentations at conferences

- Ajin V. Cheruvathur, Ernie H. G. Langner, Hans (J. W.) Niemantsverdriet, Peter C. Thüne, *Surface chemistry of MgCl$_2$ & Ziegler-Natta catalysts*, 8th International

colloquium on 'Heterogeneous Ziegler-Natta catalysts', Kanazawa, Japan, March 27-30, 2012.

(*won 'young scientist award'*)

- Ajin V. Cheruvathur, Ernie H. G. Langner, Hans (J. W.) Niemantsverdriet, Peter C. Thüne, *In-situ ATR-IR studies on flat-model Ziegler-Natta catalysts*, European graduate summer school, Rolduc abbey, The Netherlands, June 20-23, 2011.
(*won first prize in the poster competition*)

- Ajin V. Cheruvathur, Ernie H. G. Langner, Hans (J. W.) Niemantsverdriet, Peter C. Thüne, *Surface chemistry and morphology of MgCl$_2$ thin films*, 3$^{rd}$ Blue sky conference on 'catalytic olefin polymerization', Sorrento, Italy, June 20-23, 2010.

# D

# Curriculam vitae

**A**jin Cheruvathur was born on 31st of May, 1985, in Vadakkekad (Kerala), India. After finishing higher secondary school education in June 2002, he commenced his degree studies at St.Thomas' College, Thrissur (University of Calicut). He completed his Bachelor of Science Degree (Chemistry as main subject) in June 2005. In the same year, he started his post-graduation studies at the same institution. His master project was performed at Polymer Science & Rubber Technology lab in Cochin University of Science & Technology (CUSAT). Main focus of the project was to synthesize various conducting polymers, followed by detailed studies on its structure – property relationships. In December 2007, he finished his master degree in Chemistry.

In February 2008, he joined as a research consultant in SABIC Innovative Plastics division (Formerly GE Plastics) at John. F. Welch Technology Centre, Bangalore. There he worked in various projects related to synthesis and characterization of different monomers and polymers. After completing one year internship in March 2009, he joined as a Junior Research Fellow at Indian Institute of Space-science & Technology (IIST) at Thiruvananthapuram, in a project titled "Polymer nano-composites for electronic and photonic applications".

In September 2009, he started his Ph. D studies on the Dutch Polymer Institute project, titled "Elucidation and control of the active surface structure and chemistry in $MgCl_2$-supported Ziegler-Natta catalysis: an integrated and computational approach"; under supervision of prof. dr. J. W. Niemantsverdriet at the Surface Science Laboratory of Inorganic Chemistry & Catalysis research group, TU/e. This project aims to improve the knowledge about the surface chemistry of Ziegler-Natta catalyst; by investigations on flat-model catalyst surface, using various surface characterization techniques. The most important results of that work are described in this thesis.